

Study of correlation between flow harmonics in
Heavy Ion collisions at $\sqrt{s_{NN}} = 2.76$ TeV with
ALICE at LHC

Myunggeun Song

The Graduate School
Yonsei University
Physics Department

Study of correlation between flow harmonics in
Heavy Ion collisions at $\sqrt{s_{NN}} = 2.76$ TeV with
ALICE at LHC

A Ph.D Thesis
Submitted to the Physics Department
and the Graduate School of Yonsei University
in partial fulfillment of the
requirements for the degree of

Myunggeun Song

November 30, 2016

Contents

List of Figures	iv
List of Tables	xi
Abstract	xi
Chapter 1. Introduction	1
1.1 Quantum Chromo Dynamics (QCD)	1
1.2 Quark Gluon Plasma (QGP).....	2
1.3 Heavy ion collision.....	3
1.4 Flow	7
1.4.1 Event Plane method.....	14
1.4.2 Scalar product method	16
1.4.3 Cumulants method.....	19
1.5 Jet quenching	23
1.6 Correlation between flow harmonics	27
Chapter 2. Experimental setup	31
2.1 Large Hadron Collider	31
2.2 The ALICE experiment	33
2.2.1 ITS	34
2.2.2 TPC.....	35
2.2.3 VZERO	36
2.2.4 Other detectors	39
2.2.5 Analysis Framework	40

Chapter 3. Data analysis	42
3.1 Data selection.....	42
3.1.1 Default cuts and settings	42
3.1.2 Data QA.....	44
3.2 Analysis strategy.....	46
3.3 Systematics.....	52
3.3.1 Systematics from Non uniform phi distribution	52
3.3.2 Systematics from Event selection	54
3.3.3 Systematics from Track selection.....	56
3.3.4 Overall systematic uncertainty	58
Chapter 4. Results	61
4.1 $SC(m, n)$ Results.....	61
4.1.1 $SC(3, 2)$ and $SC(4, 2)$	61
4.1.2 Model Comparison	64
4.2 Higher order flow harmonics results.....	72
4.3 p_T dependence of $SC(m, n)$ and $NSC(m, n)$	76
4.4 Method comparison	81
Chapter 5. Conclusion and Outlook	88
Appendices	91
Chapter A. Toy MC simulation.....	92
A.0.1 Toy Monte Calro simulation	92
A.0.2 Test non-flow effects by impose jets from PYTHIA into ToyMC .	98
Chapter B. Choosing weight for event average	103
Chapter C. Jet energy loss as function of path-length	106
C.1 Basic motivation.....	106
C.2 Analysis	106
C.2.1 Inclusive R_{AA}	106
C.2.2 Elliptic flow.....	107
C.2.3 R_{AA} as function of $\Delta\phi$	107
C.2.4 Path-length calculation with Glauber model	108

C.3	Result	109
C.3.1	$R_{AA}(p_T, \Delta\phi)$	109
C.3.2	Convert $\Delta\phi$ to path-length.....	110
C.3.3	Path-length dependence of R_{AA}	110
C.4	Summary	112
References	114

List of Figures

Figure 1.1 A schematic phase diagram of QCD matter [1]	4
Figure 1.2 Schematic light cone diagram of the evolution of a high energy heavy ion collision	6
Figure 1.3 Schematic sketch of transverse projectile view of the non-central collision [2]. The matter created in the collision (red) is called the participant region. The nucleons in the blue region are called spectators. The grey plane in the left figure is called the reaction plane.	12
Figure 1.4 The created initial transverse energy density profile and its time dependence in coordinate space for a non-central heavy-ion collision [3] As shown in the bottom figure, the anisotropy of space(ϵ_x) coordinate becomes smaller over time, while the momentum anisotropy of momentum space (ϵ_p) increases as system expand as time goes.	13
Figure 1.5 The illustration of the elliptic flow development in the two extreme cases: a large and small mean free path among the produced particles in the left and right images, respectively [4].	14
Figure 1.6 The transverse profile in a single event simulated using the Monte Carlo Glauber model [5, 6]. (left) Green circles are the positions of the nucleon-nucleon collisions. The 2nd harmonic event plane is slightly inclined around the reaction plane. (right) It also has a non-zero triangle anisotropy. The azimuthal angle of the triangle anisotropy, i.e., the 3rd event plane angle Ψ_3 is not correlated to the reaction plane.....	15
Figure 1.7 The published results of flow with ALICE Pb + Pb $\sqrt{S_{NN}} = 2.76$ TeV with various methods [7].....	24

Figure 1.8 Transverse momentum dependence of nuclear modification factor R_{AA} for charged particles produced in heavy ion collisions at SPS, RHIC, and LHC [8].....	25
Figure 1.9 The two event plane correlators by using two subevent groups by ATLAS collaboration. $\langle \sum \Phi \rangle \equiv \langle jk(\Phi_n - \Phi_m) \rangle$. Results from the AMPT model calculation via the SP method(solid line) and the EP method(dashed line) for represent for comparison [9].....	29
Figure 1.10 Measurement of v_4 with different methods as a function of p_T for the indicated centrality bins. The event plane method with its own event plane(red circle) and the event plane method with 2nd order event plane (blue diamonds) are drawn together.[10]	30
Figure 2.1 Schematic view of Large Hadron Collider.....	32
Figure 2.2 Schematic view of ALICE detector [11].....	33
Figure 2.3 ALICE Inner Tracking System(ITS), includes Silicon Pixel Detector(SPD) and Silicon Drift Detector(SDD) and Silicon Strip Detector(SSD)	34
Figure 2.4 ALICE Time Projection Chamber	37
Figure 2.5 ALICE VZERO detectors on both side of TPC	38
Figure 2.6 Picture of general schema of the AliRoot architecture [12]	41
Figure 3.1 Ratio of $dN/d\eta$ for flip over +/- η region(left) and χ^2/NDF for ϕ flatness as function of RunID	44
Figure 3.2 χ^2/NDF for ϕ flatness for $\eta < 0$ (left) and $\eta > 0$ (right).....	45
Figure 3.3 Results of $SC(3, 2)$ (left) and $SC(4, 2)$ before auto (self)-correlation correction(open makers) and after correction(closed markers)	51
Figure 3.4 Scaled ratio of $dN/d\phi$ distribution of ALICE LHC10h dataset to flat distribution (AMPT True). The reconstructed AMPT, and LHC11h with TPC only track cut, and LHC10h with Global SSD track cut were also drawn together for comparison.	53
Figure 3.5 Z-vertex distribution of ALICE Pb + Pb $\sqrt{S_{NN}} = 2.76$ TeV with minimum bias triggered events	55

Figure 3.6 The 2-dim distribution of TPC multiplicity and Global multiplicity.	
Left is the before exclude outlier(left) and right figure is after exclude outlier(right) events.	56
Figure 3.7 χ/NDF of $dN/d\varphi$ distribution from ALICE LHC10h data with TPC only track selection filter and Global SDD filter.	57
Figure 3.8 Tracking efficiency of single particle reconstruction as a function of p_T (left) and contamination of single particle as a function of p_T (right) for ALICE with various track selection filter.....	59
Figure 4.1 The results of $SC(3, 2)$ (blue) and $SC(4, 2)$ (red) with ALICE Pb+Pb $\sqrt{S_{NN}} = 2.76\text{TeV}$ as function of collision centrality (Top). The $NSC(m, n)$ results which scaled with $\langle v_m^2 \rangle \langle v_n^2 \rangle$ were placed in Bottom. The dashed lines are hydrodynamic prediction from H. Niemi with various η/s parametrizations [13]	62
Figure 4.2 The result of SC(3,2) and SC(4,2) with HIJING simulations. Defaults($0.2 < p_T < 5.0\text{GeV}/c$) are drawn as full square with blue color, and different minimum cut conditions are listed in legend. A small shifts along the x axis were applied for better visibility.....	63
Figure 4.3 $NSC(m, n)$ (red) and $NSC(m, n)_\epsilon$ (correlation in coordinate space) by using MC-Glauber models with wounded nucleon (WN) and binary collisions (BC) weights.....	66
Figure 4.4 The result of $SC(3, 2)$ and $SC(4, 2)$ with ALICE data and comparison to various AMPT simulations with different settings. The upper figures are the results of $SC(m, n)$ and the lower figures are the results of $NSC(m, n)$	68

Figure 4.5 Result of $SC(3, 2)$ (left) and $SC(4, 2)$ (right) with LHC10h data and various VISH2+1 calculation with different settings. The three initial conditions from AMPT, KLN, and Glauber simulations are drawn as a different color. Furthermore, the hydrodynamic properties of η/s are shown as line style, the small share viscosity ($\eta/s=0.08$) are shown as solid line, and large share viscosity ($\eta/s=0.2$ for KLN and Glauber, 0.16 for AMPT) is drawn as dashed line. Upper figures are the result of $SC(m, n)$ and lower figures are results of $NSC(m, n)$	70
Figure 4.6 The results of $SC(m, n)$ (upper figure) and $NSC(m, n)$ (bottom figure) with higher order up to 5th flow harmonics with q-Cumulants method from ALICE Pb+Pb $\sqrt{S_{NN}} = 2.76$ TeV. Note that The lower order $SC(m, n)$ are scaled down by 0.1. Both $SC(m, n)$ and $NSC(m, n)$ with lower orders are drawn as colored band and statistical and systematical errors were quadratically merged.	73
Figure 4.7 The results of higher order $NSC(m, n)$ and comparison to MC-Glauber models and prediction from J.Y Ollitraults [14]	74
Figure 4.8 The results of $SC(5, 2)$, $SC(5, 3)$ and $SC(4, 3)$ and comparison to various AMPT simulations with different settings. Upper figures are the results of $SC(m, n)$ and the lower figures are the results of $NSC(m, n)$.	75
Figure 4.9 Result of $SC(5, 2)$, $SC(5, 3)$ and $SC(4, 3)$ with ALICE data and comparison to various VISH2+1 calculation with different settings. The configurations are same as Fig.4.5	76
Figure 4.10 The results of $SC(3, 2)$ and $SC(4, 2)$ with various minimum p_T cut conditions(Top) and results of $NSC(3, 2)$ and $NSC(4, 2)$ (Middle). The ratio of $NSC(m, n)$ results with various minimum p_T cut conditions to default($0.2 < p_T < 5.0$ GeV/c) are shown in bottom figure.....	78
Figure 4.11 The results of $SC(3, 2)$ and $SC(4, 2)$ with various minimum p_T cut conditions(Top) and results of $NSC(3, 2)$ and $NSC(4, 2)$ (Middle). The ratio of $NSC(m, n)$ results with various minimum p_T cut conditions to default($0.2 < p_T < 5.0$ GeV/c) are shown in bottom figure.	79

Figure 4.12 $NSC(3, 2)$ (Top) and $NSC(4, 2)$ (Bottom) as a function of minimum p_T cuts with ALICE Pb+Pb $\sqrt{S_{NN}} = 2.76\text{TeV}$. The AMPT simulation results are drawn together as colored band for comparison. The corresponding AMPT configurations are shown in legend.	80
Figure 4.13 Comparison of $SC(m, n)$ (Top) and $NSC(m, n)$ (Bottom) results for $SC(3, 2)$ (blue) and $SC(4, 2)$ (red) with the SP and QC method up to 60% centralities. The different ratios are shown in lower pads, and systematic uncertainty is drawn as a band around 1	83
Figure 4.14 Result of higher order $SC(m, n)$ and $NSC(m, n)$ with two different method. Along x-axis offset was applied for better visibility. For the QC method $ \eta < 0.8$ cut was applied, while SP method takes $0.4 < \eta < 0.8$. .	84
Figure 4.15 $SC(m, n)$ and $NSC(m, n)$ with SP method with default cuts ($0.2 \leq p_T \leq 5.0\text{ GeV}/c$) and various minimum p_T cuts up to $0.7\text{ GeV}/c$	85
Figure 4.16 $SC(m, n)$ and $NSC(m, n)$ with SP method with default cuts ($0.2 \leq p_T \leq 5.0\text{ GeV}/c$) and various minimum p_T cuts up to $1.5\text{ GeV}/c$).....	86
Figure 4.17 The ratio of $NSC(m, n)$ with SP method to the default cuts	87
Figure A.1 Flow measurement with ALICE at $\sqrt{S_{NN}} = 2.76\text{TeV}/c$ and $5.02\text{TeV}/c$ with various measurement methods, also hydrodynamic predictions are drawn as bands	96
Figure A.2 Results of ToyMC simulation for SC(3,2) with random uniform distribution of v_n with various multiplicity. The left figure is the result from 50 to 450 multiplicity, and right figure is the result from 500 to 1800 multiplicity. Both Q-cumulatns(QC) and Scalar Product(SP) mehtods are tested and drawn with red and blue color marker. Also ratio to input values are drawn in bottom pad, and the ratio of SP / QC methods are drawn with green marker	97

Figure A.3 Results of ToyMC simulation for SC(4,2) with random uniform distribution of v_n with various multiplicity. The left figure is the result from 50 to 450 multiplicity, and right figure is the result from 500 to 1800 multiplicity. Both Q-cumulatns(QC) and Scalar Product(SP) mehtods are tested and drawn with red and blue color marker. Also ratio to input values are drawn in bottom pad, and the ratio of SP / QC methods are drawn with green marker	98
Figure A.4 Event by Event Flow harmoics distributions from Bessel Gaussian function based on [?].....	99
Figure A.5 Results of ToyMC simulation for SC(m,n) with Bessel Gaussian like distribution, Both SP and QC results were performed and the ratio of two different methods are show in bottom pad	100
Figure A.6	101
Figure A.7 The ToyMC results of SC(3,2) (left) and SC(4,2) (right) from 400 to 1800 multiplicity. The input values are drawn as green line. Closed markers are the results with SP and QC results without jet implementation(as same as previous results) and open markers are the results after PYHTHIA jet embedding. The ratio to the input values are drawn in bottom pad	102
Figure C.1 Basic concept of definition of path-length for given angle $\Delta\phi$ (top), and results for centrality 00-10% and 40-50%(bottom). Open symbols are path-length which is calculated from Eq.C.7. Closed symbols are length from center to edge of region.....	109
Figure C.2 R_{AA} versus $\Delta\phi$ for LHC experiment for given p_T bins. Statistical errors and systematical errors are evaluated quadratic.	111

Figure C.3 Geometrical simulation result of path length calculation vs angle with respect to reaction plane by using TGlauber simulation for ALICE(open symbols) and PHENIX(closed symbols), plotted for the six centralities as shown in legend. The angle respect to reaction plane, $\Delta\phi$ is for the center of the bins(7.5, 22.5, 37.5, 52.5, 67.5 and 82.5) and centrality dependent offset is introduced for visual clarity	112
Figure C.4 R_{AA} versus Path-length correspond to $\Delta\phi$ for LHC experiment for given p_T bins. Statistical errors and systematical errors are evaluated quadratic.	113
Figure C.5 Comparison of R_{AA} as function of path length for ALICE and PHENIX with 7~8 GeV/ c p_T bin	114

List of Tables

Table 3.1	ALICE Track selection filter conditions	57
Table 3.2	Systematic uncertainties of $SC(m, n)$. Overall systematics are quadratically merged results of each individual systematic error	60
Table 3.3	Systematic uncertainties of $NSC(m, n)$. Overall systematics are quadratically merged results of each individual systematic error	60
Table 4.1	Configurations of AMPT simulation dataset which correspond to ALICE LHC10h data with Pb+Pb $\sqrt{S_{NN}} = 2.76\text{TeV}$	69

ABSTRACT

Study of correlation between flow harmonics in Heavy Ion collisions at $\sqrt{s_{NN}} = 2.76 \text{ TeV}$ with ALICE at LHC

Myunggeun Song

Physics Department

The Graduate School, Yonsei University, Seoul, Korea

How did the universe begin? Relativistic heavy-ion collisions can answer this question since it can produce an extreme state of very hot and dense system similar to the state just after the Big Bang.

The existence of QGP (Quark-Gluon-Plasma) at extreme conditions such as high temperature and energy density was proved by the Relativistic Heavy Ion Collider (RHIC) at BNL and Large Hadron Collider (LHC) at CERN. One of the most important probes to assess the properties of QGP is collective behavior of particle production in the plane transverse to the beam direction. These phenomena were analyzed with Fourier's series transformations. Each order of Fourier harmonic coefficient is called “flow”(v_n). This flow can provide not only evidence of existence of QGP, but also the properties of the QGP.

The large v_2 (also known as “elliptic flow”) discovered at RHIC energies (and also found at LHC energy) were explained by pressure gradients of the almond-like shape

of the collision overlap region. It was also demonstrated that the QGP behaves like a strongly coupled liquid with a very small ratio of the shear viscosity-to-entropy density (η/s). In this thesis the recent results of studies about flow and the few representative methods to measure flow are reviewed in Section 1.4.

The other harmonics, such as odd and higher harmonics were explained as the result of fluctuation of initial geometry. However, this simple geometrical flow approach cannot explain the possible relation between two different flow harmonics. To measure and quantify the correlation between flow harmonics, new multi particle observables, so called *Symmetric Cumulants* have been introduced. These observables are particularly robust against few-particle non-flow correlations and have no dependence on event planes.

The results of *Symmetric Cumulants* between different order flow harmonics in Pb-Pb collisions at $\sqrt{s_{NN}} = 2.76$ TeV with ALICE detector at the Large Hadron Collider (LHC) and their transverse momentum dependence are presented. The results also are compared to model simulations from viscous hydrodynamics, AMPT, and HIJING models.

Together with existing measurements of individual flow harmonics, this analysis aims to better determine the initial conditions and η/s as the transport properties of the system produced.

Key words : LHC, ALICE, Flow, Correlation, Fluctuation, elliptic flow(v_2),
 $SC(m, n)$

¹ Chapter 1

² Introduction

³ One of the main goals of relativistic heavy ion collision experiments is to discover
⁴ the confinement state, which is often called *Quark – Gluon – Plasma* (QGP). Study of
⁵ the properties of QGP status, such as equation of state, temperature, order of the phase
⁶ transition, transport coefficient, and chemical evolution leads to a deeper understand-
⁷ ing of dominant physics of heavy ion collision experiments. In this chapter, the basic
⁸ motivation of heavy ion collision experiments and the measurement of the azimuthal
⁹ correlation are introduced.

¹⁰ 1.1 Quantum Chromo Dynamics (QCD)

¹¹ *Quantum chromodynamics* (QCD) is a fundamental theory relating to strong in-
¹² teractions between the quarks and gluons. QCD was developed as an extension of quan-
¹³ tum electrodynamics(QED) by the imposition of a local SU(3) symmetry in “color”
¹⁴ space. The color confinement refers to the fact that quarks and gluons cannot be isolated
¹⁵ and therefore cannot be observed directly. Quarks are confined within colorless particles
¹⁶ called hadrons. Mesons are composed of quarks and anti-quarks ($q\bar{q}$), and baryons are
¹⁷ composed of three quarks (qqq or $q\bar{q}q$). The Strong interaction is governed by

$$V(r) = -\frac{4}{3}\frac{\alpha_s}{r} + kr, \quad (1.1)$$

¹⁸ Where α_s is the coupling strength, and k is the string tension. The second term in Eq.1.1
¹⁹ shows that as the distance increases the attractive force increases, this force prevents the

isolation of quarks. Therefore, all quarks are confined within hadrons, and not one can be observed as a free quark in nature. For example, when the distance between a quark-antiquark pair in a meson is increased by inserting more and more energy in the system, at some point it becomes more energetically favorable to produce a new quark-antiquark pair from the vacuum, which will then with the original quark-antiquark pair combine and form two new mesons, preventing in turn the quarks and antiquarks from original meson to be deconfined and to be found isolated.

The most important difference between QCD and QED is that QCD is a non-Abelian gauge theory and self-interacts with gluon as a consequence. The QCD interactions among quarks and gluons become weaker at high energy (called “asymptotic freedom”), while the quarks and gluons are confined inside the hadrons at low energy [15, 16]. The strong coupling constant α_s can be expressed as a function of the momentum transfer Q^2 , as follows:

$$\alpha_s(Q^2) \sim \frac{12\pi}{(33 - 2N_f) \ln(Q^2/\lambda_{QCD}^2)} \quad (1.2)$$

33

where N_f is the number of quarks flavors and $\lambda_{QCD} \sim 0.2\text{GeV}$ is a typical QCD scale. When the momentum transfer Q^2 is large enough when compared with λ_{QCD}^2 , the α_s becomes small enough to allow the use of the perturbative method for QCD calculation (pQCD) as like in the QED [17]. On the other hand, when Q^2 is not large enough, QCD remains in a non-perturbative regime.

39 1.2 Quark Gloun Plasma (QGP)

According to the “Standard Model” quarks interact via a strong nuclear force which is carried by other elementary particles called gluons. The physical quantity for the strong interaction is ‘color’, which comes in three instances: red, blue and green, and the corresponding negative units (“anti-red”, “anti-blue”, and “anti-green”). Quarks carry only a single positive (negative) unit of color, while gluons carry the set of colors, i.e., they carry one positive and one negative unit of color. Since the strong interaction be-

46 tween quarks is transmitted via gluons, which carry only a discrete number of colors
47 (gluons, for instance, do not have mass, charge, or flavor), the strong interaction only
48 can change the color of the interacting quarks. For this reason the underlying fundamen-
49 tal theory of strong nuclear reaction is called “*Quantum Chromodynamics*” (QCD).

50 At ordinary temperatures and energy densities, normal matter is confined within a
51 radius that corresponds to the QCD scale. However, at a sufficiently high temperature
52 (or energy density), the color confinement can be broken. This phase transition from the
53 confined nuclear matter to a deconfined state is the main subject of heavy ion collision
54 physics.

55 In relativistic heavy ion collision, the hadrons start to “melt” into deconfined quarks
56 and gluons. These transitions are predicted by Lattice QCD calculations [18] and pro-
57 duce Quark Gluon Plasma (QGP) as the state of matter consisting of deconfined quarks
58 and gluons (And Plasma is a general term used for physical system in which charges are
59 screened due to the presence of other mobile charges). This QGP status is considered
60 to have existed in the early universe, a few microseconds after the Big Bang [19, 20].
61 The Lattice QCD calculation predicts that the phase transition to a QGP state occurs at a
62 critical temperature T_c around $150 \sim 200$ MeV [21]. This phase transition temperature
63 might be reached in heavy-ion collisions currently delivered at RHIC with Au-Au colli-
64 sions at a center of mass energy of 200 GeV per nucleon pair, and at LHC with Pb-Pb
65 collision at a center of mass energy of 2.76 TeV per nucleon pair. The schematic phase
66 diagram of QGP matter is illustrated in Fig.1.1, where the horizontal axis is the baryon
67 density and the vertical axis is the temperature.

68 **1.3 Heavy ion collision**

69 As mentioned above, the universe started from a single point at approximately 14
70 billion years ago (Big Bang), and expanded and cooled down. During this expansion,
71 the transition from a QGP phase to a hadronic phase happened which allowed for the
72 formation of hadrons. To study this procedures, we collide heavy-ions at ultra-relativistic
73 energies, where one creates QGP matter in the laboratory under controlled conditions.

74 The first heavy-ion experiment was done at the Bevalac experiment at Lawrence

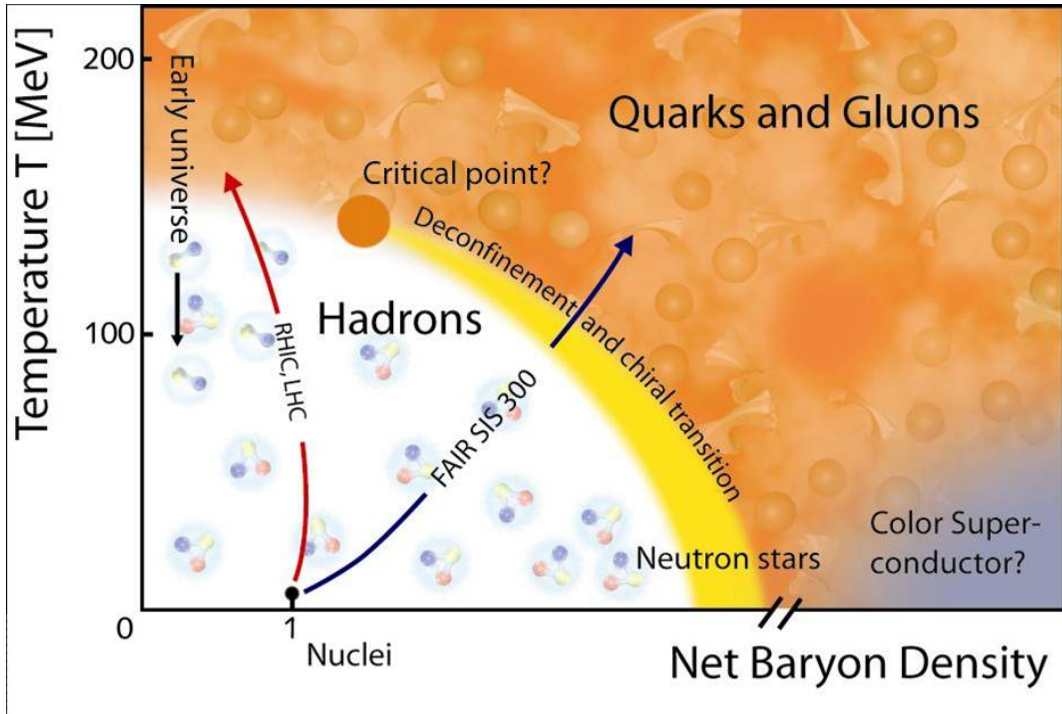


Figure 1.1: A schematic phase diagram of QCD matter [1]

75 Berkeley National Laboratory [22] and at the Joint Institute for Nuclear Research in
 76 Dubna [23] with 1 GeV energy per nucleon. In 1986, the Super Proton Synchrotron
 77 (SPS) at CERN started with 19.4 GeV energy per nucleon pair ($\sqrt{s_{NN}}$) [24]. At these
 78 energies, no decisive evidence of the existence of QGP were found. In 1994, a heavier
 79 lead (Pb) beam was introduced for new experiments and energy per nucleon pair in-
 80 creased up to 17 GeV. At the same time, the Alternating Gradient Synchrotron (AGS) at
 81 BNL collided ^{32}S ion with a fixed target at energies up to 28 GeV [25]. Hints of QGP
 82 were already seen at SPS. Although the discovery of a new state of matter was reported
 83 at CERN, these experiments provided no conclusive evidence of QGP. Now SPS is used
 84 with 400 GeV proton beams for fixed-target experiments, such as the SPS Heavy Ion
 85 and Neutrino Experiment (SHINE) [26], which tries to search for the critical point of
 86 strongly interacting matter. The Relativistic Heavy Ion Collider (RHIC) at BNL started
 87 its operation in 2000. The top center-of-mass energy per nucleon pair at 200 GeV was

88 reached in the following years. The results from the experiments at RHIC have provided
89 a lot of convincing evidences that QGP was created. [27, 28]

90 In the LHC experiment, the heavy ions are accelerated up to almost the speed of
91 light and collide with each other. LHC started operating in November 2009 with proton-
92 proton collisions. First Pb-Pb heavy-ion runs started in November 2010 with $\sqrt{s_{NN}} =$
93 2.76 TeV, an energy that is over ten times higher than at RHIC.

94 In this relativistic heavy ion collision, the initial energy density participating in the
95 collision is expected to be well above the threshold for the QGP formation [29]. In a
96 canonical picture of the collision [3] the system evolution can be divided into several
97 stages, as shown in Fig.1.2

- 98 1. Initial state
- 99 2. thermalized QGP
- 100 3. hadronic gas
- 101 4. chemical freeze-out
- 102 5. kinetic freeze-out(free streaming)

103 At first, the two nuclei traveling at relativistic speeds become longitudinal Lorentz-
104 contracted disks. A large number of the collisions between participants in target and
105 projectile nuclei occur, and it is expected that the produced partons are strongly coupled
106 with each other and thermalized into the QGP phase rapidly within a short time (less
107 than a few fm/c). After $\sim 20\text{fm}/c$ the temperature of the expanding medium drops down
108 below the critical temperature T_c [30]. The quarks and gluons become confined into
109 hadrons. Afterward, the expansion (and the temperature fall) leads to a reduction of
110 the inelastic processes among hadrons, until the relative abundance of hadron species
111 is fixed (chemical freeze-out), and then to the stop of any interaction which fixes the
112 kinetic spectra (kinetic freeze-out).

113 To verify the existence of the phase transition and the formation of QGP in heavy ion
114 collisions, physics observables should be identified for each stage of dynamical evolution

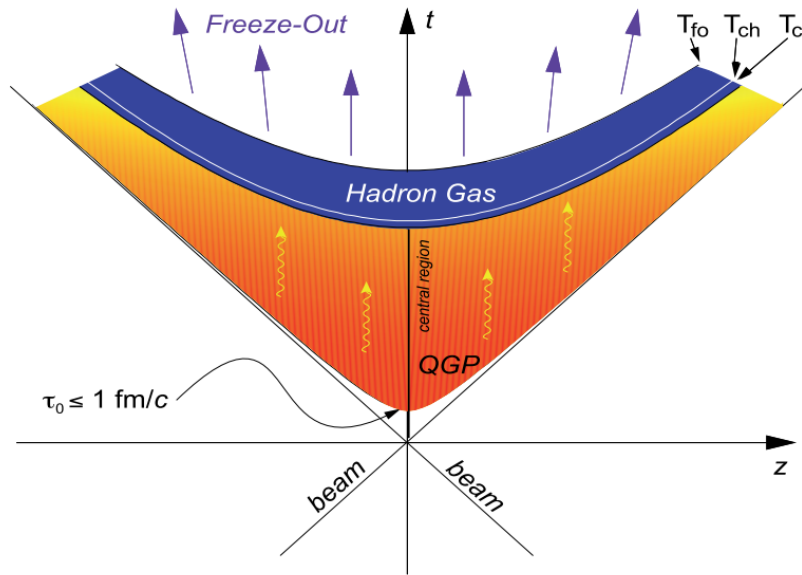


Figure 1.2: Schematic light cone diagram of the evolution of a high energy heavy ion collision

115 of the produced medium. Ordered in sequence of their formation in the course of the
 116 dynamics, the most relevant observables are characterized as follows:

- 117 • Suppression of heavy quarkonia production by Debye screening in the QGP
- 118 • Suppression of di-jets by losing their energy in the medium, so the undisturbed
 119 parton form a jet while the other one is absorbed in the medium and not detected
 120 (or distorted)
- 121 • High- p_T particles produced in primordial $\hat{q}q, \hat{g}g, \hat{q}\bar{q}$ reactions with high momen-
 122 tum transfer are attenuated by gluonic bremsstrahlung in QGP medium
- 123 • Hydrodynamics collective motion develops with the onset of thermal equilibrium
- 124 • Hadronic chemical freeze-out fixes the abundance ratios of the species
- 125 • Two particle Bose-Einstein-Correlations (the HBT effect of quantum optics) re-
 126 sulted from the kinetic freeze out stage

127 Notably, the QGP matter collectively expand both in the longitudinal and the trans-
 128 verse direction. The transverse expansion leads the collectivity motion of system, which
 129 is often called the flow. The produced particles gain the momentum and energy from the
 130 radial flow of the QGP matter, and a final distribution of the transverse momentum is
 131 modified from the superposition of the independent nucleon-nucleon collisions [31].

132 1.4 Flow

133 Introduction

134 In previous section, the phase transition is expected to occur at $T_c \sim 150$ MeV, corre-
 135 sponding to an energy density of $\epsilon_c \simeq 0.15 - 0.5$ GeV/fm³ [32], which could be already
 136 be achieved at RHIC or LHC energies. Thus, experimental measurements in relativis-
 137 tic heavy ion collisions could shed light on the properties of the QGP. The main goal
 138 of studying relativistic heavy ion collisions is to discover and understand its properties
 139 of created matter. The system produced in relativistic heavy ion collisions dynamically
 140 evolves within a time duration of the order of fm/c. Therefore one has to describe the
 141 space-time evolution of thermodynamic variables to fill the large gap between the static
 142 aspects of QGP properties and the dynamical aspects of heavy ion collisions, and hydro-
 143 dynamics plays an important role in connecting them. Hydrodynamics is thus applied to
 144 matter under local equilibrium in the intermediate stage.

145 Also by using hydrodynamics, we can remove QCD Lagrangian density

$$\mathcal{L} = \bar{\psi}_i (i\gamma_\mu D_{ij}^\mu - m\delta_{ij}) \psi_j - \frac{1}{4} F_{\mu\nu\alpha} F^{\mu\nu\alpha} \quad (1.3)$$

146
 147 where ψ_i is a quark field, γ are Dirac matrices, D is a covariant derivative, m is a
 148 quark mass, δ is the Kronecker delta symbol, and F is the field strength of the gluons.
 149 In spite of simple looking of QCD Lagrangian form, it is very difficult to make any
 150 predictions directly from QCD due to its complexity which mainly arises from the non-
 151 linearity of the interactions of the gluons, the strong coupling, the dynamical many body
 152 system and confinement. In hydrodynamics, however, as a phenomenological theory, we

153 can express the equation of state as follows:

$$P = P(e, n) \quad (1.4)$$

154

155 which expresses the pressure P as a function of energy density e and the baryon
156 density n . Such an equation can be obtained by performing numerical simulations of
157 QCD on the lattice. To calculate the above equation of the states, it is also necessary
158 to use additional transport coefficients such as shear viscosity η , bulk viscosity ζ , heat
159 conductivity λ , etc.

160 Hydrodynamics can also produce outputs, such as local temperature or energy den-
161 sity, that could be useful in describing the dynamics for other observables. For instance,
162 in the current formalism of jet quenching, one needs information regarding parton den-
163 sity or energy density along a trajectory of an energetic parton.

164 Hydrodynamics also provides information regarding bulk matter. Therefore we can
165 say that, in the context of relativistic heavy ion collisions, hydrodynamics is the heart
166 of the dynamical modeling since it not only describes expansion and collective flow of
167 matter, but also provides important information about the intermediate stage for other
168 phenomena.

169 Formal definitions

170 The particle azimuthal distribution($r(\varphi)$) is a periodic quantity (over 0 to 2π in polar
171 coordinate), and it can be expand with customary expressed in a Fourier series [4, 33],

$$r(\varphi) = \frac{x_0}{2\pi} + \frac{1}{\pi} \sum_{n=1}^{\infty} [x_n \cos(n\varphi) + y_n \sin(n\varphi)] \quad (1.5)$$

172

173 where, Fourier coefficient x_n, y_n is defined as

$$x_n = \int_0^{2\pi} r(\varphi) \cos(n\varphi) d\varphi \quad (1.6)$$

$$y_n = \int_0^{2\pi} r(\varphi) \sin(n\varphi) d\varphi \quad (1.7)$$

175

176 For our case, the multiplicity is finite, therefore x_n and y_n are changed into finite
 177 sum as like

$$x_n = \sum_{\nu} r_{\nu} \cos n\phi_{\nu} \quad (1.8)$$

178

$$y_n = \sum_{\nu} r_{\nu} \sin n\phi_{\nu} \quad (1.9)$$

179

180 r_{ν} is weight for particle, and usually it takes unity($r_{\nu} = 1$) for inclusive flow mea-
 181 surement. If there is no flow effect and fluctuation, the azimuthal distribution $r(\varphi)$
 182 should be const. i.e. isotropic multiplicity for all angles, and all the coefficient of sin
 183 and cos terms will be vanished. On the other hand, if there are any anisotropic effect,
 184 coefficient x_n and y_n will survive.

185 If we define the v_n , and ψ_n for each corresponding Fourier's harmonics in the fol-
 186 lowing way:

$$v_n \equiv \sqrt{x_n^2 + y_n^2} \quad (1.10)$$

187

$$0 \leq \psi_n \leq \frac{2\pi}{n} \quad (1.11)$$

188

189 we can now express azimuthal particle distribution with v_n and ψ_n instead of x_n and
 190 y_n .

191

$$x_n = v_n \cos n\psi_n \quad (1.12)$$

$$y_n = v_n \sin n\psi_n \quad (1.13)$$

192

193 If we put back x_n and y_n into original Eq.1.5 then

$$\frac{dN}{d\phi} = \frac{x_0}{2\pi} + \frac{1}{\pi} \sum_{n=1} (v_n \cos n\psi_n \cos n\phi + v_n \sin n\psi_n \sin n\phi) \quad (1.14)$$

$$= \frac{x_0}{2\pi} + \frac{1}{2\pi} \sum_{n=1} (2v_n \cos n(\phi - \psi_n)) \quad (1.15)$$

194

195 From Eq.1.14 to 1.15, the sinus terms were vanished because of symmetry of the
 196 collision. As illustrated in Fig.1.3, if the colliding nuclei are the same, the probability
 197 for a produced particles to be emitted in direction φ and $-\varphi$ is equal. As defined in
 198 Eq.1.9, y_n is average of $\langle \sin(n\varphi) \rangle$, and this average of sinus term will be canceled each
 199 other of any angle φ with its symmetries

$$\sin(n\varphi) + \sin(n(-\varphi)) = \sin(n\varphi) - \sin(n\varphi) = 0 \quad (1.16)$$

200 From Eq.1.15, harmonics v_n can be related explicitly to the origin azimuthal distri-
 201 bution $r(\varphi)$ in the following way:

$$\langle \cos(n\varphi) \rangle \equiv \frac{\int_0^{2\pi} \cos(n\varphi) r(\varphi) d\varphi}{\int_0^{2\pi} r(\varphi) d\varphi} \quad (1.17)$$

$$= \frac{\frac{1}{\pi} v_n \int_0^{2\pi} \cos^2(n\varphi) d\varphi}{v_0} \quad (1.18)$$

$$= \frac{v_n}{v_0} \quad (1.19)$$

202 Using a normalized distribution $r(\varphi)$, for which $v_0 = \int_0^{2\pi} r(\varphi) d\varphi = 1$, the above
 203 equation leads to:

$$v_n = \langle \cos(n\varphi) \rangle \quad (1.20)$$

204

205 The harmonic v_1 is often called “directed flow”, and v_2 called “elliptic flow”, and
 206 v_3 is “triangular flow”. When we consider the polar coordinate with (r, φ) , then the
 207 distribution for ellipse-like is determined by the following equation.

$$r(\varphi) = \frac{a(1 - \varepsilon^2)}{1 + \varepsilon \cos \varphi} \quad (1.21)$$

208

209 where ε is the eccentricity defined as

$$\varepsilon^2 \equiv 1 - \frac{b^2}{a^2} \quad (1.22)$$

210 with definition of a is major, and b is minor axis. With this parameterization, v_n can
211 be calculated analytically in a closed form, as like

$$v_n = 2\pi b(-1)^n \left(\frac{a-b}{a+b}\right)^{\frac{n}{2}} \quad (1.23)$$

212 The methods that attempt to explain the azimuthal distribution of particles produced
213 with customized Fourier's expansion have been succeeded in relativistic heavy ion col-
214 lision, especially in RHIC and LHC, by studying about strong collective and anisotropic
215 flow in the transverse plane driven by the pressure gradients with more particles emitted
216 in the direction of the largest gradients. The large elliptic flow discovered at RHIC en-
217 ergies [34] continuous to increase also in LHC energies [7, 35]. This has been predicted
218 by calculations utilizing viscous hydrodynamics [36, 31, 37, 38, 39, 40].

219 These calculations also demonstrated that the shear viscosity to the entropy density
220 ratio (η/s) of strongly interacting matter is close to a universal lower bound $1/4\pi$ [41]
221 in heavy ion collisions at RHIC and LHC energies.

222 The temperature dependence of the η/s has some generic features that most of the
223 known fluids obey. One such general behavior is that the ratio typically reaches its
224 minimum value close to the phase transition region [42]. It was shown, using kinetic
225 theory and quantum mechanical considerations [43] that $\eta/s > 1/15$ would be an order
226 of magnitude for the lowest possible shear viscosity to entropy ratio in nature. Later it
227 was found that one can calculate an exact lower bound $(\eta/s)_{\min} = 1/4\pi \approx 0.08$ using
228 the AdS/CFT correspondence [41]. Hydrodynamical simulations supports as well the
229 view that the QGP matter indeed is close to that limit [39].

230 In relativistic collision, each collision is characterized by the impact parameter, de-
231 fined as the distance between the center of two nuclei points. Collisions with the short
232 impact parameter are called central collisions and collisions with the long impact pa-
233 rameter are called peripheral collisions. This geometry of the collision moments with
234 non-central collision has ellipticity in the transverse plane and is shown in Fig.1.3

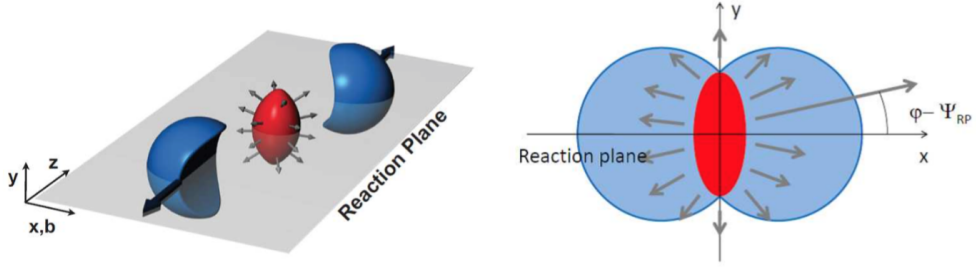


Figure 1.3: Schematic sketch of transverse projectile view of the non-central collision [2]. The matter created in the collision (red) is called the participant region. The nucleons in the blue region are called spectators. The grey plane in the left figure is called the reaction plane.

235 The initial spatial anisotropy in the azimuthal direction is transformed to the anisotropy
 236 of the final particle momentum distributions due to the collective expansion of the pro-
 237 duced system. During evolution of the almond-shaped interaction volume, the anisotropy
 238 in coordinate space is transformed to anisotropy in momentum space (shown in Fig.1.4).
 239 Therefore, these momentum anisotropies of the hydrodynamic matter lead to the anisotropic
 240 azimuthal distribution of the produced particles.

241 However, the transverse expansion of system volume is insufficient to explain the
 242 anisotropy of azimuthal particle distribution. As shown in Fig.1.5, if there is no inter-
 243 action between particles (or the mean free path among the produced particles is much
 244 longer than the typical size of the system), the azimuthal distribution of the particles
 245 does not depend on azimuthal angle on average due to symmetry of the production pro-
 246 cess. On the other hand, when the mean free path is very small compared to the typical
 247 system size, hydrodynamics can be applied to describe the space-time evolution of the
 248 system. Furthermore, the pressure gradient along the horizontal axis is much longer than
 249 the vertical axis due to the geometry.

250 The origin of large v_2 cannot explain other harmonics especially odd number har-
 251 monics like v_3 , v_5 , etc. The impact parameter vector b (the vector connecting the centers
 252 of two colliding nuclei) changes event-by-event, which in turn yields a random reaction
 253 plane angle ψ_R (the plane spanned by the impact parameter and the beam axis). Due

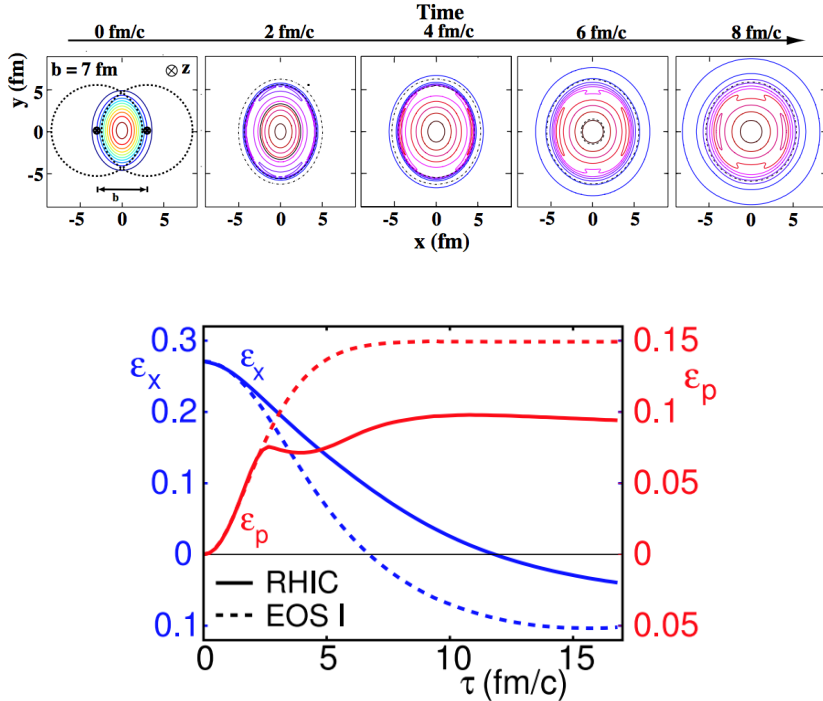


Figure 1.4: The created initial transverse energy density profile and its time dependence in coordinate space for a non-central heavy-ion collision [3]. As shown in the bottom figure, the anisotropy of space (ϵ_x) coordinate becomes smaller over time, while the momentum anisotropy of momentum space (ϵ_p) increases as system expand as time goes.

254 to these random fluctuations, it is not trivial to set up for each event the coordinate sys-
 255 tem. Because of the random geometry of participant nucleon in colliding nuclei, the
 256 overlap region shape is not a perfect almond shape, but rather a complex shape as shown
 257 in Fig.1.6. As a result of this random fluctuation and the complex shape of the energy
 258 density profile of the system, the flow harmonics v_n are defined with their own event
 259 plane ψ_n , not with respect to reaction plane ψ_R . Although the 2nd harmonics symmetry
 260 plane(ψ_2) roughly corresponds to the reaction plane($\psi_2 \sim \psi_R$), their azimuthal angles
 261 are slightly inclined event-by-event. In the following section, methods to calculate flow
 262 will be discussed.

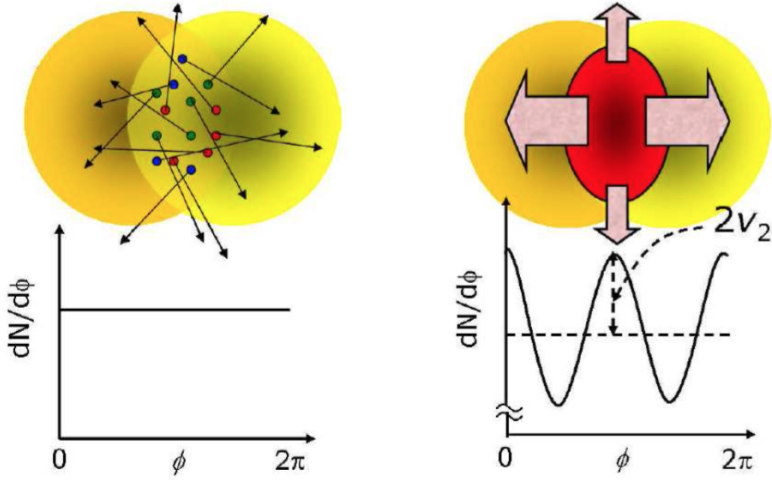


Figure 1.5: The illustration of the elliptic flow development in the two extreme cases: a large and small mean free path among the produced particles in the left and right images, respectively [4].

263 1.4.1 Event Plane method

264 The event plane method (EP) is the most commonly used method to measure anisotropic
 265 flow. Using this method, the event plane is estimated and all particles' azimuthal angles
 266 are correlated to this estimated plane in order to obtain the flow harmonics v_n . From the
 267 Eq.1.13 we can easily calculate event plane angles with the following way:

$$\frac{y_n}{x_n} = \frac{v_n \sin n\psi_n}{v_n \cos n\psi_n} = \tan n\psi_n \quad (1.24)$$

$$268 \quad \psi_n = (\arctan \frac{y_n}{x_n})/n \quad (1.25)$$

269 and by using Fourier's coefficient relation:

$$270 \quad v_n = \langle \cos n(\phi_\nu - \psi_n) \rangle \quad (1.26)$$

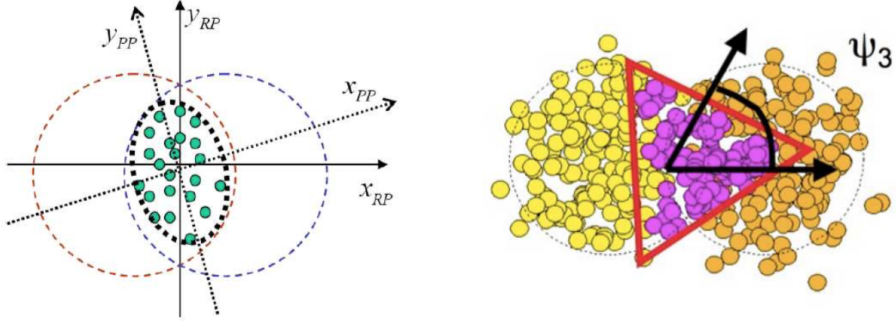


Figure 1.6: The transverse profile in a single event simulated using the Monte Carlo Glauber model [5, 6]. (left) Green circles are the positions of the nucleon-nucleon collisions. The 2nd harmonic event plane is slightly inclined around the reaction plane. (right) It also has a non-zero triangle anisotropy. The azimuthal angle of the triangle anisotropy, i.e., the 3rd event plane angle Ψ_3 is not correlated to the reaction plane

271 However, in practice, since each event has a finite number of created particles, the
 272 results for the event plane angle will be affected by a limited resolution. This can be
 273 corrected for by estimating the event plane resolution:

$$v_n^{measured} = \langle \cos n(\phi - \psi_n^{measured}) \rangle \quad (1.27)$$

274

275 where, $\psi_n^{measured} = \psi_n + \psi_n^{err}$

$$v_n^{measured} = \langle \cos n(\phi - \psi_n - \psi_n^{err}) \rangle \quad (1.28)$$

$$= \langle \cos n(\phi - \psi_n) \cos n(\psi_n^{err}) + \sin n(\phi - \psi_n) \sin n(\psi_n^{err}) \rangle \quad (1.29)$$

$$= \langle \cos n(\phi - \psi_n) \cos n(\psi_n^{err}) \rangle + \langle \sin n(\phi - \psi_n) \sin n(\psi_n^{err}) \rangle \quad (1.30)$$

$$= \langle \cos n(\phi - \psi_n) \rangle \langle \cos n(\psi_n^{err}) \rangle \quad (1.31)$$

$$= v_n \langle \cos n(\psi_n^{err}) \rangle \quad (1.32)$$

276 Finally, we get

$$v_n = v_n^{measured} / \langle \cos n(\psi_n^{err}) \rangle \quad (1.33)$$

277

278 We assume that event angle error(ψ_n^{err}) is independent of $\phi - \psi_n$, and the expectation
 279 value of $\sin n(\psi_n^{err})$ is zero. The estimated event plane resolution can be obtained by
 280 two or more independent subevents [44]. The advantage of the event plane method is
 281 that it is less sensitive to the number of particles for analysis, and can therefore be used
 282 to measure flow of rare particles. Furthermore, this method can be used to estimate an
 283 event plane, especially the 2nd order event plane which is expected to be similar to the
 284 reaction plane $\psi_2 \sim \psi_R$. This 2nd event plane also can be used for jet or other analysis.
 285 The main disadvantage of this method occurs when the event plane resolution is affected
 286 by correlations which do not stem from a genuine correlation of all particles with the
 287 true event plane. While event plane resolution can fix errors from multiplicity, it cannot
 288 fix errors originating from non-flow (e.g., jet, detector smearing, etc.).

289 **1.4.2 Scalar product method**

290 The original idea behind the event plane method is that the direction of Ψ_n of the
 291 flow vector in a reference frame provides an estimation of the corresponding angle Φ_n
 292 in the underlying probability distribution. Because a finite sample of particles is used,
 293 statistical fluctuation causes Ψ_n to differ from Φ_n . This dispersion is characterized by
 294 the “resolution”, defined as

$$R \equiv \langle e^{in(\Psi_n - \Phi_n)} \rangle \quad (1.34)$$

$$= \left\langle \frac{Q_n}{|Q_n|} e^{-in\Phi_n} \right\rangle \quad (1.35)$$

295 For the fixed v_n , the above equation can be written in the form of

$$R(v_n) \equiv \left\langle e^{in(\Psi_n - \Phi_n)} \right\rangle_{|vn} \quad (1.36)$$

$$= \left\langle \frac{Q_n}{|Q_n|} e^{-in\Phi_n} \right\rangle_{|vn} \quad (1.37)$$

296 where $\langle \dots \rangle_{|vn}$ indicates an average over a large number of event with the same under-
 297 lying v_n . From the Eq.1.26, we can see underlying probability distribution (Eq.1.5) de-

298 pends on the relative magnitude of the anisotropy v_n to the statistical dispersion $1/\sqrt{N}$.
 299 In the limit $v_n \gg 1/\sqrt{N}$ (large number of multiplicity), easily reconstruct the underlying
 300 event plane so that $\Phi_n = \Psi_n$, (i.e. $R(v_n) \sim 1$, and conversely, when the $v_n\sqrt{N} \ll 1$
 301 (low multiplicity) the Resolution $R(v_n) \sim kv_n$, where k is independent of v_n and scale
 302 as $k \sim \sqrt{N}$.

303 Generally, the value falls somewhere between these limits [45], and this nonlinear
 304 dependence of the resolution on the underlying flow is the origin of the difficulties of the
 305 event plane method.

306 When we obtain the event plane resolution from subevents A and B, the resolution
 307 $R(v_n)$ is a factorization like the below definition:

$$\left\langle \frac{Q_{nA}}{|Q_{nA}|} \frac{Q_{nB}}{|Q_{nB}|} \right\rangle = \left\langle \frac{Q_{nA}}{|Q_{nA}|} e^{-in\Phi_n} \right\rangle \left\langle \frac{Q_{nB}}{|Q_{nB}|} e^{-in\Phi_n} \right\rangle^* \quad (1.38)$$

$$= \left| \left\langle \frac{Q_{nA}}{|Q_{nA}|} e^{-in\Phi_n} \right\rangle_{v_n} \right|^2 \quad (1.39)$$

$$= R(v_{nA})^2 \quad (1.40)$$

308 The Eq.1.37 is used for the second line to third line of the above equation. The event-
 309 plane methods is thus defined as:

$$v_n\{EP\} \equiv \frac{\left\langle Q_n \frac{Q_{nA}^*}{|Q_{nA}|} \right\rangle}{\sqrt{\left\langle \frac{Q_{nA}}{|Q_{nA}|} \frac{Q_{nB}}{|Q_{nB}|} \right\rangle}} \quad (1.41)$$

310

311 Since the measurement has been taken with the average of all events in a given
 312 centrality class, Eq.1.41 changes as term of v_n as like

$$v_n\{EP\} = \frac{\langle v_n R(v_{nA}) \rangle_{v_n}}{\sqrt{\langle R(v_{nA})^2 \rangle_{v_n}}} \quad (1.42)$$

313

314 Note that $\langle R(v_{nA})^2 \rangle \neq \langle R(v_{nA}) \rangle^2$. Resolution correction is no longer a simple
 315 projection of the measured event plane Ψ_n onto the “true” event plane Φ_n .

316 In the limit of infinite multiplicity (i.e. $R(v_n) \sim 1$), $v_n\{EP\}$ does indeed measure
 317 the event averaged mean v_n from Eq.1.5. But in reality, the resolution is not perfect and
 318 the result is usually even closer to the low resolution limit [46], and in this case, the
 319 event-plane measurement thus yields a root-mean-square value. In other words, what
 320 we measure with the event plane method is some values between root-mean-square and
 321 mean of v_n depends on the resolution (i.e. Event multiplicity or the performance and
 322 acceptance of detector)

$$v_n\{EP\} \simeq \langle v_n \rangle \quad (\text{high resolution limit}) \quad (1.43)$$

$$v_n\{EP\} \simeq \sqrt{\langle v_n^2 \rangle} \quad (\text{low resolution limit}) \quad (1.44)$$

323
 324 However, in the scalar product method, which is a slight variant of the event plane
 325 method, consists of removing the factor of $|Q_n|$ before taking the average in the numer-
 326 ator and denominator of Eq.1.41

$$v_n\{SP\} \equiv \frac{\langle Q_n Q_{nA}^* \rangle}{\sqrt{\langle Q_n Q_{nA}^* \rangle}} \quad (1.45)$$

327
 328 Then, by calculating the scalar product in numerator, the fluctuation term (Resolution
 329 related terms) are removed.

$$v_n\{SP\} = \frac{\langle v_n v_{nA} \rangle_{v_n}}{\sqrt{\langle v_n v_{nA} \rangle_{v_n}}} = \sqrt{\langle v_n^2 \rangle} \quad (1.46)$$

330
 331 As a result, the scalar product method always yields the root-mean-square v_n , re-
 332 gardless of the details of the analysis and makes for a superior measurement.

333 **1.4.3 Cumulants method**

334 **Multi particle correlations**

335 Because of the disadvantage of the event plane method (or the scalar product method)
 336 in estimating the event plane, the cumulants method (often called the multi-particle cor-
 337 relation method) was proposed in order to reduce this bias. This method does not require
 338 the event plane estimation event-by-event. Instead, these multi-particle correlations can
 339 be calculated by looping over all possible multiplets. If we assume that all the particles
 340 have azimuthal correlations which originated from flow harmonics only, then 2- and 4-
 341 particle azimuthal correlations can be expressed in the following way:

$$\langle 2 \rangle \equiv \langle e^{in(\phi_1 - \phi_2)} \rangle \equiv \frac{1}{\binom{M}{2} 2!} \sum_{i,j=1, i \neq j}^M e^{in(\phi_i - \phi_j)} \quad (1.47)$$

342

$$\langle 4 \rangle \equiv \langle e^{in(\phi_1 + \phi_2 - \phi_3 - \phi_4)} \rangle \equiv \frac{1}{\binom{M}{4} 4!} \sum_{i \neq j \neq k \neq l}^M e^{in(\phi_i + \phi_j - \phi_k - \phi_l)} \quad (1.48)$$

343

344 where the brackets denote the particle average in a single event. The i, j, k, l denote
 345 identical particles, and ϕ_i is the azimuthal angle of the i -th particle measured in labora-
 346 tory frame. To prevent contribution of self(auto) correlation, the constraints $i \neq j$ and
 347 $i \neq j \neq k \neq l$ have been enforced. When we extend the above equation for event
 348 average, then 2- and 4- particle azimuthal correlations are as follows :

$$\langle \langle 2 \rangle \rangle \equiv \langle \langle e^{in(\phi_1 - \phi_2)} \rangle \rangle \equiv \frac{\sum_{i=1}^N (W_{\langle 2 \rangle})_i \langle 2 \rangle_i}{\sum_{i=1}^N (W_{\langle 2 \rangle})_i} \quad (1.49)$$

349

$$\langle \langle 4 \rangle \rangle \equiv \langle \langle e^{in(\phi_1 + \phi_2 - \phi_3 - \phi_4)} \rangle \rangle \equiv \frac{\sum_{i=1}^N (W_{\langle 4 \rangle})_i \langle 4 \rangle_i}{\sum_{i=1}^N (W_{\langle 4 \rangle})_i} \quad (1.50)$$

350

351 where, N is the number of events, and $W_{\langle 2 \rangle}$ and $W_{\langle 4 \rangle}$ are the event weights. The
 352 selecting event weight is explained in Appendix B. The benefit of using multi-particle
 353 azimuthal correlation is to measure flow harmonics v_n without requiring the event plane
 354 ψ_n ,

$$\langle\langle 2 \rangle\rangle \equiv \langle\langle e^{in(\phi_1-\phi_2)} \rangle\rangle = \langle\langle e^{in(\phi_1-\psi_n-\phi_2+\psi_n)} \rangle\rangle \quad (1.51)$$

$$= \langle\langle e^{in(\phi_1-\psi_n)} \rangle\langle e^{-in(\phi_2-\psi_n)} \rangle\rangle = \langle v_n^2 \rangle \quad (1.52)$$

355 In cases when only flow correlations exist in the system, the correlation among any
 356 two particles is induced through the correlation of each particle with the same event
 357 plane ψ_n [47, 48]. Each of these single particle azimuthal distributions is related to the
 358 flow harmonics via Eq.1.15. Therefore we can show that :

$$\langle\langle 4 \rangle\rangle = \langle v_n^4 \rangle \quad (1.53)$$

$$\langle\langle 6 \rangle\rangle = \langle v_n^6 \rangle \quad (1.54)$$

$$\langle\langle 8 \rangle\rangle = \langle v_n^8 \rangle \quad (1.55)$$

361 and so on, in a similar manner. Crucially, even in an ideal case when there is an
 362 absence of non-flow effects, the cumulants method will be systematically biased due to
 363 flow fluctuation.

$$\langle v_n \rangle^k \neq \langle v_n^k \rangle \quad (1.56)$$

364

365 **Flow fluctuation**

366 The measuring of flow harmonics is paramount to the measuring of the power of
 367 average values of flow harmonics with multi-particle correlation. However, these two
 368 values are not exactly equivalent even in the ideal case, i.e., when there is no non-flow
 369 effect scenario due to unavoidable flow fluctuations. In the following section methods for
 370 quantifying various powers of flow harmonics will be discussed. For better convention,
 371 v_n will be denoted as simply v .

372 First, let's consider the Taylor expansion for arbitrary functions around mean μ_x up
 373 to second order

$$h(x) = h(\mu_x) + (x - \mu_x)h'(\mu_x) + \frac{(x - \mu_x)^2}{2!}h''(\mu_x) \quad (1.57)$$

374

375 If we take the average of given function $h(x)$ then the Taylor expansion can be
 376 expressed as:

$$\langle h(x) \rangle = h(\mu_x) + (\langle x \rangle - \mu_x)h'(\mu_x) + \frac{\sigma_x^2}{2}h''(\mu_x) \quad (1.58)$$

$$= h(\mu_x) + (\mu_x - \mu_x)h'(\mu_x) + \frac{\sigma_x^2}{2}h''(\mu_x) \quad (1.59)$$

$$= h(\mu_x) + \frac{\sigma_x^2}{2}h''(\mu_x) \quad (1.60)$$

377 where,

$$\sigma_x^2 = \int_{-\infty}^{\infty} (x - \mu_x)^2 f(x) dx$$

378

379 As seen in this equation, the expectation value of linear term(first order) in Taylor's
 380 expansion of $h(x)$ around mean μ_x always vanishes. Then we can now estimate the
 381 average of various powers of v from Eq.???. For example, in the case $h(v) = v^2$, it
 382 follows that :

$$\langle v^2 \rangle = \langle v \rangle^2 + \sigma_v^2 \quad (1.61)$$

383 By using the definition of multi- particle correlation (Eq.1.52 to 1.55), we have

$$v\{2\} = \langle v^2 \rangle^{1/2} \quad (1.62)$$

384 Furthermore, by applying the Taylor expansion above (Eq.1.60) for the case $h(v) \equiv$
 385 v^2 , it follows that:

$$\langle v^2 \rangle = (\langle v \rangle^2 + \sigma_v^2)^{1/2} \quad (1.63)$$

$$= \langle v \rangle \left(1 + \frac{\sigma_v^2}{\langle v \rangle^2} \right)^{1/2} \quad (1.64)$$

$$\simeq \langle v \rangle \left(1 + \frac{1}{2} \frac{\sigma_v^2}{\langle v \rangle^2} \right) \quad (1.65)$$

386 For the constraint with:

$$\sigma_v \ll \langle v \rangle \quad (1.66)$$

387 Then we have general results:

$$(1+x)^n \simeq 1 + nx, \quad (1.67)$$

388 valid for $x \simeq 0$, and the final equation can be expressed as like

$$v\{2\} \simeq \langle v \rangle + \frac{1}{2} \frac{\sigma_v^2}{\langle v \rangle} \quad (1.68)$$

389 From this result, we can conclude that the flow estimation with the 2nd order cumulant will be always systematically biased with positive signature due to flow fluctuations.

390 In addition, the four-particle cumulant can be defined similarly. From the definitions

$$v\{4\} = (-\langle v^4 \rangle + 2\langle v^2 \rangle^2)^{1/4} \quad (1.69)$$

392 with Talyer expansion (Eq.1.60) for the case $h(v) \equiv v^4$ we have up to second order
393 in σ_v as

$$\langle v^4 \rangle = \langle v \rangle^4 + 6\sigma_v^2 \langle v \rangle^2 \quad (1.70)$$

394 as same as 2-particle cumulants, it follows that:

$$v\{4\} = \left[-\langle v \rangle^4 - 6\sigma_v^2 \langle v \rangle^2 + 2(\langle v \rangle^2 + \sigma_v^2)^2 \right]^{1/4} \quad (1.71)$$

$$= [\langle v \rangle^4 - 2\sigma_v^2 \langle v \rangle^2 + \mathcal{O}(\sigma_v^4)]^{1/4} \quad (1.72)$$

$$= \langle v \rangle \left(1 - 2 \frac{\sigma_v^2}{\langle v \rangle^2} \right)^{1/4} \quad (1.73)$$

$$\simeq \langle v \rangle \left(1 - \frac{1}{2} \frac{\sigma_v^2}{\langle v \rangle^2} \right) \quad (1.74)$$

(1.75)

395 so, as like $v\{2\}$, the final form is

$$v\{4\} \simeq \langle v \rangle - \frac{1}{2} \frac{\sigma_v^2}{\langle v \rangle} \quad (1.76)$$

396

397 with this final form, we can conclude that the 4- particle cumulant flow results will be
 398 always systematically biased with negative signature due to statistical flow fluctuations.
 399 This is an opposite trend when compared with 2- particle cumulant results (Eq.1.68).
 400 Due to this reason, the $v_n\{2\} < v_n\{EP\} < v_n\{4\}$ and explain the difference between
 401 different flow measurement methods as shown in Fig.1.7.

402 The higher-order cumulants like 6-particle or 8-particle correlation can be calculated
 403 in the same way.

404 1.5 Jet quenching

405 In p - p collisions, hard scattered partons fragment into hadrons with high transverse
 406 momentum, also called as jets. However in heavy-ion collisions, the hard scattering
 407 occurs before the formation of QGP, and the scattered partons will experience the entire
 408 evolution of the system created in these collisions [49]. These partons will interact
 409 strongly with the created medium and loss their energy, and these features are known as
 410 “jet quenching” [50]. This “jet quenching” is the another strong evidence of the existence
 411 of the QGP, because energy loss in a deconfined matter is believed to be much stronger

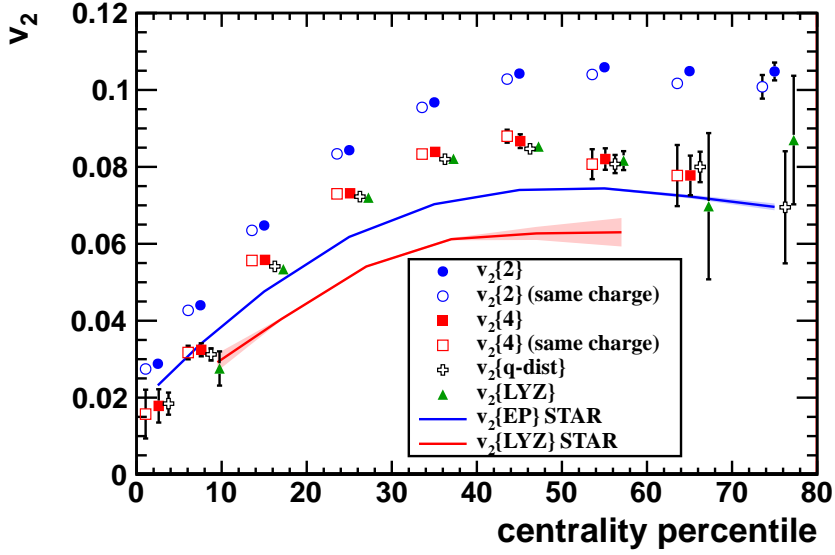


Figure 1.7: The published results of flow with ALICE Pb + Pb $\sqrt{S_{NN}} = 2.76$ TeV with various methods [7].

412 than in hadronic matter [50]. “Jet quenching” is usually observed with the suppression
 413 of high p_T particles yields though the nuclear modification factor R_{AA} , defined as like

$$R_{AA}(p_T) = \frac{dN_{ch}^{AA}(p_T)/dp_T}{\langle N_{coll} \rangle dN_{ch}^{pp}(p_T)/dp_T} \quad (1.77)$$

414 where AA denotes heavy-ion collisions and pp for the p-p collisions. the $dN_{ch}(dp_T)$
 415 refer the number of charged particle produced in each collisions as a function of trans-
 416 verse momentum. The number of binary collisions N_{coll} has been used to compare the
 417 yield of charged particle produced in AA and p-p collisions as scaling factor. This N_{coll}
 418 were calculated by Glauber model, which provide a proper normalization for a given AA
 419 centrality. If there are not any medium effects on AA collisions, the heavy-ion collision
 420 can be regarded as a just simple superposition of nucleon-nucleon collisions (as like p-p)
 421 and nuclear modification factor R_{AA} will be unity. Otherwise, any deviation from unity
 422 of R_{AA} will indicate a certain medium effect of heavy ion collisions.

423 At the energy of SPS, the R_{AA} was slightly lower than unity for $2 < p_T < 3$ GeV/c

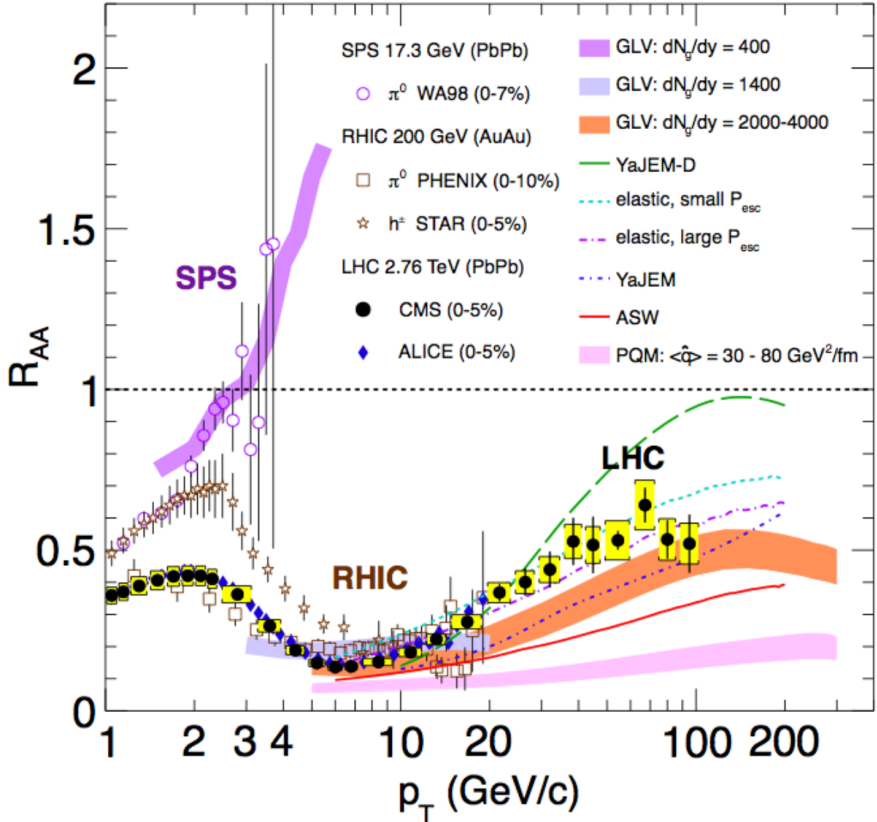


Figure 1.8: Transverse momentum dependence of nuclear modification factor R_{AA} for charged particles produced in heavy ion collisions at SPS, RHIC, and LHC [8].

and almost unity for above p_T [51]. However, at RHIC energy, R_{AA} increase monotonically up to $p_T \sim 3$ GeV/c and then start to decrease. Hadron production for $6 < p_T < 8$ GeV/c is suppressed by a factor of 5 in central Au-Au collision when compare to p-p collisions [52, 53].

Also, at ALICE energy, R_{AA} published in 2010 with the p_T spectra up to 20 GeV/c shows a slightly stronger suppression (about a factor of 7 observed for the p_T range around 6~8 GeV/c) than previous results was reported. This observation was confirmed by CMS Collaborations, which extended to p_T range up to 100 GeV/c. The R_{AA} measurements exhibit a clear increasing trend up to $p_T \sim 40$ GeV/c and then seems to

433 saturate with a value of about 0.5.

434 In addition, the parton energy loss in created medium is increase as the path-length.
435 The path-length which hard scattered parton travels are related to local geometry of
436 create medium. Since in non-central collision the shape of collision regions are formed
437 as like ellipse, the path-length will depend on the azimuthal angles respect to reaction
438 plane angle. For instance, the parton travels along the minor-axis direction (in plane
439 direction) have shorter path-length than the parton emit to the direction of major-axis
440 (out of plane direction). As the results, at high p_T , v_2 is expected to be due to “jet
441 quenching” reflecting the azimuthal asymmetry of the path-length [54].

442 The study of jet energy loss in created medium as function of path-length are per-
443 formed by utilizing $R_{AA}(p_T)$ and $v_2(p_T)$. The path-length as the function of centrality
444 and azimuthal angle respected to 2nd event plane (\sim reaction plane) were estimated from
445 Glauber simulation and details can be found in Appendix C.

446 1.6 Correlation between flow harmonics

447 Since the early 1990s the second order flow(v_2) was studied as one of the most
448 interesting results at RHIC, with Au+Au $\sqrt{S_{NN}} = 200$ GeV collisions. This large signal
449 of the second order “elliptic flow” are explained by the almond shape of the collision
450 overlap region in initial state, and it indicated that a perfect liquid had been made in the
451 early stage of collision. Also detailed studies about flow study report that the fluctuation
452 over event-by-event leads odd number harmonics flow.

453 The anisotropic flow is understood as hydrodynamic response to spatial deformation
454 of the initial density profile. This profile fluctuates event to event due to quantum fluctu-
455 ations of the positions of the constituents inside the colliding nuclei, which implies that
456 the flow also fluctuates [55, 56]. The recognition of the importance of flow fluctuation
457 has led to triangular flow and higher harmonics [57, 58] as well as the correlations be-
458 tween different Fourier harmonics [9]. As the result from ATLAS experiments, it shows
459 that higher order harmonics are sensitive to the η/s [59]. And the v_n distributions carry
460 detailed information about the initial density profile [60, 61].

461 However, difficulties on extracting the shear viscosity in heavy ion has been realized
462 since it strongly depends on the specific choice of the initial conditions [36, 59, 62]. The
463 viscous effects reduce the magnitude of the elliptic flow. Furthermore, the magnitude of
464 η/s used in these calculations should be considered as an average over the temperature
465 history of the expanding fireball while as it is known that η/s of other fluids depends on
466 temperature. In addition, part of the elliptic flow also can originate from the hadronic
467 phase [63, 64, 65]. Therefore, knowledge of both the temperature dependence and the
468 relative contributions from the partonic and hadronic phases should be understood better
469 to quantify η/s of the partonic fluid.

470 The higher harmonics ($n > 3$) are understood as superpositions of linear and nonlin-
471 ear responses, through which they are correlated with lower-order harmonics [66, 67].
472 When the harmonic order is large, the nonlinear response contribution in viscous hydro-
473 dynamics is dominant [66, 67]. The magnitude of the viscous corrections as a function
474 of p_T for v_4 and v_5 are sensitive to ansatz used for the viscous distribution function,
475 δf , a small correction for the equilibrium distribution at hadronic freeze-out when QGP

476 phase has become cool and dilute [68]. Hence the studies of the higher order ($n > 3$) to
 477 lower order (v_2 or v_3) harmonic correlations and their p_T dependence can help to under-
 478 stand the viscous correction to the momentum distribution at hadronic freeze-out which
 479 is probably the least understood part of hydrodynamic calculations [66, 13].

480 Although there have been detailed studies of single flow harmonics in recent decades,
 481 only a few studies discussed correlation between two different flow harmonics. The dif-
 482 ficult part of studying flow correlation is that there are two kinds of correlation between
 483 flows: the correlation between two flow magnitudes ($v_n - v_m$), and the correlation be-
 484 tween two flow directions. i.e., event plane angles correlation for two different flow
 485 harmonics ($\psi_n - \psi_m$).

486 ATLAS Collaboration measured the correlation between different order event plane
 487 angles with two plane or three correlators by using two (three) subevents symmetric
 488 around $\eta = 0$ with a gap in between. With this method, we can expect the same res-
 489 olution for each subevent groups and it provides its own estimate of the event plane
 490 (Fig.1.9). As a result they found a positive correlation between event plane angles as a
 491 function of centrality.

492 CMS Collaboration also reported the correlation between different order event plane
 493 angles by using event plane methods [10], which measure higher-order flow (like v_4, v_5, v_6)
 494 with its own event plane angle, and also with the event plane angle which are measured
 495 from lower harmonics. For example, Fig.1.10 compares the v_4 with its own event plane
 496 angle Ψ_4 (i.e. $v_4\{\Psi_4\}$) and v_4 with 2nd order flow event plane angle Ψ_2 (i.e. $v_4\{\Psi_2\}$).

497 Despite several approaches in studying flow correlations, it is still a challenge to
 498 measure only “direction” and “magnitudes” correlations independently. One observable
 499 proposed by H. Niemi et al. [69] can be used to study the event-by-event fluctuations
 500 and also can measure the correlations between different v_n which directly related to ϵ_n .
 501 They define the linear correlation coefficients $c(a, b)$ as :

$$c(a, b) = \left\langle \frac{(a - \langle a \rangle_{ev})(b - \langle b \rangle_{ev})}{\sigma_a \sigma_b} \right\rangle_{ev} \quad (1.78)$$

502

503 where σ_a is the standard deviation of the quantity a . This correlation function is

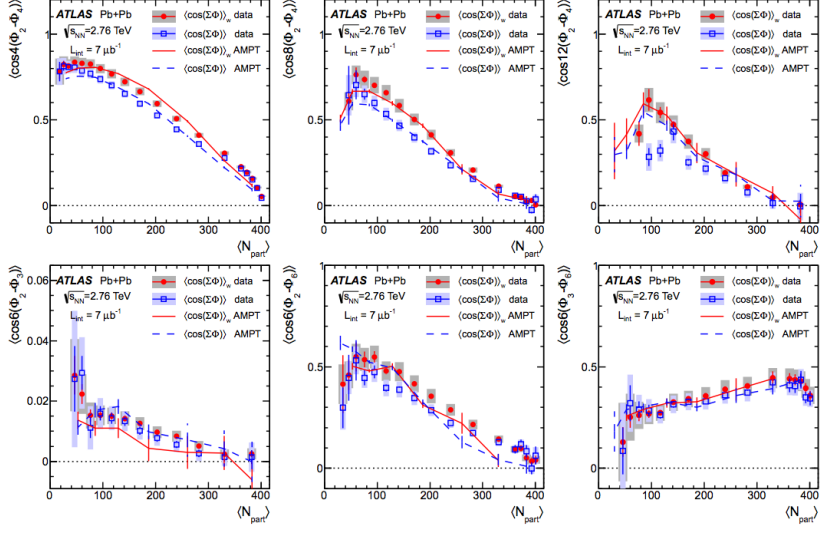


Figure 1.9: The two event plane correlators by using two subevent groups by ATLAS collaboration. $\langle \sum \Phi \rangle \equiv \langle jk(\Phi_n - \Phi_m) \rangle$. Results from the AMPT model calculation via the SP method(solid line) and the EP method(dashed line) for represent for comparison [9].

504 1 (or -1) if a and b are linearly (anti-linearly) correlated and zero in the absence of
 505 correlation. From this calculation with hydrodynamic models, correlation between flow
 506 harmonics was found. The result indicates that the correlation not only depends on
 507 η/s , but is also strongly sensitive to the other properties of the QGP, such as decoupling
 508 temperature. Otherwise, the correlation v_2 and v_3 seems sensitive to the initial conditions
 509 but insensitive to η/s . Also clear p_T dependence on correlation $c(v_2, v_3)$ was expected.

510 Recently we measured for the first time the new multiparticle observables, the Sym-
 511 metric 2-harmonic 4-particle Cumulants (SC), which quantify the relationship between
 512 event-by-event fluctuations of two different flow harmonics [70]. The new observ-
 513 ables are particularly robust against few-particle non-flow correlations and they provide
 514 orthogonal information to recently analysed symmetry plane correlators [71]. It was
 515 demonstrated that they are sensitive to the η/s of the expending medium and simultane-
 516 ous descriptions of different order harmonic correlations would constrain both the initial

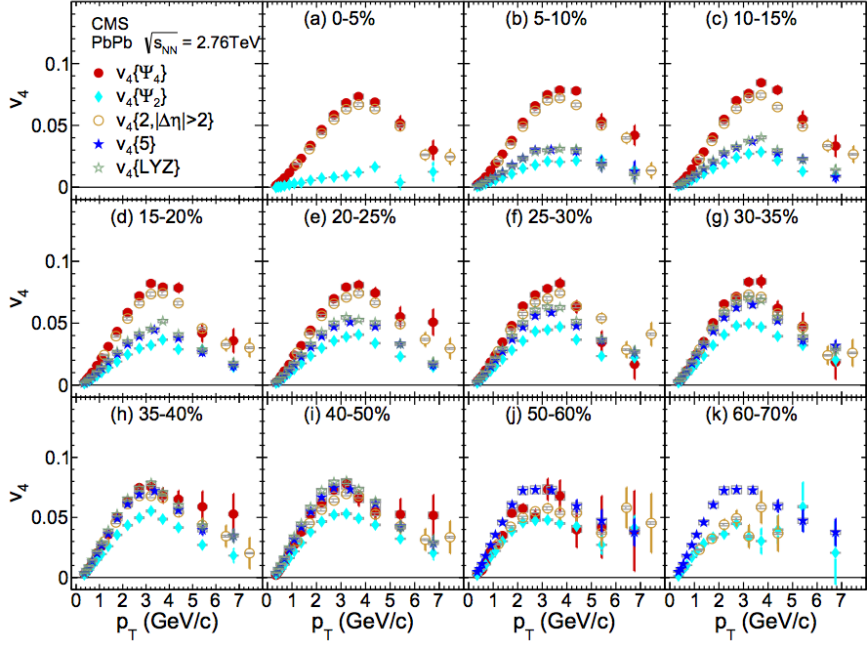


Figure 1.10: Measurement of v_4 with different methods as a function of p_T for the indicated centrality bins. The event plane method with its own event plane(red circle) and the event plane method with 2nd order event plane (blue diamonds) are drawn together.[10]

517 conditions and the medium properties. In this article, we have extended the analysis to
 518 higher order Fourier harmonic (up to 5th order) correlations as well as p_T dependence
 519 of correlations for the lower order harmonic (v_3-v_2 and v_4-v_2). We also include a sys-
 520 tematic comparison to hydrodynamic and AMPT models.

521 From these studies, we can understand that the flow harmonics fluctuate event-by-
 522 event due to the fluctuations in the initial matter distribution, including contributions
 523 from fluctuations in the positions of the participating nucleons in the nuclei, the partic-
 524 ipant plane, determined by the participating nucleons. In addition, such event-by-event
 525 fluctuations of the spatial asymmetry generate additional harmonics, which are more
 526 sensitive to η/s , because the effect of share viscosity reduces all anisotropic flow coeffi-
 527 cients, with a larger decrease for higher order coefficients.

528 **Chapter 2**

529 **Experimental setup**

530 **2.1 Large Hardon Collider**

531 The Large Hadron Collider is the biggest accelerator in the world which was built
532 between 2002 and 2009 at CERN. This powerful particle accelerator was installed in the
533 27km long circular underground tunnel across the border between France and Swiss. It
534 has 16 RF(radio frequency) accelerating cavities and over 1600 superconducting mag-
535 nets. With this accelerator, we can collide protons with a centre-of mass energy up to 14
536 TeV and Pb ions with a centre-of mass energy per nucleon up to 5.5 TeV [72].

537 The protons are first accelerated in linear accelerator LINAC and injected into the
538 BOOSTER at an energy of 50 MeV. The BOOSTER accelerates them to 1.4 GeV before
539 they are sent to the Proton Synchrotron (PS), which further accelerates the protons to
540 25 GeV. From the PS they are sent to the Super Proton Syncrotron (SPS), where they
541 yet again are accelerated, this time to 450 GeV. Finally they are transferred to the LHC
542 ring. At Maximum the 2808 bunches of the protons travel the ring either clockwise or
543 counter-clockwise.

544 Procedures for operating the LHC with lead ions are similar, though with some dif-
545 ferences. The lead ions are produced by heating a highly purified lead sample up to
546 around 550° . This creates a number of charge states, with Pb^{27+} being the dominant
547 one. The ions are accelerated in LINAC 3 to 4.2 MeV per nucleon. Afterwards they are
548 sent through a carbon foil, which strips them to Pb^{54+} . The Pb^{54+} beam is led to the
549 Low Energy Ion Ring (LEIR), where it is accelerated to 72 meV per nucleon, before be-

550 ing transferred to the PS. At the PS, the ions are accelerated up to 5.9 GeV per nucleon.
 551 The ions once again are sent through the foil, stripping them to Pb^{82+} , which is the final
 552 ionization used for collisions. After the PS the now fully stripped ions arrive at the SPS,
 553 where they are accelerated to 177 GeV per nucleon, before being sent into the LHC ring
 554 for acceleration to their collision energy ($0.999999991c$ at $\sqrt{s_{NN}} = 7\text{TeV}$). As in the
 555 proton case, the ion bunches are sent either clockwise or counter-clockwise around the
 556 ring. The collision of lead ions only occur at 3 of the experiment sites, namely ALICE
 557 [73], ATLAS [74], and CMS [75]. The ATLAS and CMS experiments are general pur-
 558 pose detectors used to look for signs of new physics, including the origins of the mass
 559 of elementary particles and extra dimensions. The ALICE detector is designed to study
 560 the properties of the so called quark gluon plasma (QGP) which is believed to have been
 561 created in the first microseconds after the Big Bang. Details will be discussed in the
 562 following chapter.

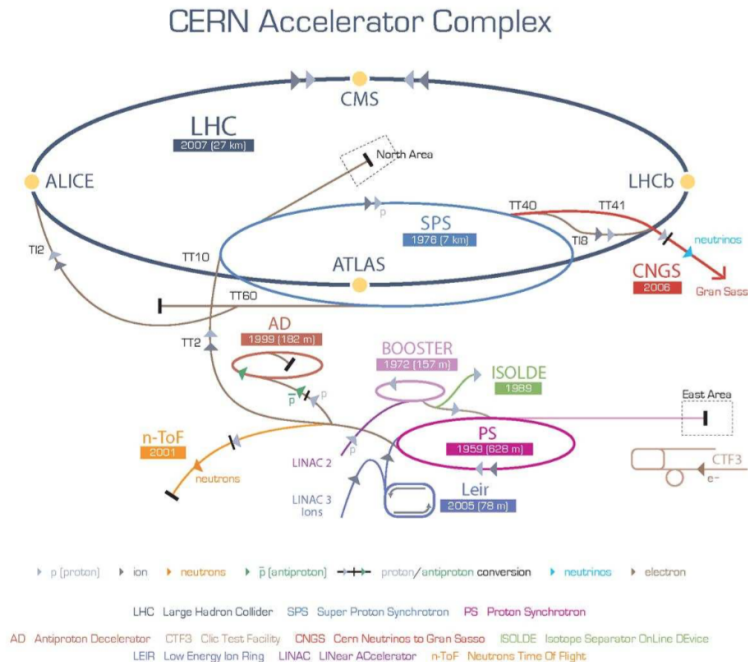


Figure 2.1: Schematic view of Large Hadron Collider

563 2.2 The ALICE experiment

564 ALICE (A Large Ion Collider Experiment) is one of the experiments placed in LHC.
565 The collaboration involves more than a thousand scientists and engineers from 116 insti-
566 tutes and 33 countries. It was designed to study the properties of QCD and to characterize
567 the Quark-Gluon Plasma (QGP). It is the only experiment at LHC which was optimized
568 for the heavy ions collisions.

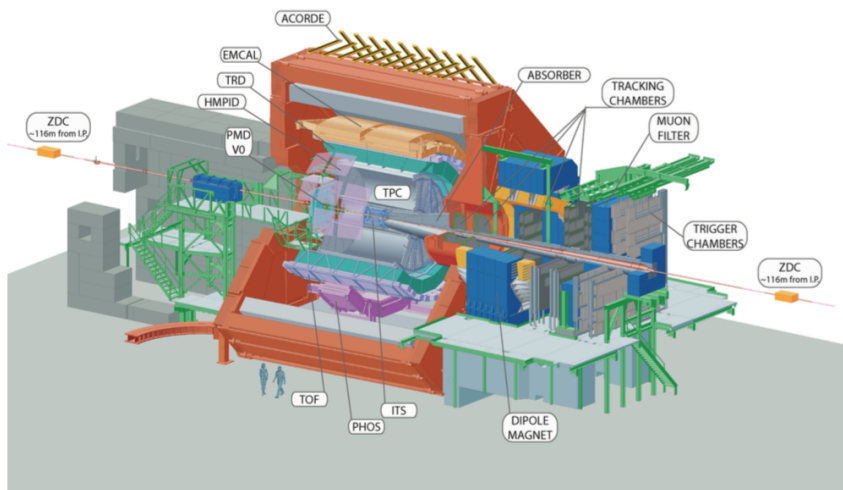


Figure 2.2: Schematic view of ALICE detector [11]

569 The detector is placed in the solenoid magnet from the L3 experiment. This pro-
570 vides a relatively low magnetic field of 0.5 T, which allows to measure low momentum
571 particles corresponding to the so-called soft QCD, as well as more energetic particles
572 from hard processes. Because of the extremely high multiplicity expected in nucleus-
573 nucleus collisions at LHC energies, the design of ALICE was optimized for a multiplic-
574 ity $dN_{ch}/dy = 8000$. ALICE has an efficient and robust tracking system over a large
575 momentum range, from tens of MeV/c (soft physics) to over $100 \text{ GeV}/c$ (jet physics). As
576 some of the tracking detectors are based on drift technologies, they are slower than the
577 detectors operated by the other LHC experiments but can work at the nominal LHC ion
578 beam rate of 10 kHz. A specificity of the ALICE detector over the other LHC experi-

579 ments is its emphasis on hadron and lepton identification (PID). It is achieved over much
580 of the momentum range using most known PID techniques, such as dE/dx energy loss,
581 time-of-flight, transition and Cherenkov radiation, electromagnetic calorimetry, muon
582 filters, and topological decay reconstruction.

583 The detectors in the ALICE experiment are arranged in a classical layered structure
584 around the interaction point as Shown in Figure.2.2. Here is a short description of the
585 main detectors which used in this analysis. Most of description here are taken from the
586 ALICE Technical Design Report (ALICE TDR) [76], and more detail information can
587 be found in CERN document system (CDS) [11].

588 **2.2.1 ITS**

589 The Inner Tracking System (ITS) consists of six layers of silicon detectors with radii
590 few cm as shown Figure.2.5

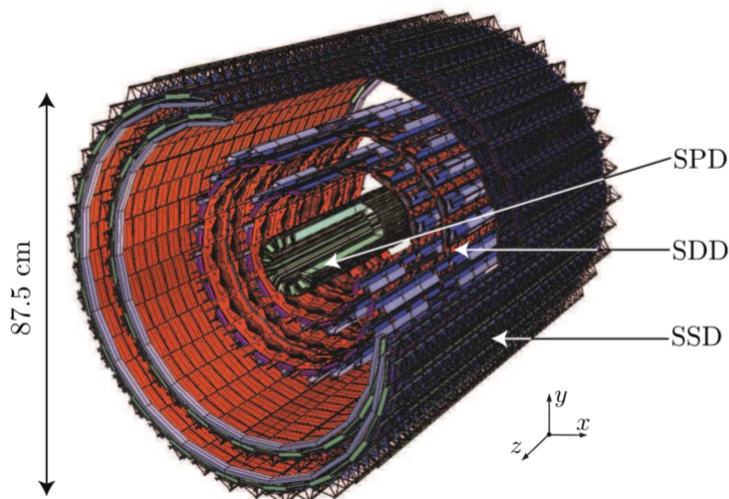


Figure 2.3: ALICE Inner Tracking System(ITS), includes Silicon Pixel Detector(SPD)
and Silicon Drift Detector(SDD) and Silicon Strip Detector(SSD)

591 The main purpose of the ITS is the reconstruction of the primary vertex of the col-
592 lision as well as the reconstruction of secondary vertexes with a resolution better than
593 100 μm in transverse direction. The ITS stand-alone tracking can provide the tracking

594 information for low-momentum particles that do not reach the TPC. The p_T cut-off at
595 nominal field for the two innermost layers is about 35 MeV/c.

596 The two innermost layers, Silicon Pixel Detector (SPD) [77], are based on hybrid
597 silicon pixels which consist of silicon detector diodes with a thickness of 200 μm . The
598 first layer and the second layer are placed at 3.9 cm and 7.6 cm with an acceptance of
599 $|\eta| < 2.0$ and $|\eta| < 1.4$, respectively. The SPD has approximately 10 million channels.
600 The pixel readout chip (ALICE1LHCb) is a mixed- signal ASIC for the readout of 8192
601 pixels. Each pixel cell contains a preamplifier-shaper with leakage current compensa-
602 tion, followed by a discriminator. A signal above threshold results in a logical 1 which
603 is propagated through a delay line during the 6 μs latency time until the arrival of the L1
604 trigger signal. Upon arrival of the L1 trigger, the logical level present at the end of the
605 delay line is stored in the first available buffer location. The outputs of the discriminators
606 in the pixel cells of the ALICE1LHCb chip provide a fast-OR digital pulse when one or
607 more pixels are hit on the chip.

608 The third and forth layer, Silicon Drift Detector (SDD) [78], consist of a 300 μm
609 thick layer of homogeneous high-resistivity silicon. The readout of the SDD is analog,
610 therefore particle identification can be conducted using the information of energy-loss.
611 The SDD has 133,000 channels.

612 The two outermost layers, Silicon Strip Detector (SSD) [79], consist of sensors
613 equipped on both sides with silicon micro-strips. These are arranged under a stereo angle
614 of 35 mrad allowing for a two-dimensional measurement of the track position together
615 with an energy-loss measurement for particle identification. The SSD has approximately
616 2.6 million channels [80].

617 2.2.2 TPC

618 The Time Projection Chamber (TPC) [81] is the main tracking device of the ALICE
619 experiment. It is a large cylindrical gas chamber detector with $\sim 88\text{m}^3$ volume in 0.5
620 T solenoidal magnetic filed parallel to the E field.

621 This detector is designed to have dE/dx resolution better than 5% and a relative
622 p_T resolution better than 1% for momenta of $\sim 1\text{GeV}/c$ and better than 2.5% for mo-

623 ments of $4\text{GeV}/c$, and two track resolution capable of separating tracks with a relative
624 momentum difference of $< 5\text{MeV}$.

625 The TPC is separated by two volumes with the Central Electrode (CE) made of single
626 stretched Mylar foil, and secondary electrons drift toward the end-caps.

627 Volumes are filed with Ne-CO₂-N₂ (90%-10%-5%) gas which is optimized for drift
628 speed, ion mobility, and low diffusion of electrons. Since, Ne-CO₂-N₂ gas have de-
629 pendence of drift velocity on temperature, TPC is aiming for a thermal stability with
630 $\Delta T < 0.1\text{K}$ in the drift volume over the running period.

631 As the gas detector, the TPC field cage has to be operated at very high voltage gra-
632 dients, of about 400V/cm, with a high voltage of 100kV at the central electrode which
633 results in a maximum drift time of about $90\mu\text{s}$.

634 The TPC covers a pseudo-rapidity range of $|\eta| < 0.9$ for full track length within
635 the TPC volume. Also it provides 0 to 2π azimuthal coverage except for the dead zones
636 in the TPC, and it makes the TPC an ideal detector for anisotropic flow analysis, since
637 these inefficiencies in the azimuthal acceptance would result in non-negligible system-
638 atic biases for the azimuthal angle correlations analysis.

639 2.2.3 VZERO

640 The VZERO detectors(also often called V0) [82] are designed with a much larger
641 acceptance, in order to perform as a minimum bias trigger in both proton-proton and
642 Pb-Pb collisions. Furthermore, it is also used, together with the timing information of
643 the collision, for the rejection of beam-gas interactions. The VZERO is also used to
644 determine the event centrality and many of ALICE analyses use centrality determination
645 from VZERO.

646 This consists of two separate arrays of scintillator counters and V0A and V0C,
647 placed on different sides of the central barrel detectors along the beam line. V0A/C
648 are placed asymmetrically with respect to the interaction point. V0A is located 340 cm
649 from the interaction point on the side opposite to the muon arm, while V0C is placed 90
650 cm from the interaction point on the opposite side from V0A. Because of this asymmetry,
651 V0A and V0C have different pseudo-rapidity coverage. The V0A covers pseudo-rapidity

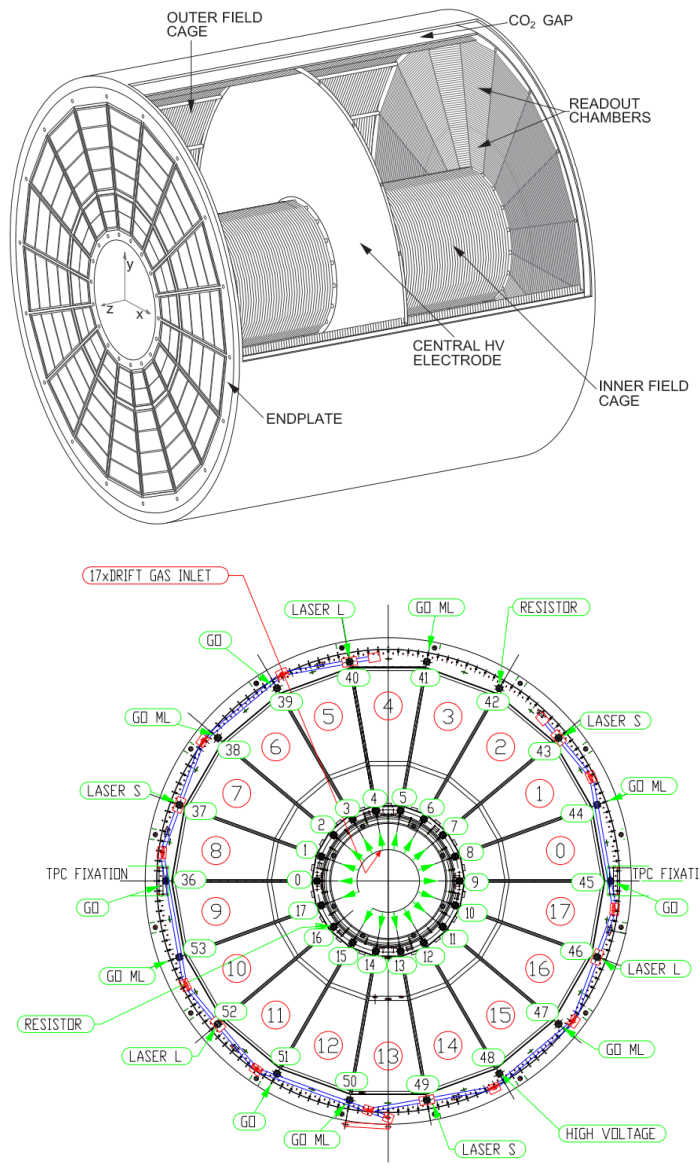


Figure 2.4: ALICE Time Projection Chamber

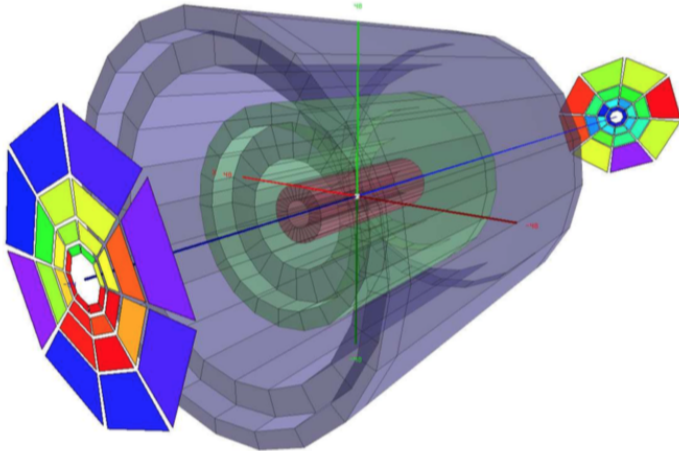


Figure 2.5: ALICE VZERO detectors on both side of TPC

652 range $2.8 < \eta < 5.1$, while V0C covers $-3.7 < \eta < -1.7$.

653 The V0A/V0C are segmented into 32 elementary counters distributed in four rings.
 654 Each ring covers 0.4-0.6 unit of pseudo-rapidity. The rings are divided into eight sectors
 655 of 45° . The elementary counter consists of scintillator material with embedded Wave-
 656 Length Shifting (WLS) fibers. The light from the WLS is collected by clear fibers and
 657 transported to PhotoMultiplier (PM) installed at 3-5 m from the detectors, inside the L3
 658 magnet. The time resolution of each individual counter will be better than 1 ns.

659 Signals from each PMT are sent to an electronics circuit, which delivers two signals.
 660 The first one is sent to a threshold discriminator for the generation of the V0 event
 661 triggers. It is amplified by a factor of about 10. If at least one discriminator is fired
 662 during the time window around the timing of the beam crossing (after 3 ns for V0A, 11
 663 ns for V0C), the V0 event trigger is issued.

664 **2.2.4 Other detectors**

665 **TRD**

666 Transition Radiation Detector (TRD) [83] is placed from 2.9 to 3.8 m from the in-
667 teraction point. It discriminates electrons from pions with high efficiency for momenta
668 about 1 GeV/c by the identification of the transition radiation photons from electrons.
669 Also this detector can provide the trigger signals for electron

670 **TOF**

671 Time Of Flight (TOF) [84] is made of Multigap Resistive Plate Chamber strips
672 (MRPC), which are made by a ten layer double-stack detector with a time resolution
673 of about 40 ps. By measuring the time particles take to reach it, and combined with
674 the tracking information of the TPC, it allows for the identification of pions, kaons and
675 protons

676 **HMPID**

677 High Momentum Particle Identification Detector (HMPID) [85] consists of an array
678 of proximity-focusing Ring Imaging CHerenkov counters (RICH) and covers a pseudo-
679 rapidity range of $|\eta| < 0.6$ and 58° of azimuthal angle. The HMPID discriminates
680 pions and kaons in the range $1 < p_T < 3\text{GeV}/c$ and protons and kaons in the range
681 $2 < p_T < 5\text{GeV}/c$ by means of their Cherenkov rings.

682 **PHOS**

683 PHOton Spectrometer (PHOS) [86] is placed partially opposite to the EMCAL and
684 made of highly segmented electromagnetic calorimeter of lead-tungstenate (PbWO₄ ,
685 PbWO) crystals with a radiation length of $20X_0$. It is used for neutral mesons and direct
686 photon measurements.

687 **EMCAL**

688 ElectroMagnetic Calorimeter (EMCAL) [87] is a lead scintillator sampling calorime-
689 ter that covers an azimuthal angle range of 107° in the rapidity interval $|\eta| < 0.7$ at a

690 radial distance of about 4.5 m from the vacuum tube. The EMCAL is designed for the
691 study of jet-physics and can provide trigger signals for hard jets, photons and electrons.

692 **Muon Spectrometer**

693 Muon Sepctrometer is situated in the forward($-4 < \eta < -2.5$) region on one side
694 of the experiment. It track muons with momentum $p > 4\text{GeV}/c$. And used for the
695 analaysis of quarkonia decaying to the $\mu\mu$.

696 **TZERO**

697 TZERO (T0) [88] detector is designed to determine the collision time. T0 consists of
698 two units, one on each side of the interaction point. Each T0 unit is comprised of quartz
699 Cherenkov radiators glued to photo multiplier tubes. A coincidence between signals in
700 both sides is used for both vertex and time determination

701 **Zero Degree Calorimeter**

702 The Zero Degree Calorimeters (ZDC) [89] are positioned at extremely forward an-
703 gles. Their role is to measure the spectator nucleons from heavy ion collisions, in order
704 to estimate the number of participants, and hence the centrality. Furthermore they are
705 also used to determine the event plane.

706 **2.2.5 Analysis Framework**

707 The ROOT system is an object-oriented framework (written in C++) developed at
708 CERN in the 90's and used by various collaborations worldwide as a starting framework
709 on top of which the specific framework needed for particular collaboration is being built.
710 It provides a full set of features needed for event generation, detector simulation, event
711 reconstruction, data acquisition and data analysis. All features are encoded in a set
712 of about 650 classes grouped in about 40 libraries. A vast majority of ROOT classes
713 inherit from the common base class called TObject, which provides default behavior and
714 protocol (e.g. protocol for the object I/O, error handling, sorting, inspection, printing,
715 drawing, etc.) for all objects in the ROOT system, but the standalone classes which can
716 be used as built-in types are also implemented.

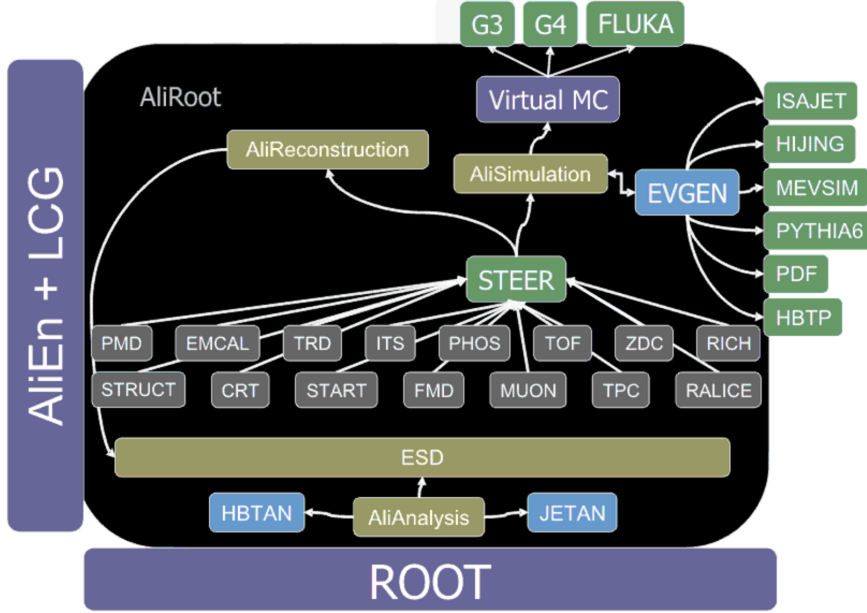


Figure 2.6: Picture of general schema of the AliRoot architecture [12]

717 The AliRoot is the specific version of framework which built on the ROOT system.
 718 It's optimized for ALICE simulation, alignment, calibration, reconstruction, visualization,
 719 quality assurance, and analysis. Most of codes are written in C++ and some parts
 720 are written in Fortran.

721 Also for the large consumption of CPU power, the ALICE analysis framework pro-
 722 vides several distributed computing systems, including the parallel computing (PROOF)
 723 or, Grid. Because of the huge amount of data produced by the ALICE detector ($\sim 2\text{PB}$
 724 per year) [90], the reconstructed events are saved into a worldwide computing center.
 725 The computing center has a distributed hierarchy with Tier 0 to Tier 3, and the ALICE
 726 Virtual Organization (ALICE VO) is made of more than 80 sites. Each site provides
 727 large computing power with physical machines where the software programs can be run.
 728 By using JDL(Job Description Language) and XML(eXecutable Machine Language),
 729 users can use codes with AliRoot over 1500 CPUs at the same time.

730 **Chapter 3**

731 **Data analysis**

732 **3.1 Data selection**

733 In this chapter, we outline the selection criteria applied for this analysis. Basically,
734 we used LHC10 data with pass 2 reconstruction which marked as “good run”. The period
735 of data taking is LHC10h and it is only data sets from heavy ion collisions from 2010.

736 **3.1.1 Default cuts and settings**

737 The data sample recorded by ALICE during the 2010 heavy-ion run at the LHC
738 is used for this analysis. Detailed procedure of the ALICE data taking can be found
739 in [91, 92, 93]. The Time Projection Chamber (TPC) was used to reconstruct charged
740 particle tracks and measure their momenta with full azimuthal coverage in the pseudo-
741 rapidity range $|\eta| < 0.8$. Two scintillator arrays (V0) which cover the pseudo-rapidity
742 ranges $-3.7 < \eta < -1.7$ and $2.8 < \eta < 5.1$ were used for triggering, and the de-
743 termination of centrality [94]. The trigger conditions and the event selection criteria
744 are identical to those described in [7, 94]. Approximately 10^7 minimum-bias Pb-Pb
745 events with a reconstructed primary vertex within ± 10 cm from the nominal interaction
746 point in the beam direction are used for this analysis. Charged particles reconstructed
747 in the TPC in $|\eta| < 0.8$ and $0.2 < p_T < 5$ GeV/c were selected. The charged track
748 quality cuts described in [7] were applied to minimize contamination from secondary
749 charged particles and fake tracks. The charged particle track reconstruction efficiency
750 and contamination were estimated from HIJING Monte Carlo simulations [95] com-

751 bined with a GEANT3 [96] detector model, and found to be independent of the collision
 752 centrality. The reconstruction efficiency increases from 70% to 80% for particles with
 753 $0.2 < p_T < 1 \text{ GeV}/c$ and remains constant at $80 \pm 5\%$ for $p_T > 1 \text{ GeV}/c$. The estimated
 754 contamination by secondary charged particles from weak decays and photon conver-
 755 sions is less than 6% at $p_T = 0.2 \text{ GeV}/c$ and falls below 1% for $p_T > 1 \text{ GeV}/c$. With
 756 this choice of low p_T cut-off ($p_T > 0.2 \text{ GeV}/c$) we are reducing event-by-event biases
 757 from smaller reconstruction efficiency at lower p_T , while the high p_T cut-off ($p_T < 5.0$
 758 GeV/c) was introduced to reduce the contribution to the anisotropies from jet particles.

759 The default estimator for centrality determination in ALICE is obtained from the
 760 measurement multiplicity in the VZERO detectors.

Centrality(%)	0-5	5-10	10-20	20-30	30-40	40-50	50-60	60-70
b(fm) AMPT	0.00-3.72	3.72-5.23	5.23-7.31	7.31-8.88	8.88-10.20	10.20-11.38	11.38-12.47	12.47-13.50
b(fm) HIJING	0.00-3.60	3.60-5.09	5.09-7.20	7.20-8.83	8.83-10.20	10.20-11.40	11.40-12.49	12.49-13.49
b(fm) ALICE	0.00-3.50	3.50-4.94	4.94-6.98	6.98-	-9.88	9.81-	-12.09	12.09-

<https://twiki.cern.ch/twiki/bin/viewauth/ALICE/CentStudies>

761
 762
 763 Also, even though the Inner tracking System (ITS) and the Time Projection Chan-
 764 mber (TPC) were used as the main tracking devices for ALICE experiment, ITS does
 765 not have uniform acceptance. On the other hand, corrections for TPC are negligible due
 766 to its uniform acceptance. Because of this, we are going to use TPC only cuts in this
 767 analysis, in which the tracks are required to have at least 70 reconstructed space point
 768 out of the maximum 159 in the TPC and a $\langle \chi^2 \rangle$ per TPC cluster ≤ 4 (with 2 degrees of
 769 freedom per cluster)

770 Only tracks with a transverse distance of closest approach (DCA) to the primary ver-
 771 tex less than 3 mm , both in longitudinal and transverse direction, are accepted to reduce
 772 the contamination from secondary tracks (for instance the charged particles produced in
 773 the detector material, particles from weak decays, etc.). Tracks with kinks (the tracks
 774 that appear to change direction due to multiple scattering, K^\pm decays) were rejected.

775 **3.1.2 Data QA**

776 **η distribution QA**

777 In principle, the multiplicity in each η region should be similar (i.e. $N_{A\text{side}} \sim$
 778 $N_{C\text{side}}$). To confirm this similarity of multiplicity in each η set, we check η distribution
 779 for each centrality bins. Also the multiplicity in $\eta < 0$ region and $\eta > 0$ is compared as
 780 ratio. The ratio between number of multiplicity in $\eta > 0$ subgroup and $\eta < 0$ subgroups,
 781 was fitted with 0th order polynomial function with unity parameter(i.e $y = 1$) run by run.
 782 After fitting, χ^2/NDF was calculated to check for the same multiplicity in both sub-
 783 set groups for each run, each centralities. Fig.3.1 are the η distribution for run number
 784 137135 and the χ^2/NDF test results over all run. The Run number corresponding Run
 785 ID information can be found in Appendix ??

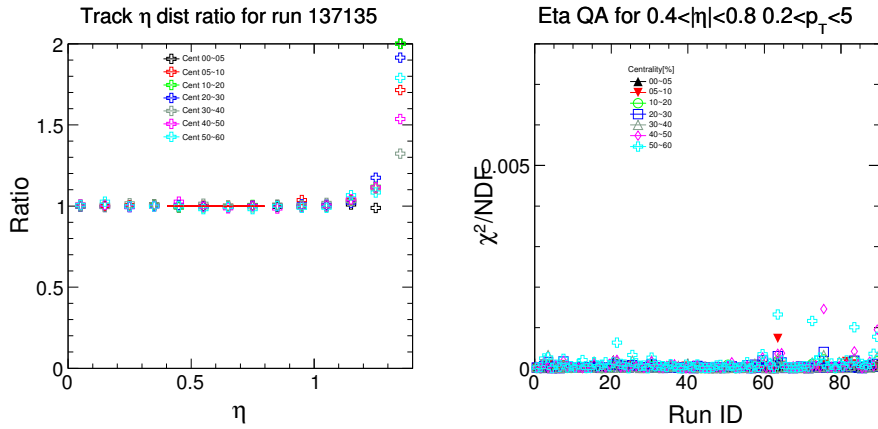


Figure 3.1: Ratio of $dN/d\eta$ for flip over +/- η region(left) and χ^2/NDF for ϕ flatness as function of RunID

786 QA result looks quite good across the runs as shown in figure. χ^2/NDF was lower
 787 than 0.002 for all runs and all centralities. As the results, we might simply assume that
 788 number of multiplicity in each subgroups are same.

789 **ϕ distribution QA**

790 ϕ flatness QA was performed on the ϕ distributions with the data. We fit the distri-
 791 butions with 0th-order polynomial. The distribution was fitted run by run. χ^2/NDF of
 792 each run were taken to estimate the flatness of distribution as like η QA method. The fit
 793 results are shown in Fig.3.2

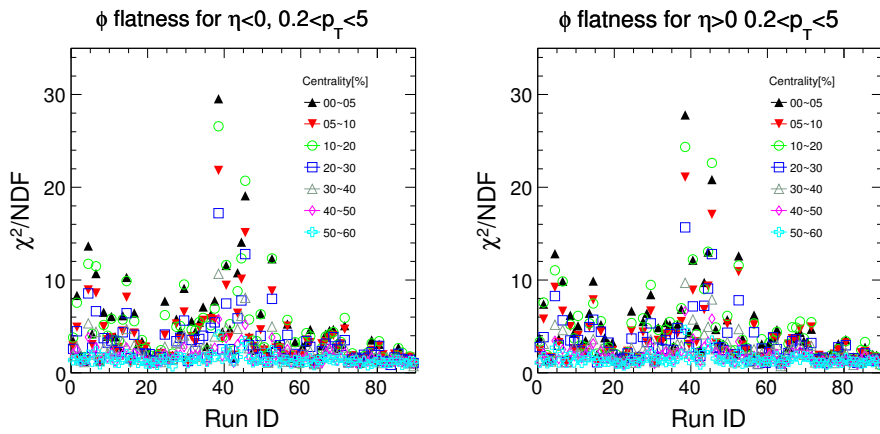


Figure 3.2: χ^2/NDF for ϕ flatness for $\eta < 0$ (left) and $\eta > 0$ (right)

794 As shown in the figure, the flatness (χ^2/NDF of ϕ) of some runs is worse than
 795 others. This is considered as a detector effect, and might be affect on our analysis.
 796 The effect of these non-uniform ϕ distribution will be treated as systematics and will be
 797 covered in systematic chapter.

798 **3.2 Analysis strategy**

799 While from existing measurements an estimate can be placed on the average value
800 of QGP’s η/s , both at RHIC and LHC energies, what remains completely unknown is
801 how the η/s of QGP depends on temperature (T). This study has been just initiated
802 by the theorists in Ref. [13], where the first (and only rather qualitative) possibilities
803 were investigated (see Fig. 1 therein). The emerging consensus of late is that it is
804 unlikely that the study of individual flow harmonics v_n will reveal the details of $\eta/s(T)$
805 dependence. In fact, it was demonstrated already in the initial study [13] that different
806 $\eta/s(T)$ parameterizations can lead to the same centrality dependence of individual flow
807 harmonics. In Ref. [97] new flow observables were introduced by the theorists, which
808 quantify the degree of correlation between two different harmonics v_m and v_n . The
809 initial success of these new observables was attributed to their potential to discriminate
810 for the first time the two respective contributions to anisotropic flow development—from
811 initial conditions and from the transport properties of the QGP [97]. Therefore their
812 measurement in turn would enable the experimental verification of theoretical predictions
813 for individual stages of heavy-ion evolution independently. Besides this advantage, it
814 turned out that correlations of different flow harmonics are sensitive to the details of
815 $\eta/s(T)$ dependence [71], to which individual flow harmonics are nearly insensitive [13].

816 For technical reasons, discussed in detail in Refs. [71, 98], the correlations between
817 different flow harmonics cannot be studied experimentally with the same set of observ-
818 ables introduced by the theorists in Ref. [97]. Instead, in [98] the new flow observables
819 obtained from multiparticle correlations, so-called *Symmetric Cumulants* (*SC*), were in-
820 troduced to quantify in the most reliable way (i.e. nearly insensitivity to nonflow) the
821 correlation of amplitudes of two different flow harmonics. The technical details are
822 elaborated in Ref. [98], while the first measurements of *SC* observables were recently
823 released by ALICE Collaboration in Ref. [71]. For the convention, we will denote *Sym-*
824 *metric Cumulants* for m th order and n th order as $SC(m, n)$ from now on. This new
825 observable are based on 4-particle cumulant, and defined as

$$SC(m, n) = \langle\langle \cos(m\varphi_1 + n\varphi_2 - m\varphi_3 - n\varphi_4) \rangle\rangle \quad (3.1)$$

$$= \langle v_n^2 v_m^2 \rangle - \langle v_n^2 \rangle \langle v_m^2 \rangle \quad (3.2)$$

826 where double angular brackets indicates that the averaging has been extended from single to all events. Due to the condition that $m \neq n$, a lot of terms which appear in
827 the general cumulant expansion are non-isotropic and therefore, average to zero for a
828 detector with uniform acceptance when the averaging is extended to all events.
829

830 These values can be obtained by multi-particle correlation with q-Cumulants such as

$$\langle\langle 2 \rangle\rangle \equiv \langle\langle e^{in(\phi_1-\phi_2)} \rangle\rangle \equiv \frac{\sum_{i=1}^N (W_{\langle 2 \rangle})_i \langle 2 \rangle_2}{\sum_{i=1}^N (W_{\langle 2 \rangle})_i} \quad (3.3)$$

$$\langle\langle 4 \rangle\rangle \equiv \langle\langle e^{in(\phi_1+\phi_2-\phi_3-\phi_4)} \rangle\rangle \equiv \frac{\sum_{i=1}^N (W_{\langle 4 \rangle})_i \langle 4 \rangle_i}{\sum_{i=1}^N (W_{\langle 4 \rangle})_i} \quad (3.4)$$

831
832
833 The choice for the event weights in above equations is not arbitrary and we will
834 outline in Appendix D. It has a physical meaning which will render the number of com-
835 binations (i.e. number of distinct 2- and 4-particle combinations one can form for an
836 event with multiplicity M) as the only correct event weight.

837 For fixed value of v_n and v_m over all events, the $SC(m, n)$ which defined as like
838 Eq.3.2, is zero by definition. Moreover we can obtain the result in the last line of above
839 equation not only when v_m and v_n are fixed for all events, but also when event-by-event
840 fluctuations of v_m and v_n are correlated(or anti-correlated).

841 This $SC(m, n)$ is very efficient observables for measuring flow “magnitude” corre-
842 lation because it’s free from event-plane which is directly related to “direction” corre-
843 lation. (Any dependence on the event plane ψ_n and ψ_m is canceled by definition)

844 As a result, the Eq.3.2 holds, the correlation between flow harmonics, and we can
845 concluded whether finding v_m larger than $\langle v_m \rangle$ in an event will enhance(or reduce) the
846 probability of finding v_n larger than $\langle v_n \rangle$ in that event.

847 In this analysis, we are going to show $SC(m, n)$ results which can be calculated for
 848 correlation between flow harmonics by using 4- particle cumulants. In addition, we will
 849 show not only $SC(m, n)$ but also going to show *normalized* $SC(m, n)$ (also denote as
 850 $NSC(m, n)$)

$$NSC(m, n) = \frac{SC(m, n)}{\langle v_n^2 \rangle \langle v_m^2 \rangle} \quad (3.5)$$

851
 852 *Normalized symmetric cumulants* (NSC) reflect only the degree of the correlation
 853 which is expected to be insensitive to the magnitudes of v_m and v_n , while $SC(m, n)$
 854 contains both the degree of the correlation and individual v_n harmonics. In Eq.3.5 the
 855 products in the denominator are obtained with two-particle correlations and using a pse-
 856 dorapidity gap of $|\Delta\eta| > 1.0$ to suppress biases from few-particle nonflow correlations.
 857 On the other hand, in the two two-particle correlations which appear in the definition of
 858 $SC(m, n)$ the psedorapidity gap is not needed, since nonflow is suppressed by construc-
 859 tion in SC observable, as the study based on HIJING model has clearly demonstrated in
 860 Ref. [71].

861 However, note that the following Eq.3.6 and 3.7 are not held in this analysis because
 862 of the difference between products $\langle v_m^2 \rangle \langle v_n^2 \rangle$ for denominator and numerator. For the
 863 numerator, since nonflow is suppressed by construction in $SC(m, n)$ we do not apply
 864 any pseudorapidity(η) gap for calculate 4- particle cumulants for all the particles in $|\eta| <$
 865 0.8. But for the denominator, these products were obtained in ALICE with 2- particle
 866 correlations separately with using a pseudorapidity gap of $|\Delta\eta| > 1.0$ to suppress biases
 867 from few particle non-flow correlations. However, other theoretical studies [14] use both
 868 Eq.3.5 and 3.7 for the $NSC(m, n)$

$$\begin{aligned} NSC(m, n) &= \frac{SC(m, n)}{\langle v_n^2 \rangle \langle v_m^2 \rangle} \\ &= \frac{\langle v_n^2 v_m^2 \rangle - \langle v_n^2 \rangle \langle v_m^2 \rangle}{\langle v_n^2 \rangle \langle v_m^2 \rangle} \end{aligned} \quad (3.6)$$

$$= \frac{\langle v_n^2 v_m^2 \rangle}{\langle v_n^2 \rangle \langle v_m^2 \rangle} - 1 \quad (3.7)$$

869 The $SC(m, n)$ provide orthogonal information to recently measured symmetry plane
870 correlators in Refs. [58, 99, 9]. This statement does not exclude the possibility that
871 both set of observables can be sensitive to the same physical mechanisms. In the recent
872 theoretical study [14] it was pointed out that the mechanism giving rise to symmetry
873 plane correlations (nonlinear coupling) can also contribute to symmetric cumulants. As
874 a concrete example it was discussed that the existing correlation due to hydrodynamic
875 evolution between V_4 and V_2^2 (which are vectors in the transverse plane) implies that
876 both the angles and the magnitudes are correlated [14].

877 Interpretation of flow results obtained with multiparticle correlation techniques in
878 small colliding systems, like pp and p–Pb at LHC, remains a challenge. The underlying
879 difficulty stems from the fact that when anisotropic flow harmonic v_n is estimated with
880 k -particle correlator, the statistical spread of that estimate scales to leading order as
881 $\sigma_{v_n} \sim \frac{1}{\sqrt{N}} \frac{1}{M^{k/2}} \frac{1}{v_n^{k-1}}$, where M is the number of particles in an event (multiplicity) and
882 N is total number of events. This generic scaling ensures that multiparticle correlations
883 are precision method only in heavy-ion collisions, characterized both with large values
884 of multiplicity and flow. To leading order the measurements in small systems [100,
885 101, 102, 103, 104] and the measurements in heavy-ion collisions resemble the same
886 features, which can be attributed to collective anisotropic flow in both cases. However,
887 such interpretation is challenged by the outcome of recent Monte Carlo study [105] for
888 e^+e^- systems in which collective effects are not expected. Nonetheless, in this study
889 to leading order multiparticle correlations exhibit yet again the similar universal trends
890 first seen in heavy-ion collisions, both for elliptic and triangular flow. Therefore, it seems
891 unlikely that the analysis of individual flow harmonics with multiparticle techniques will
892 answer whether collective effects can develop and QGP be formed in small systems—
893 instead new observables, like SC, might provide the final answer due to their better
894 sensitivity [97, 71].

895 **Measuring $SC(m, n)$ with Scalar Product method**

896 In this analysis, we are going to show that $SC(m, n)$ also can be calculated by
897 the Scalar Product(SP) method via measuring moments [106] with single η gap. By

898 introducing single η gap between two different sub-event group can avoid auto (self)-
 899 correlation and can suppress non-flow effects. To calculate $SC(m,n)$ with the SP method,
 900 we need to define the (normalized) flow Q -vector such as

$$Q_n = \frac{1}{N} \sum e^{in\varphi} \quad (3.8)$$

901 Then, the flow magnitude can be easily obtained with Q -vector calculation.

$$\langle v_n^{2k} \rangle = \langle V_n^{k*} V_n^k \rangle = \langle Q_{nA}^{*k} Q_{nB}^k \rangle \quad (3.9)$$

902 To avoid self-correlation when calculating v_n^2 , we divide particles into 2 sub event
 903 groups and introduced single η gap between sub event group to suppress non-flow effect.
 904 So main difference between original method and this method is that calculate correlation
 905 with full-particle Q -vector or divided-particle Q -vector, and existence of η gap around
 906 0.

$$\langle v_m^2 v_n^2 \rangle - \langle v_m^2 \rangle \langle v_n^2 \rangle = \langle V_n V_n^* V_m V_m^* \rangle - \langle V_n^k V_n^* \rangle \langle V_m^k V_m^* \rangle \quad (3.10)$$

$$= \langle Re(Q_{An} Q_{Bn}^* Q_{Am} Q_{Bm}^*) \rangle - \langle Re(Q_{An} Q_{Bn}^*) \rangle \langle Re(Q_{Am} Q_{Bm}^*) \rangle \quad (3.11)$$

907 In this analysis, we take denotation “A” for sub-event group which have negative η
 908 range ($-0.4 > \eta > -0.8$) and “B” for positive η range ($0.4 < \eta < 0.8$). Because we
 909 divided into 2 sub groups, particles will not count twice when calculating $Q_{An} Q_{Bn}^*$, but
 910 there are still possible of auto (self) correlation when calculating “ $Q_{An} Q_{Bn}^* Q_{Am} Q_{Bm}^*$ ”,
 911 this effect is probably small but can be corrected with the analytical method.

$$v_n^{2k} v_m^{2l} = \langle Q_{nA}^{*k} Q_{nB}^k Q_{mA}^{*l} Q_{mB}^l \rangle \quad (3.12)$$

912 The auto correlation during above the equation happens because there is a η gap
 913 between $Q_{nA}^{*k} Q_{nB}^k$, and $Q_{mA}^{*l} Q_{mB}^l$ but not between $Q_{nA}^{*k} Q_{mA}^{*k}$ nor $Q_{nB}^k Q_{mB}^l$, the auto
 914 (self) correlation effect can be corrected by changing equation of $SC(m,n)$ from

$$\langle Re(Q_{An}Q_{Bn}^*Q_{Am}Q_{Bm}^*) \rangle - \langle Re(Q_{An}Q_{Bn}^*) \rangle \langle Re(Q_{Am}Q_{Bm}^*) \rangle \quad (3.13)$$

915 to

$$\begin{aligned} & \langle Re(Q_{An}Q_{Bn}^*Q_{Am}Q_{Bm}^*) - \frac{1}{M_B} Re(Q_{Bm+n}^*Q_{Am}Q_{An}) \\ & - \frac{1}{M_A} Re(Q_{Am+n}Q_{Bn}^*Q_{Bm}^*) + \frac{1}{M_AM_B} Re(Q_{Am+n}Q_{Bm+n}^*)) \rangle \\ & - \langle Re(Q_{An}Q_{Bn}^*) \rangle \langle Re(Q_{Am}Q_{Bm}^*) \rangle \end{aligned} \quad (3.14)$$

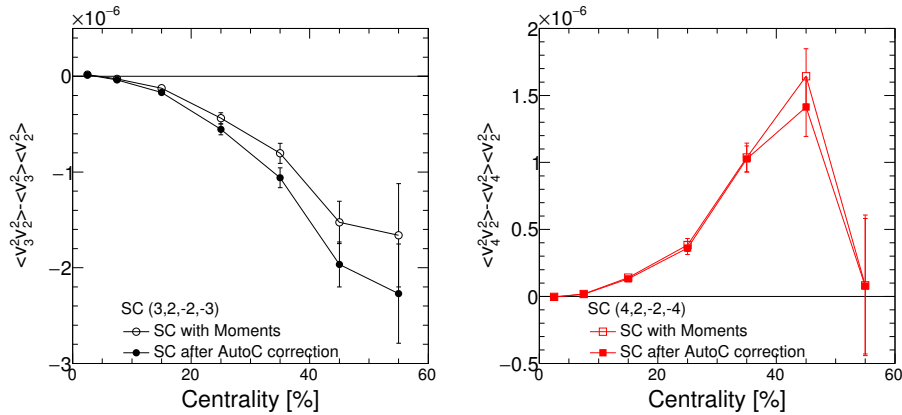


Figure 3.3: Results of $SC(3, 2)$ (left) and $SC(4, 2)$ before auto (self)-correlation correction(open makers) and after correction(closed markers)

916 The detailed results of $SC(m, n)$ and $NSC(m, n)$ with various flow harmonics,
917 and comparison with hydrodynamic calculations and MC simulations, and also the p_T
918 dependence of $SC(m, n)$ and $NSC(m, n)$ and the difference between two different
919 measuring method (QC vs SP) will be covered in the results chapter.

920 **3.3 Systematics**

921 In this section, the systematic uncertainties of $SC(m, n)$ and $NSC(m, n)$ will be
922 presented. The systematic uncertainties were estimated by varying the event and track
923 selection criteria. All systematic checks described here are performed independently.
924 Each results of $SC(m, n)$ (and also $NSC(m, n)$) with a selected criterion are compared
925 to ones from the default event and track selection described in the previous chapter.
926 The differences between the default results and the ones obtained from the variation
927 of the selection criteria are taken as systematic uncertainty of each individual source.
928 The different ratio were fitted with a 0-th order polynomial as function of centrality
929 to suppress point-to-point statistical fluctuations and to extract the overall systematics.
930 The contributions from different sources were then merged in quadrature to obtain the
931 final value of the systematic uncertainty. The detailed conditions varying for systematics
932 studies were described in the following.

933 **3.3.1 Systematics from Non uniform phi distribution**

934 This section is about systematics uncertainty from the non-uniform efficiency of de-
935 tector performance. In principle, the ϕ distribution of produced particle should be flat
936 over all events unless detector effect. But in our data, as seen in the previous section in
937 data QA (see figure.3.2), the distribution of the transverse angle of particle produced is
938 not perfectly uniform due to detector effects like inefficiency or dead-zone area. And
939 these non-uniform ϕ distributions vary run-by-run, and it is not easily corrected by sim-
940 ple weight correction for specific ϕ angle.

941 This non-uniform ϕ distribution might change the final results of $SC(m, n)$ and
942 should be taken into systematic uncertainty. The simplest and basic approach to check
943 the effect of non-uniform distribution is categorize run groups into two sub groups to
944 have good ϕ distribution, and for the other group to have bad ϕ distribution. Then
945 measure the $SC(m, n)$ values with each sub groups independently and calculated the
946 difference between them as the systematic uncertainty. However, to use this methods,
947 we need to have almost same number of events for each groups. Even though we have
948 similar number of events for each groups, we are going to have larger statistical error

949 because of half of events in this way.

950 In this analysis, to check systematic uncertainties from non-uniform ϕ distribution,
951 we use AMPT simulation which has better match to data than any other existing models.
952 We measure $SC(m, n)$ with the large statistics AMPT dataset which has flat ϕ distribu-
953 tion, and impose non-uniform ϕ distribution from data and calculate the difference be-
954 tween original AMPT and modified AMPT as systematic uncertainty from non-uniform
955 ϕ distribution.

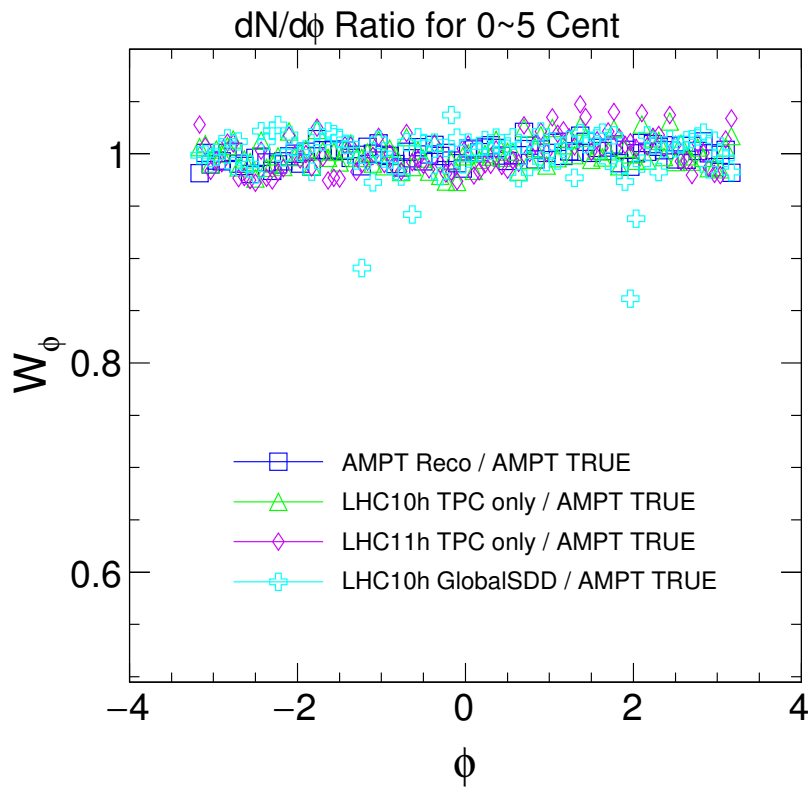


Figure 3.4: Scaled ratio of $dN/d\phi$ distribution of ALICE LHC10h dataset to flat distribution (AMPT True). The reconstructed AMPT, and LHC11h with TPC only track cut, and LHC10h with Global SSD track cut were also drawn together for comparison.

956 The non-uniform ϕ distribution which is taken from ALICE LHC10h data are shown
957 in Fig.3.4. We use TPC only track cut, which have better ϕ distribution, but also LHC10h

958 with Global SDD and LHC11h distribution were shown together for comparison. As
959 seen in figure, the data from LHC10h period have worse flatness than AMPT simulation.
960 It becomes even worse in GlobalSSD track cut or LHC11h period data because of some
961 detector problems. (Some of SDD clusters in ITS detector were dead in 2010, and there
962 was reconstruction efficiency issue with TPC detector in 2011 data taking) The results
963 with AMPT data and modified AMPT data were calculated together and the difference
964 between them was taken into systematic uncertainties.

965 **3.3.2 Systematics from Event selection**

966 Following is the list of item for systemic uncertainty study about event selections.

967 **Z-vertex cut**

968 Because of limited acceptance of ALICE detector, primary vertex position along the
969 longitudinal direction is important to ensure for the uniform pseudo-rapidity distribution
970 over all events. The z-vertex distribution of ALICE LHC10h events are shown in Fig.3.5.
971 As described in previous chapter, the reconstructed vertex position in beam axis (z-
972 vertex) is required to be located within 10 cm of interaction point (IP). Since the different
973 z-vertex position may have an effect on effective η range. So these Z-vertex cut criteria
974 are important to ensure for the flat η distribution over all events. Instead of using the
975 original vertex range cut ($|z| < 10$ cm), we tried to reduce $|z| < 8$ cm for systematic
976 study.

977 **Magnetic polarization**

978 The events which we analyzed were recorded with two settings of the magnetic field
979 polarities, namely (++) and (-). For the default, we used all the events from both polar-
980 ized magnetic fields. The configuration of magnetic polarizations consist of almost the
981 same number of events. We measured the $SC(m, n)$ results from (++) or (-) categorized
982 events and compare to the default one.

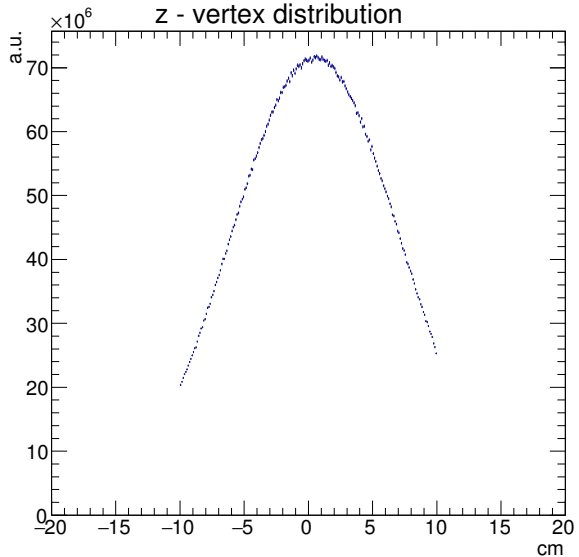


Figure 3.5: Z-vertex distribution of ALICE Pb + Pb $\sqrt{S_{NN}} = 2.76$ TeV with minimum bias triggered events

983 **Centrality determination**

984 The centrality of the given collision can be determined by various detectors and set-
 985 tings. By the default, the multiplicity of the VZERO detector(Both V0A and V0C) is
 986 used for centrality determinations with better than 2% of resolution. Another method of
 987 determine event centrality were using the multiplicity of tracks estimated by the stan-
 988 dalone TPC tracking or tracklet from SPD detector independently which have slightly
 989 worse resolution. We use these methods to study systematic uncertainty from centrality
 990 determination.

991 **Cut on outliers**

992 The outlier is an observation point that is different from other observations. In
 993 LHC10h datasets, there are some events which have many more TPC tracks than Global
 994 reconstructed tracks. These outliers is coming from pile-up like events or indicate ex-

995 experimental error. These kind of outliers usually are discarded from the data sets. In these
 996 case, we excluded the events which have Multiplicity of TPC except following criteria

$$32.1 + 1.59 \times M_{Global} < M_{TPC} < -40.3 + 1.22 \times M_{Global} \quad (3.15)$$

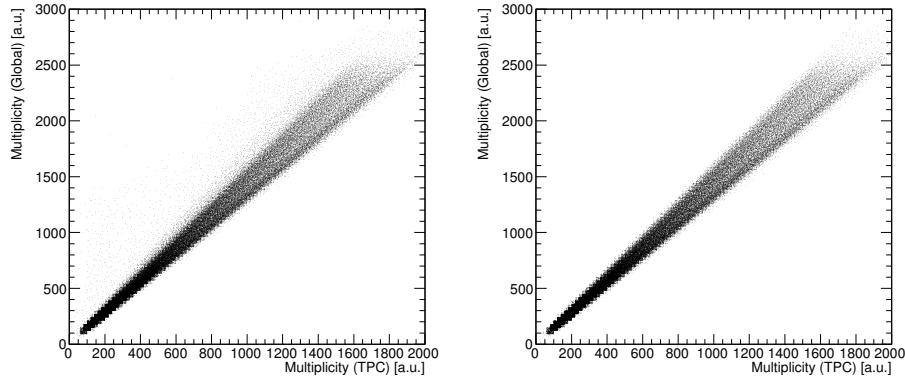


Figure 3.6: The 2-dim distribution of TPC multiplicity and Global multiplicity. Left is the before exclude outlier(left) and right figure is after exclude outlier(right) events.

997 3.3.3 Systematics from Track selection

998 Following is the list of item for systematic uncertainty study form track selections.

999 **Track filter bit**

1000 As can see the Fig.3.7, ϕ flatness vary as track selection filter cuts, and it might
 1001 affect the results of $SC(m, n)$ which is sensitive to ϕ distribution. This incompleteness
 1002 of ϕ distribution comes from the limited precision with the detector performance. And
 1003 each track filter cuts were evaluated by the thresholds on parameters used to select the
 1004 tracks at the reconstruction level. Usually TPC only track cuts have relatively good(flat)
 1005 ϕ distribution than GlobalSDD cut, but more fake and secondary tracks are included.
 1006 Also GlobalSDD cut gives two small holes in ϕ distribution.

1007 To estimate systematic uncertainty from the track selection filter cut, we measure the
 1008 results from different track selections and compare with the default setting.

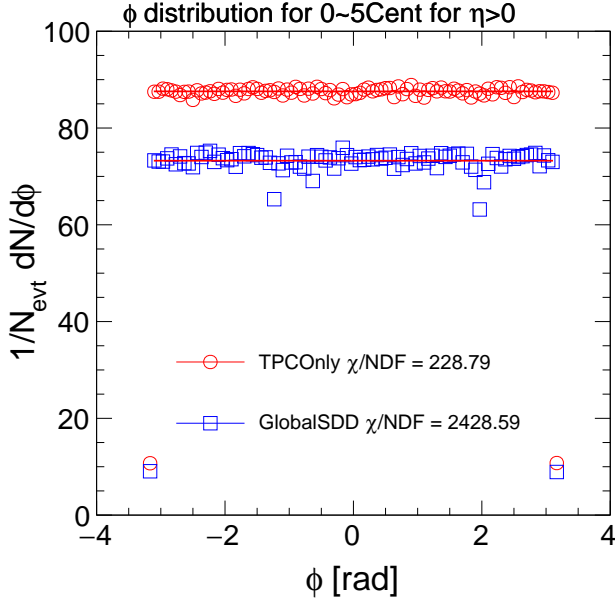


Figure 3.7: χ/NDF of $dN/d\varphi$ distribution from ALICE LHC10h data with TPC only track selection filter and Global SDD filter.

cut	filter bit	comments
TPCOnly	128 (7)	GetStandardTPCOnlyTrackCuts() + SetMinNClustersTPC(70)
GlobalSDD	96 (5 6)	GetStandardITSTPCTrackCuts2010() with requiring the first SDD cluster instead of an SPD cluster

Table 3.1: ALICE Track selection filter conditions

1009 Charge combination

1010 We used 4p- and 2p- correlation to measure $SC(m, n)$. The multiparticle cumu-
 1011 lants are expected to remove non-flow effect by cancellation each other, however it is
 1012 hard to prove there is perfectly absense of non-flow effects in $SC(m, n)$. To estimate
 1013 remain non-flow effects, such as re-reinteraction with other particles in the system after

leaving the domain, the modification of the jet-like two-particle correlations, resonance decays, and final state interactions (particularly Coulomb effects). Such flowing cluster contributes to cumulants by definition as being genuine four particle correlations, however, due to charge conservation, we will have in the cluster always particles of opposite charge. Therefore, by performing an independent analysis only with like-sign charges, we are estimating the contribution from flowing clusters.

Efficiency correction

The correction to p_T dependent efficiency were also tested, and taken into systematic uncertainty. Because of incompleteness of track reconstruction, correction steps are necessary to trace back from reconstructed tracks to the originally generated particles from the collisions. Usually this study were conducted with a Monte Carlo simulation such as HIJING for Pb+Pb collisions and PYTHIA for the p - p collisions. The single track reconstruction efficiency, and contamination form the secondary particles were shown in Fig.3.8

3.3.4 Overall systematic uncertainty

All systematic uncertainty checks discussed in this analysis were included in the final systematic uncertainty. All individual checks are performed independently and these all systematics were combined in quadrature to obtain the final uncertainty. The tabulated systematic uncertainties are listed below tables.

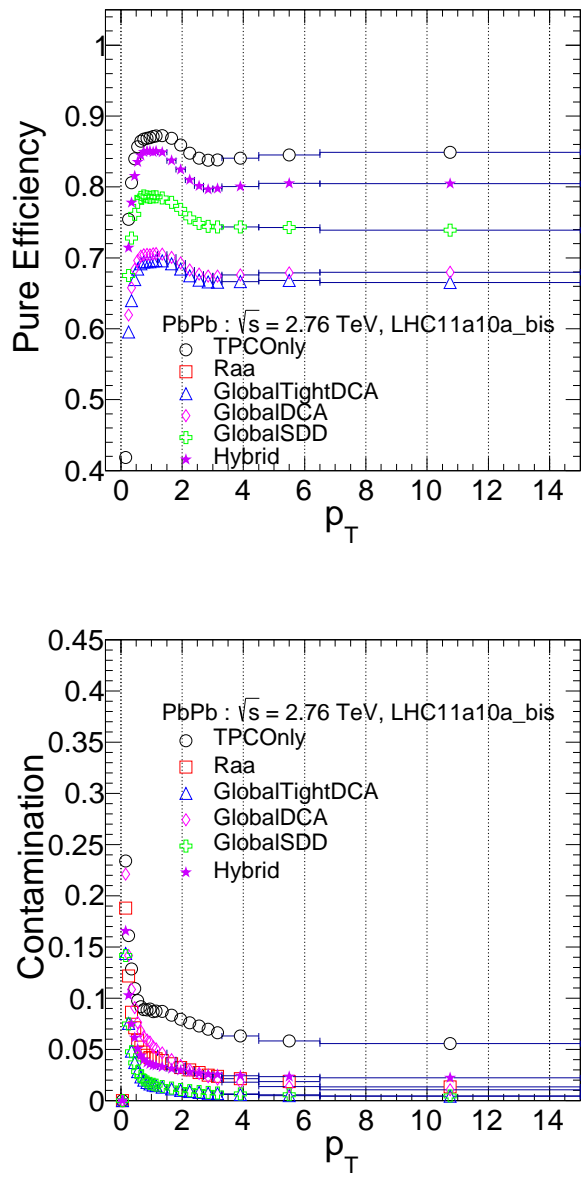


Figure 3.8: Tracking efficiency of single particle reconstruction as a function of p_T (left) and contamination of single particle as a function of p_T (right) for ALICE with various track selection filter

Type [%]	SC(3,2)	SC(4,2)	SC(5,2)	SC(5,3)	SC(4,3)
Non-uniform ϕ distribution	< 1	1.2	9.5	17.3	11.3
Track filter bit selection	8.4	4.9	9.1	9.1	11.9
Efficiency correction	3.1	4.4	1.5	1.7	1.3
Z-vertex cut	2.1	1.5	2.1	1.9	3.0
Charge combination	4.5	12.1	18.5	19.5	6.8
high multiplicity outliers	< 1	2	2.1	2.1	< 1
Magnetic field polarization	2.1	2.7	1.3	1.5	1.1
Centrality determination	< 1	< 1	3.1	7.6	1.5
Overall	10.8	17.9	22.8	28.8	18.4

Table 3.2: Systematic uncertainties of $SC(m, n)$. Overall systematics are quadratically merged results of each individual systematic error

Type [%]	NSC(3,2)	NSC(4,2)	NSC(5,2)	NSC(5,3)	NSC(4,3)
Non-uniform ϕ distribution	< 1	1.1	7.5	15.3	12.4
Track filter bit selection	7.3	4.9	8.4	12.1	11.1
Efficiency correction	3.1	3.4	1.5	1.7	1.3
Z-vertex cut	2.1	1.5	2.1	1.9	3.0
Charge combination	2.3	5.1	18.2	19.5	6.1
high multiplicity outliers	< 1	2	2.1	3.1	< 1
Magnetic field polarization	2.1	2.7	3.6	5.1	4.1
Centrality determination	< 1	< 1	1.4	1.5	< 1
Overall	9.1	8.1	22.2	28.3	18.5

Table 3.3: Systematic uncertainties of $NSC(m, n)$. Overall systematics are quadratically merged results of each individual systematic error

1033 **Chapter 4**

1034 **Results**

1035 **4.1 $SC(m, n)$ Results**

1036 **4.1.1 $SC(3, 2)$ and $SC(4, 2)$**

1037 The centrality dependence of $SC(4, 2)$ and $SC(3, 2)$ are presented in Fig.4.1. Positive values of $SC(4, 2)$ are observed for all measured centralities. This suggests a positive correlation between the event-by-event fluctuations of v_2 and v_4 . It also indicates that finding v_2 larger than average($\langle v_2 \rangle$) in an event enhances the probability of finding v_4 larger than average($\langle v_4 \rangle$) in that event. On the other hand, the negative results of $SC(3, 2)$ over all measured centralities show the anti-correlation between v_2 and v_3 flow harmonic magnitudes, which further implies that finding v_2 larger than average($v_2 > \langle v_2 \rangle$) enhancing the probability of finding smaller v_3 than average($v_3 < \langle v_3 \rangle$).

As discussed and evaluated order-by-order in [107], general cumulant formalism is applicable to any correlators eliminating non-flow correlations up to order $2k$ by means of a cumulant expansion. Also when compared with HIJING simulation data[108] does not include anisotropic collectivity, but has azimuthal correlations due to jet production (non-flow effects)[109]. It is found that both

$$\langle\langle \cos(m\varphi_1 + n\varphi_2 - m\varphi_3 - n\varphi_4) \rangle\rangle = \langle v_m^2 v_n^2 \rangle$$

and

$$\langle\langle \cos[m(\varphi_1 - \varphi_2)] \rangle\rangle \langle\langle \cos[n(\varphi_1 - \varphi_2)] \rangle\rangle = \langle v_m^2 \rangle \langle v_n^2 \rangle$$

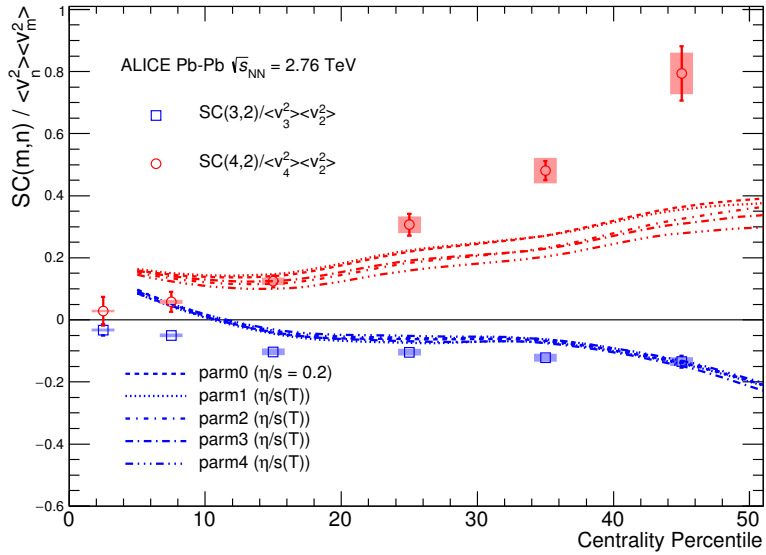
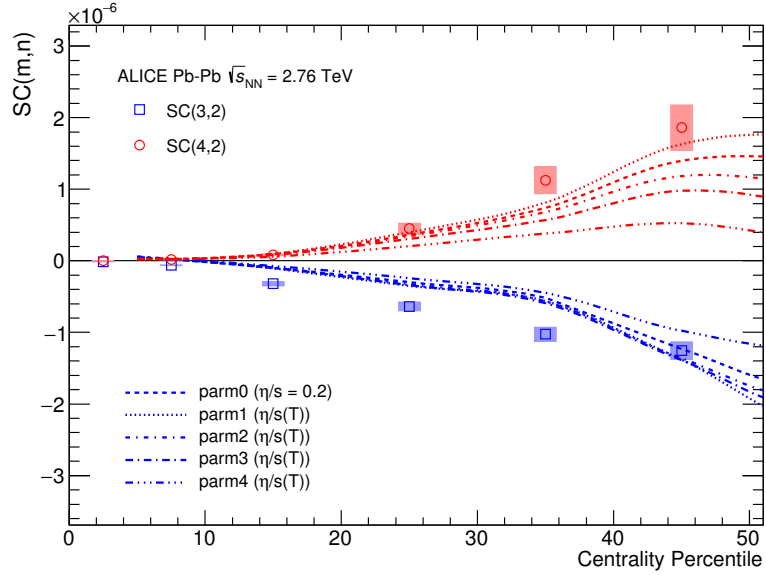


Figure 4.1: The results of $SC(3,2)$ (blue) and $SC(4,2)$ (red) with ALICE Pb+Pb $\sqrt{s_{NN}} = 2.76\text{TeV}$ as function of collision centrality (Top). The $NSC(m, n)$ results which scaled with $\langle v_m^2 \rangle \langle v_n^2 \rangle$ were placed in Bottom. The dashed lines are hydrodynamic prediction from H. Niemi with various η/s parametrizations [13]

1045 are not zero. However, the calculation of $SC(m, n)$ from HJING are compatible with
 1046 zero for all centralities (even for higher p_T as shown in Fig.4.2) and it suggest that the
 1047 $SC(m, n)$ are not coming from non-flow effects and insensitive to non-flow correlations.

1048 Moreover, systematics study using the same charge combination pair technique has
 1049 been done, which is another approach to estimate the non-flow effect. By using like-sign
 1050 track selection method, we can eliminate “flow cluster” effects due to charge conserva-
 1051 tion. As the result of systematic study, it was found that the difference between like-sign
 1052 and all charged measurements are only few% level and also we can found same trends
 1053 (positive and negative correlation for $SC(4, 2)$ and $SC(3, 2)$) in like-sign results. This
 1054 further illustrates that non-zero values of $SC(m, n)$ cannot be explained by non-flow
 1055 effect, but confirms the existence of correlation (and anti-correlations) between v_n and
 1056 v_m harmonics.

1057 The $SC(m, n)$ results show that the correlation strength in both $SC(m, n)$ and
 1058 $NSC(m, n)$ increase non-linearly up to centrality 50%.

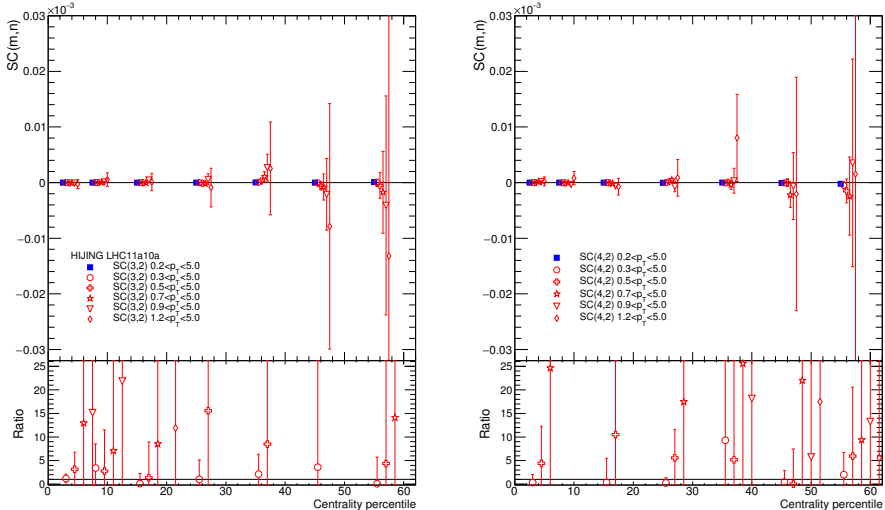


Figure 4.2: The result of $SC(3,2)$ and $SC(4,2)$ with HIJING simulations. Defaults($0.2 < p_T < 5.0 GeV/c$) are drawn as full square with blue color, and different minimum cut conditions are listed in legend. A small shifts along the x axis were applied for better visibility

1059 **4.1.2 Model Comparison**

1060 Various models have been used in this study. The HIJING model [95, 107] was
1061 used to estimate the strength of non-flow correlations (typically few-particle correlations
1062 insensitive to the collision geometry) as described in previous section.

1063 The $SC(m, n)$ from hydrodynamic prediction with pQCD, where the initial energy
1064 density profiles are calculated using a next-to-leading order perturbative-QCD+saturation
1065 model [110, 111] + various shared viscosity η/s parameterizations were performed by
1066 H. Niemi [13]. The subsequent spacetime evolution is described by relativistic dissipa-
1067 tive fluid dynamics with different parametrizations for the temperature dependence of
1068 the shear viscosity to entropy density ratio $\eta/s(T)$. Each of the $\eta/s(T)$ parametrizations
1069 is adjusted to reproduce the measured v_n from central to mid-peripheral collisions.

1070 The fluid hydrodynamic predictions with the different parameterizations for the tem-
1071 perature dependence of the shear viscosity to entropy ratio $\eta/s(T)$ are shown shown in
1072 Figure 4.1 as dashed line. Roughly the hydrodynamic calculations capture qualitatively
1073 the centrality dependence, but not quantitatively. Both $SC(3, 2)$ with data and hydro-
1074 dynamics have negative values for all centralities, while $SC(4, 2)$ results have positive
1075 values over all measured centralities. However, there is no single centrality for which
1076 a given $\eta/s(T)$ parameterization describes both $SC(3, 2)$ and $SC(4, 2)$ simultaneously.
1077 On the other hand, the same hydrodynamic calculations capture the centrality depen-
1078 dence of the individual v_n quantitatively [112].

1079 $NSC(3, 2)$ and $NSC(4, 2)$ are also compared to the same model on the right in
1080 Fig. 4.1. While $NSC(3, 2)$ does not show sensitivity to different $\eta/s(T)$ parameteri-
1081 zations, $NSC(4, 2)$ exhibit much better sensitivity than $NSC(3, 2)$ observable and the
1082 individual flow harmonics [13]. These findings indicate that $NSC(3, 2)$ observable is
1083 sensitive mainly to the initial conditions, while $NSC(4, 2)$ observable is sensitive to
1084 both the initial conditions and the system properties, which is consistent with the predic-
1085 tion from [97].

1086 However, the sign of $NSC(3, 2)$ is positive in the models in 0-10% central colli-
1087 sions while it is negative in data. In the most central collisions the anisotropies origi-
1088 nate mainly from fluctuations, i.e. the initial ellipsoidal geometry characteristic for mid-

1089 central collisions plays little role in this regime. Hence this observation will help to
1090 understand the fluctuations in initial conditions better.

1091 $NSC(4, 2)$ observable shows better sensitivity for different $\eta/s(T)$ parameteriza-
1092 tions, i.e. medium property but the model cannot describe the centrality dependence
1093 nor the absolute values. These observed distinct discrepancies between data and models
1094 might indicate that the current understanding of initial conditions used in the model need
1095 to be revisited to further constrain the $\eta/s(T)$, considering the difficulties on separating
1096 the role of the η/s from the initial condition to the final state particle anisotropies [36,
1097 62]. Hence the use of $SC(m, n)$ and $NSC(m, n)$ can provide new constraints on the
1098 detailed modeling of the initial-state condition and the fluctuations of the medium cre-
1099 ated in heavy ion collisions and the better constraints on the initial-state conditions will
1100 certainly improve the uncertainties of determining $\eta/s(T)$.

1101 The $NSC(m, n)$ were compared to MC-Glauber using wounded nucleon (WN) and
1102 binary collisions (BC) weights models to check linear and non-linear response from ini-
1103 tial geometry. Assuming only linear response $v_n \propto \epsilon_n$, we expect that the $NSC(m, n)$
1104 evaluated in coordinate space are able to capture the measurement of centrality depen-
1105 dence of $NSC(m, n)$ in the momentum space. In this case the correlation between
1106 the n th and m th order harmonics were estimated with calculation of $SC(m, n)$ in the
1107 coordinate space as define as

$$SC(m, n)_\epsilon / \langle \epsilon_n^2 \rangle \langle \epsilon_m^2 \rangle \equiv (\langle \epsilon_n^2 \epsilon_m^2 \rangle - \langle \epsilon_n^2 \rangle \langle \epsilon_m^2 \rangle) / \langle \epsilon_n^2 \rangle \langle \epsilon_m^2 \rangle \quad (4.1)$$

1108 Where the ϵ_n is the n th order coordinate space anisotropy as defined in [57]. Since
1109 there are two different scenarios of the MC-Glauber model, we tested with both wounded
1110 nucleon (WN) and binary collisions (BC) weights and results are shown in Fig.4.3.
1111 An increasing trend from central to peripheral collisions with different sign has been
1112 observed and there is a large deviation of $NSC(4, 2)$ between ALICE data and MC-
1113 Glauber model. This deviation increase from central to peripheral collision regions and
1114 this might indicate the contribution of the non-linear response of initial condition though
1115 hydrodynamic evolution. Moreover, the MC-Glauber model with $NSC(3, 2)$ describes
1116 better the data than $NSC(4, 2)$, because the $NSC(3, 2)$ appears to be sensitive only to

initial conditions and not sensitive to hydrodynamic properties (η/s).

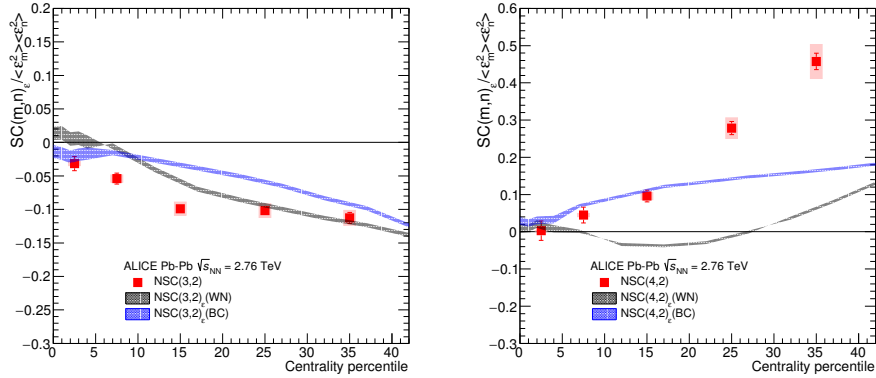


Figure 4.3: $NSC(m, n)$ (red) and $NSC(m, n)_\epsilon$ (correlation in coordinate space) by using MC-Glauber models with wounded nucleon (WN) and binary collisions (BC) weights.

$SC(m, n)$ with AMPT [113, 114, 115] simulation with various configurations was also tested. The configuration of AMPT are listed in Table 4.1.2. With changing configuration of AMPT simulations, we may estimate the effects of initial conditions and finite states effects.

Even though thermalization could be achieved in collisions of very large nuclei and/or at extremely high energy, the dense matter created in heavy ion collisions may not achieve full thermal or chemical equilibrium as a result of its finite volume and energy. To address such non-equilibrium many-body dynamics, AMPT has been developed, which includes both initial partonic and final hadronic interactions and the transition between these two phases of matter. For the initial conditions, the AMPT model uses the spatial and momentum distributions of hard minijet partons and soft strings from the HIJING model [95, 107]. The AMPT model can be run in two main configurations, the default and the string melting model. In the default version, partons are recombined with their parent strings when they stop interacting. The resulting strings are later converted into hadrons using the Lund string fragmentation model [116, 117]. In the string melting version, all the excited strings that are not projectile and target

nucleons not experiencing any interactions are converted to partons according to the flavor and spin structures of their valence quarks. The advantage of this choice is that the AMPT model with string melting reduces to HIJING results in the absence of partonic and hadronic interactions as these partons would then find each other as closest partners at the same freeze-out time and thus coalesce back to the original hadron. In the AMPT model with string melting, the initial strings are melted into partons whose interactions are described by the ZPC parton cascade model [118]. These partons are then combined into the final-state hadrons via a quark coalescence model. [119]

In both configurations, the dynamics of the subsequent hadronic matter is described by a hadronic cascade based on a Relativistic Transport (ART) model [120] which also includes resonance decays. The third version presented in this article is based on the string melting configuration, in which the hadronic rescattering phase is switched off to study its influence to the development of anisotropic flow. The input parameters used in both configurations are: $\alpha_s = 0.33$, a partonic cross-section of 1.5 mb, while the Lund string fragmentation parameters were set to $\alpha = 0.5$ and $b = 0.9 \text{ GeV}^{-2}$. Even though the string melting version of AMPT [121, 115] reasonably reproduces particle yields, p_T spectra, and v_2 of low- p_T pions and kaons in central and mid-central Au-Au collisions at 200 GeV and Pb-Pb collisions at 2.76 TeV [122], it was seen clearly in the recent study [123] that it fails to quantitatively reproduce the measurements. It turns out that the radial flow in AMPT is 25% lower than the measured value at the LHC, which indicates that the unrealistically low radial flow in AMPT is responsible for the quantitative disagreement. The detail configurations on AMPT settings used for this article and the comparisons of p_T differential v_n for pions, kaons and protons to the data can be found in [123].

The results of comparison to AMPT are shown in Fig.4.4. As for $SC(3, 2)$, neither of the settings can describe the data and somewhat the setting with the default AMPT model follows the trend of the data closest. The same setting can describe $NSC(3,2)$ fairly well and also the sign of $NSC(3,2)$ is well reproduced by this setting while all the hydrodynamic calculations in this article failed to describe the sign of the observable in most central collisions.

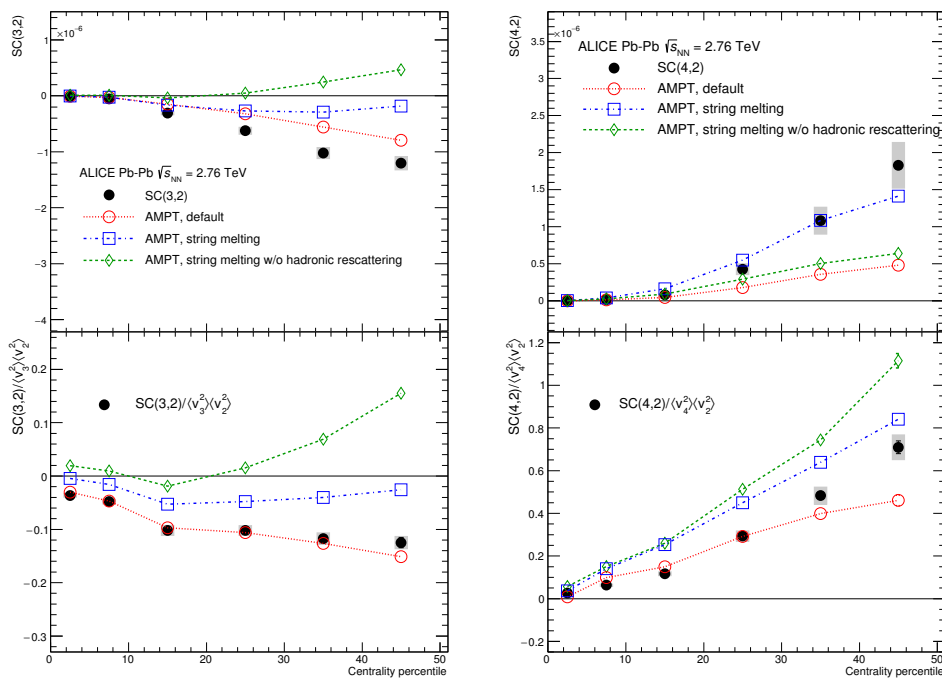


Figure 4.4: The result of $SC(3,2)$ and $SC(4,2)$ with ALICE data and comparison to various AMPT simulations with different settings. The upper figures are the results of $SC(m,n)$ and the lower figures are the results of $NSC(m,n)$

Setting	String Melting	Rescattering
AMPT Default	OFF	ON
AMPT String melting	ON	ON
AMPT String melting w/o hadronic rescattering	ON	OFF

Table 4.1: Configurations of AMPT simulation dataset which correspond to ALICE LHC10h data with Pb+Pb $\sqrt{S_{NN}} = 2.76\text{TeV}$

1164 Interestingly the string melting AMPT model can't capture the data well where the
 1165 strength of the correlation is weaker than the default model. The third version based on
 1166 the string melting configuration with the hadronic rescattering phase off is also shown
 1167 to study its influence. This late hadronic rescattering stage makes both $SC(3, 2)$ and
 1168 $NSC(3, 2)$ stronger in the string melting AMPT model but it is not enough to describe
 1169 the data.

1170 Further we investigated why the default AMPT model can describe $NSC(3, 2)$ fairly
 1171 well but underestimates $SC(3, 2)$. By taking the differences in the individual flow har-
 1172 monics (v_2 and v_2) between the model and data into account, we was able to recover the
 1173 data. The discrepancy in $SC(3, 2)$ can be explained by the overestimated individual v_n
 1174 values reported in [123] in all the centrality ranges.

1175 In case of $SC(4, 2)$, the string melting AMPT model can fairly describe the data
 1176 while the default model underestimates it. $NSC(4, 2)$ is slightly overestimated by the
 1177 same setting which can describe $SC(4, 2)$ but the default AMPT model can describe
 1178 the data better. The influence of the hadronic rescattering phase for $NSC(4, 2)$ is op-
 1179 posite to other observables ($SC(3, 2)$, $NSC(3, 2)$ and $SC(4, 2)$), where the hadronic
 1180 rescattering make $NSC(4, 2)$ slightly smaller. It should be noted that the better agree-
 1181 ment for $SC(m, n)$ should not be overemphasized since there are discrepancies in the
 1182 individual v_n between AMPT and data as it was demonstrated for $SC(3, 2)$. Hence the
 1183 simultaneous description of $SC(m, n)$ and $NSC(m, n)$ should give better constrains to
 1184 the parameters in AMPT.

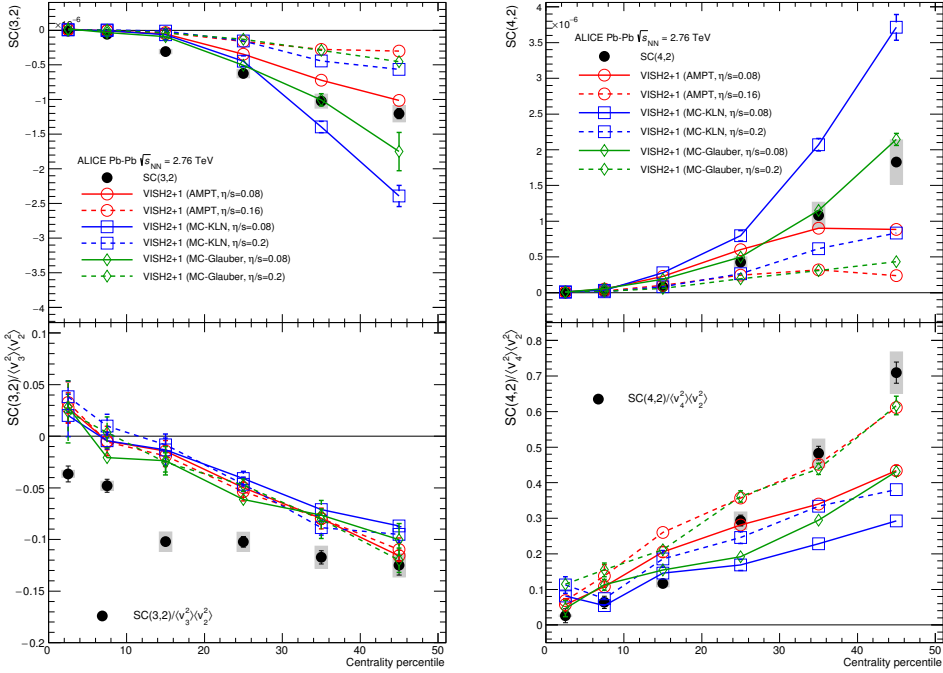


Figure 4.5: Result of $SC(3, 2)$ (left) and $SC(4, 2)$ (right) with LHC10h data and various VISH2+1 calculation with different settings. The three initial conditions from AMPT, KLN, and Glauber simulations are drawn as a different color. Furthermore, the hydrodynamic properties of η/s are shown as line style, the small share viscosity ($\eta/s=0.08$) are shown as solid line, and large share viscosity ($\eta/s=0.2$ for KLN and Glauber, 0.16 for AMPT) is drawn as dashed line. Upper figures are the result of $SC(m, n)$ and lower figures are results of $NSC(m, n)$

1185 The comparison to VISH2+1 calculation are shown in Fig.4.5. The VISH2+1 [124]
1186 is an event-by-event theoretical framework model for relativistic heavy-ion collision
1187 based on (2+1)-dimensional viscous hydrodynamics which describes both the QGP fluid
1188 and the highly dissipative and even off-equilibrium late hadronic stage with fluid-dynamics.
1189 With well tuned transport coefficients, decoupling temperature and some well-chosen
1190 initial conditions (like AMPT [125, 126, 127] etc.), it could fit many related soft hadron
1191 data, such as the p_T spectra and different flow harmonics at RHIC and the LHC [128,
1192 129, 31, 126]. Three different initial conditions (MC-Glauber, MC-KLN and AMPT)
1193 along with different constant η/s parametrizations are used in the model. Traditionally,
1194 the Glauber model constructs the initial entropy density of the QGP fireball from a mix-
1195 ture of the wounded nucleon and binary collision density profiles [130], and the KLN
1196 model assumes the initial entropy density is proportional to the initial gluon density cal-
1197 culated from the corresponding k_T factorization formula [131]. In the Monte-Carlo ver-
1198 sions (MC-Glauber and MC-KLN) [5, 132, 133], additional initial state fluctuations are
1199 introduced through the position fluctuations of individual nucleons inside the colliding
1200 nuclei. For the AMPT initial conditions [126, 127, 125], the fluctuating energy density
1201 profiles are constructed from the energy decompositions of individual partons, which
1202 fluctuate in both momentum and position space. Compared with the MC-Glauber and
1203 MC-KLN initial conditions, the additional Gaussian smearing parameter in the AMPT
1204 initial conditions makes the typical initial fluctuation scales changeable which gives rise
1205 to non-vanishing initial local flow velocities [127].

1206 As shown in the Fig.4.5, all the models with the large share viscosity regardless
1207 of the initial conditions ($\eta/s=0.2$ for MC-KLN and MC-Glauber initial conditions and
1208 $\eta/s = 0.16$ for AMPT initial condition) failed to capture the centrality dependence
1209 of $SC(3, 2)$ and $SC(4, 2)$. However, for the normalized case(NSC), all the results
1210 with different parameters do not have much difference as like original $SC(m, n)$. It
1211 may suggest that the η/s parametrization affects the single flow magnitude, (generally
1212 large share viscosity(η/s) leads short mean free path(λ_{mfp}) and it decreases the flow
1213 magnitudes) rather than affect on correlations between flow orders. And among the
1214 models with small shear viscosities ($\eta/s=0.08$), the one with the AMPT initial condition

describes the data better both for $SC(3, 2)$ and $SC(4, 2)$ but they cannot describe the data quantitively for most of the centrality ranges. As similarly as the above mentioned hydrodynamic calculations [13], the sign of the $NSC(3, 2)$ in these models is opposite to the data in 0-10% central collisions. $NSC(3, 2)$ don't show sensitivity to neither initial conditions nor η/s parameterizations and cannot be described by these models quantitively. However, for $NSC(4, 2)$, it is sensitive both to initial conditions and η/s parameterizations. Even though $NSC(4, 2)$ is favored both by AMPT initial condition with $\eta/s=0.08$ and MC-Glauber initial condition with $\eta/s=0.20$, $SC(4, 2)$ can be only described by smaller η/s from AMPT and MC-Glauber initial conditions. Therefore the Glauber initial condition with $\eta/s=0.20$ model can be ruled out and we come to a conclusion based on the tested model parameters that η/s should be small and AMPT initial condition is favored by the data.

4.2 Higher order flow harmonics results

In this section, we will present the results of the correlation between higher order flow harmonics up to 5th order. The results with q-Cumulants method (SP method) with $|\eta| < 0.8$, $0.2 < p_T < 5.0\text{GeV}/c$ from ALICE data are shown. The lower order $SC(m, n)$ are scaled down and drawn together as colored band for comparison.

As predicted as hydrodynamic calculation [106] the correlation between v_3^2 and v_4^2 is negative and the others are positive. The correlation between higher harmonics (v_3 and v_4 , v_2 and v_5 , v_3 and v_5) become smaller for more central collisions, and it suggests that the correlation is likely due to the non-linear contributions of higher order flow harmonics like v_4 and v_5 [134].

However, unlike $SC(m, n)$, $NSC(m, n)$ results with the higher order flow harmonics show almost same order of the correlation strength as the lower order flow harmonic correlations ($NSC(3, 2)$ or $NSC(4, 2)$). $NSC(4, 3)$ is comparable to $NSC(3, 2)$ and one finds that a hierarchy $NSC(5, 3) > NSC(4, 2) > NSC(5, 2)$ holds for most of centrality ranges within the errors. These results indicate that the lower oder harmonic correlations ($SC(3, 2)$ and $SC(4, 2)$) are larger than higher order harmonic correlations ($SC(4, 3)$, $SC(5, 2)$, and $SC(5, 3)$), not only because of the correlation strength itself

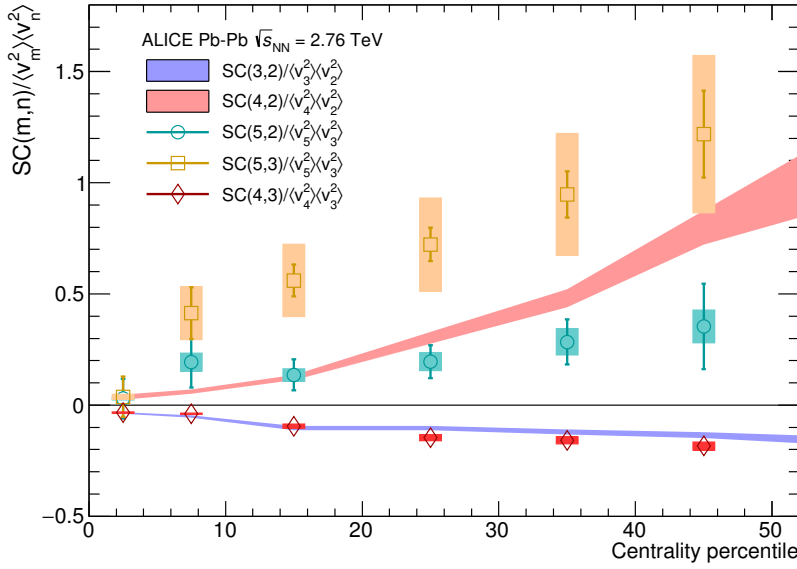
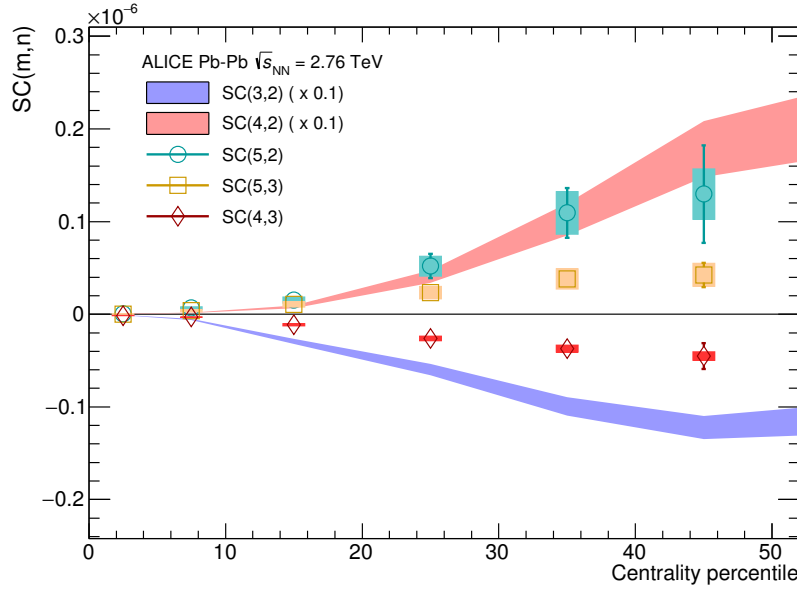


Figure 4.6: The results of $SC(m, n)$ (upper figure) and $NSC(m, n)$ (bottom figure) with higher order up to 5th flow harmonics with q-Cumulants method from ALICE Pb+Pb $\sqrt{s_{NN}} = 2.76$ TeV. Note that The lower order $SC(m, n)$ are scaled down by 0.1. Both $SC(m, n)$ and $NSC(m, n)$ with lower orders are drawn as colored band and statistical and systematical errors were quadratically merged.

1244 but also the individual flow strength. $SC(5, 2)$ is stronger than $SC(5, 3)$, however as for
 1245 NSC , the correlation between v_5 and v_3 is stronger than the correlation between v_5 and
 1246 v_2 .

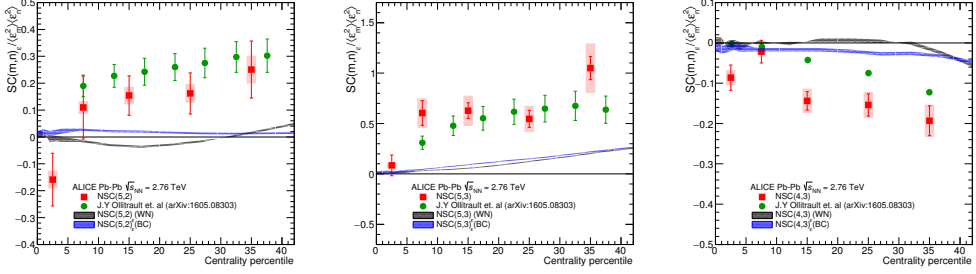


Figure 4.7: The results of higher order $NSC(m, n)$ and comparison to MC-Glauber models and prediction from J.Y Ollitraults [14]

1247 The $NSC(m, n)$ with higher order harmonics were compared to MC-Glauber to
 1248 check the response (both linear and non-linear) of initial geometry. The $NSC(m, n)$ in
 1249 coordinate space (as defined in Eq.4.1) with both WN and BC weights were compared
 1250 and shown in Fig.4.7. The large differences between MC-Glauber models (both WN and
 1251 BC) and data shows that the correlation between flow harmonics can not be explained
 1252 by only linear contribution of initial fluctuation. Also the prediction from J.Y Ollitraults
 1253 from ALICE lower order $SC(m, n)$ and EP (Event Plane) correlation from ATLAS with
 1254 few assumptions [14] were shown together as green marker in Fig.4.7. Although it pre-
 1255 dict better than any other existing theoretical models, however still have some deviation
 1256 between data for $NSC(4, 3)$ case.

1257 The extracted results from particle level AMPT simulations in the same way as for
 1258 the data are compared to the data in Fig.4.8. The string melting AMPT model describes
 1259 $SC(5,2)$ and $SC(5,3)$ well. The same setting describes only $NSC(5, 3)$. However, it
 1260 overestimates $NSC(5, 2)$. However the default AMPT model can describe $NSC(5, 3)$
 1261 and $NSC(5, 2)$ fairly well as similarly as $NSC(3, 2)$ and $NSC(4, 2)$. In case of
 1262 $SC(4, 3)$, neither of the settings can describe the data but the default AMPT model
 1263 follows the data closest. The string melting AMPT model fails to describe $SC(4, 3)$

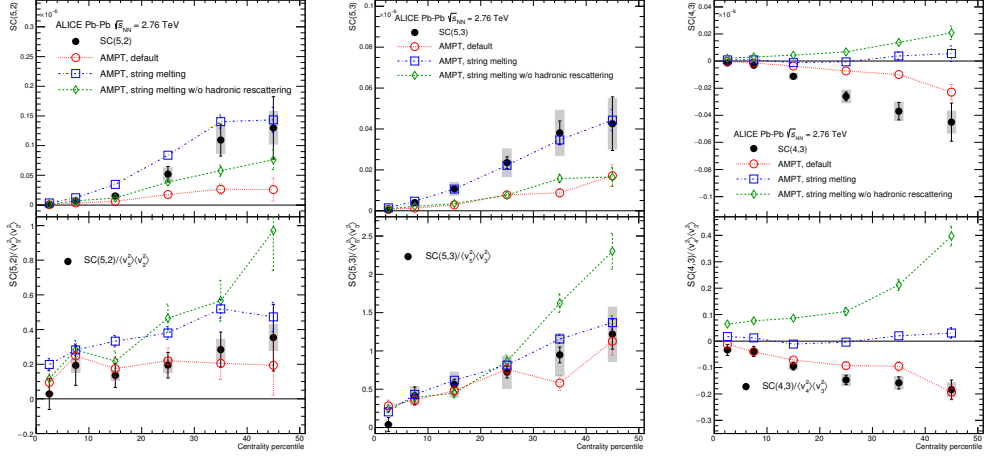


Figure 4.8: The results of $SC(5,2)$, $SC(5,3)$ and $SC(4,3)$ and comparison to various AMPT simulations with different settings. Upper figures are the results of $SC(m,n)$ and the lower figures are the results of $NSC(m,n)$

and $NSC(4,3)$. In summary, the default AMPT model describes the normalized case ($NSC(m,n)$) from lower to higher order harmonic correlation while the string melting AMPT model overestimates $NSC(5,2)$ and underestimates (or very weak correlations) $NSC(4,3)$.

The event-by-event calculation from VISH by using a hybrid approach based on (2+1)-dimensional viscous hydrodynamics(VISH2+1) were tested and shown in Fig.4.9. All the models with the large share viscosity regardless of the initial conditions ($\eta/s=0.2$ for MC-KLN and MC-Glauber initial conditions, and $\eta/s = 0.16$ for AMPT) failed to capture the centrality dependence of $SC(5,2)$, $SC(5,2)$, and $SC(5,3)$ more clearly than lower order harmonic correlations ($SC(3,2)$, $SC(4,2)$). And among the models with small shear viscosity ($\eta/s=0.08$), the one from the AMPT initial condition describes the data much better than the other initial conditions. A quite clear separation between different initial conditions is observed for these higher order harmonics correlations compared to the lower order harmonic correlations. $NSC(5,2)$ and $SC(5,3)$ are quite sensitive to both the initial conditions and the η/s parametrizations. As similarly

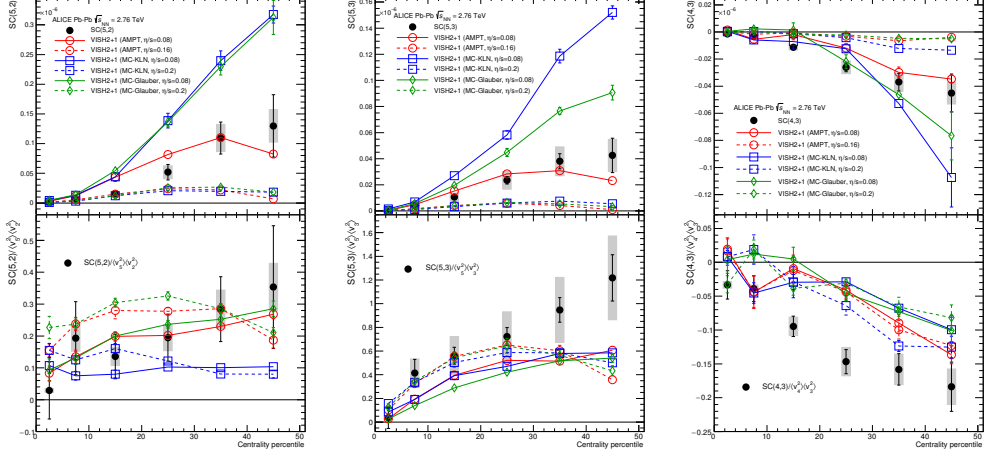


Figure 4.9: Result of $SC(5, 2)$, $SC(5, 3)$ and $SC(4, 3)$ with ALICE data and comparison to various VISH2+1 calculation with different settings. The configurations are same as Fig.4.5

as the above mentioned hydrodynamic calculations [13], the sign of the $NSC(4, 3)$ in these models is opposite to the data in 0-10% central collisions. $NSC(4, 3)$ shows sensitivity to both initial conditions and η/s parameterizations while $NSC(3, 2)$ didn't show sensitivity to neither initial conditions nor η/s parameterizations. $SC(4, 3)$ data is clearly flavoured by smaller η/s but $NSC(4, 3)$ cannot be described by these models quantitatively.

4.3 p_T dependence of $SC(m, n)$ and $NSC(m, n)$

To analyze p_T dependence of $SC(m, n)$ and $NSC(m, n)$ result, we set various cut conditions for p_T of measuring particles, instead of using all charged hadrons with $0.2 < p_T < 5.0$ GeV/c in $|\eta| < 0.8$ region. The simplest approach to analyze p_T dependence is to apply different p_T bin windows when measuring $SC(m, n)$. But the number of particles in each p_T bin groups decreases rapidly as function of p_T and the number of combination for cumulants pair will decrease even more rapidly ($\sim \frac{1}{n^4}$) and this method causes large statistical fluctuations. Because the original $SC(m, n)$ has only the order of few 10^{-6} strength signal, it is not simple to get clear p_T dependence from

1293 different p_T window bins from a large statistical fluctuations. To prevent the statistical
1294 fluctuation issue, we apply minimum p_T cuts, instead of p_T bin-by-bin windows. In
1295 this analysis, we tested $SC(m, n)$ s (and also $NSC(m, n)$ s) with different p_T conditions
1296 from $0.2 \sim 5.0\text{GeV}/c$ to $1.5 \sim 5.0\text{GeV}/c$.

1297 The result of p_T dependence with $SC(3, 2)$ and $SC(4, 2)$ is shown in Fig.4.10. As
1298 seen in figure, the strength of $SC(m, n)$ correlation becoming larger as function of min-
1299 imum p_T . This indicates that the relationship between event-by-event fluctuation of two
1300 different flow harmonics v_m and v_n is stronger in high p_T region. This p_T dependence
1301 correlation is relatively small in central collision centralities and large in non-central col-
1302 lisions. However, this correlation between flow harmonics and p_T is not clearly shown
1303 in $NSC(m, n)$ s. The $NSC(m, n)$ results are aligned all together and consistent within
1304 errors. The ratio to default cut ($0.2 < p_T < 5.0\text{GeV}/c$) is nearly 1 for all centrality.
1305 This suggests that the p_T dependence of $SC(m, n)$ are not solely comes from the corre-
1306 lation between flow harmonics but comes from the strength dependence of p_T of single
1307 v_n values. Minimum p_T cuts are extended to $1.5\text{ GeV}/c$ and the results are shown in
1308 Fig.4.11. Even in higher minimum p_T cuts, there is no clear p_T dependence in nor-
1309 malized $SC(3, 2)$ or $SC(4, 2)$. For detail study of p_T dependence of $NSC(m, n)$, the
1310 $NSC(m, n)$ as function of minimum p_T cuts are prepared in Fig.4.12. Unlike AMPT
1311 prediction, the results from the data does not have clear p_T dependence up to 40% colli-
1312 sion centralities. In 40-50% collision centrality region, there is a slightly decreased slope
1313 in $NSC(3, 2)$ but it is not enough to say that there is p_T dependence for $NSC(3, 2)$.
1314 For AMPT simulations, AMPT with string melting configuration failed to capture data
1315 result. These AMPT simulation predict that $NSC(m, n)$ increase as a function of min-
1316 imum p_T and turns over to positive values around minimum $p_T \sim 1.0\text{GeV}/c$. But in
1317 LHC10h data, the results remains in negative values for all minimum p_T bins, and cen-
1318 trality bins. Also for $NSC(4, 2)$ cases, only AMPT default which has the configuration
1319 without string melting, has similar values with data. The others (AMTP with string melt-
1320 ing) predict increase of $NSC(4, 2)$ from around $\sim 1\text{GeV}/c$ minimum p_T cuts, and failed
1321 to reproduce the data.

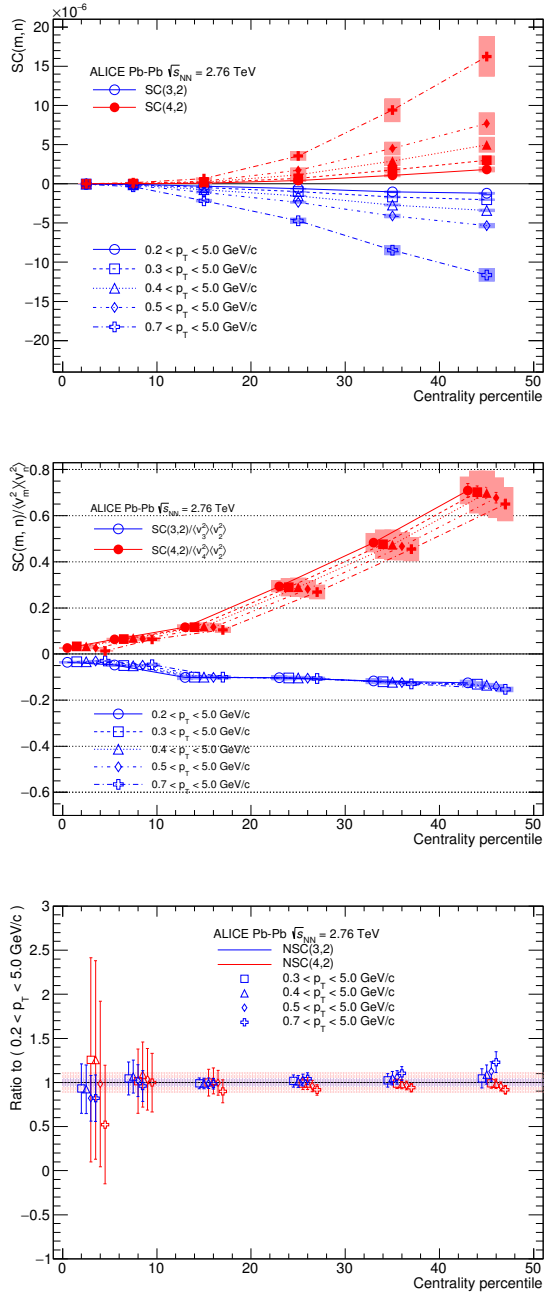


Figure 4.10: The results of $SC(3,2)$ and $SC(4,2)$ with various minimum p_T cut conditions (Top) and results of $NSC(3,2)$ and $NSC(4,2)$ (Middle). The ratio of $NSC(m, n)$ results with various minimum p_T cut conditions to default ($0.2 < p_T < 5.0 \text{ GeV}/c$) are shown in bottom figure.

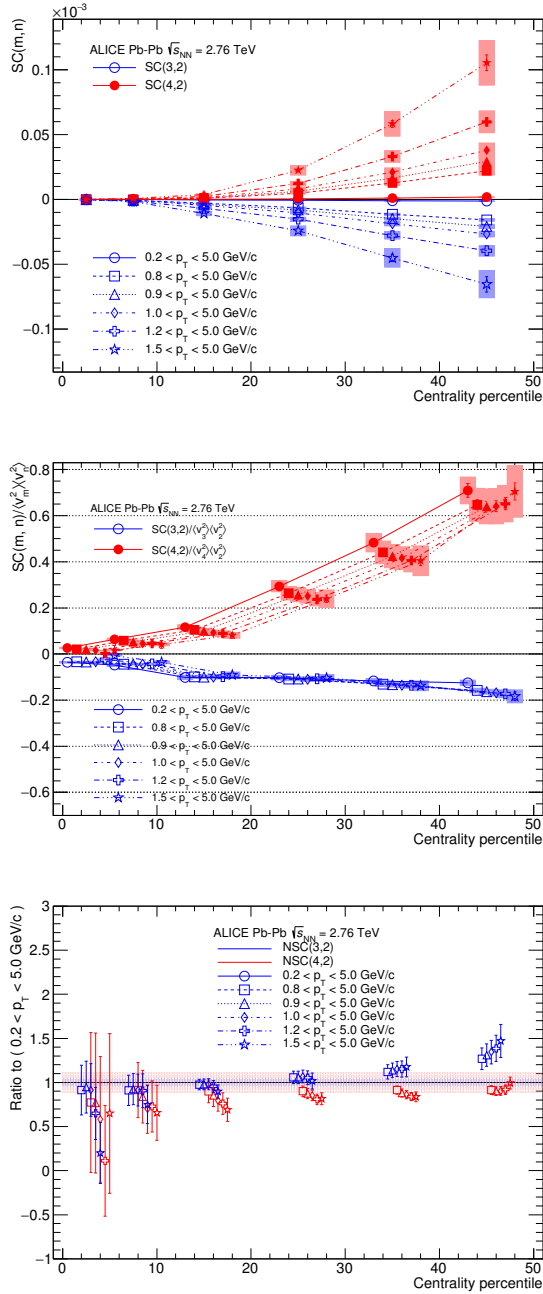


Figure 4.11: The results of $SC(3,2)$ and $SC(4,2)$ with various minimum p_T cut conditions (Top) and results of $NSC(3,2)$ and $NSC(4,2)$ (Middle). The ratio of $NSC(m, n)$ results with various minimum p_T cut conditions to default ($0.2 < p_T < 5.0 \text{ GeV}/c$) are shown in bottom figure.

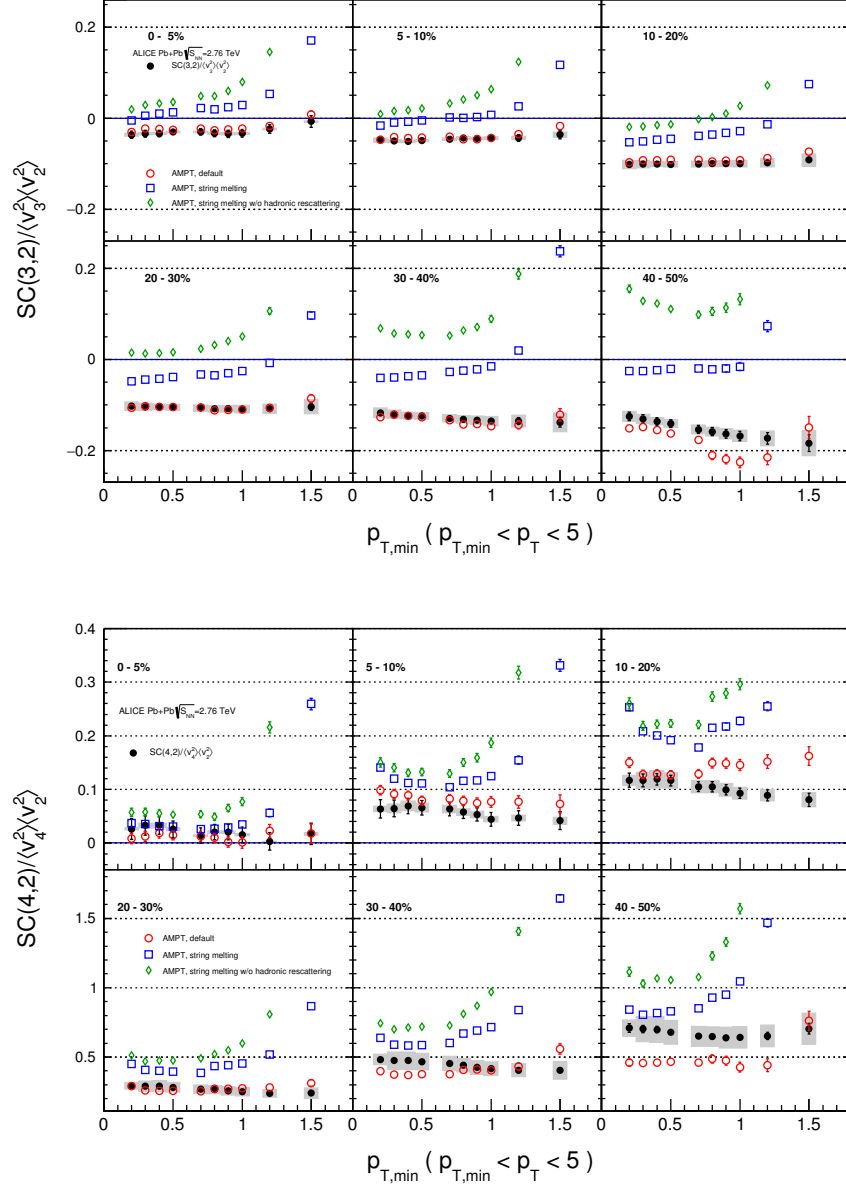


Figure 4.12: $NSC(3,2)$ (Top) and $NSC(4,2)$ (Bottom) as a function of minimum p_T cuts with ALICE Pb+Pb $\sqrt{S_{NN}} = 2.76\text{TeV}$. The AMPT simulation results are drawn together as colored band for comparison. The corresponding AMPT configurations are shown in legend.

1322 **4.4 Method comparison**

1323 The Eq.3.2 is based on the multi-particle q-Cumulants method(i.e. QC method),
1324 but it can be also obtained by calculating moments [106] as discussed in the previous
1325 section3.2.

1326 As seen in Fig.4.13 in both methods, the flow harmonics with 2nd and 4th are corre-
1327 lated. On the other hand, 2nd and 3rd harmonics are anti-correlated. The strength of cor-
1328 relation is small in the central collision region and becomes stronger in non-central colli-
1329 sion in both q-Cumulant method(QC) and Scalar Product method(SP). Also $NSC(m, n)$
1330 which is divided by products $\langle v_m^2 \rangle \langle v_n^2 \rangle$, in order to obtain the normalized observables are
1331 shown and suggests the same trend but a large deviation especially for $SC(4, 2)$. HIJING
1332 simulations results from SP methods are shown together for comparison.

1333 The advantage of using the SP method is that calculations are much simpler and
1334 faster in estimating the correlation between flow harmonics. Instead of calculating par-
1335 ticle pair of 4- or 2- cumulants, the SP method needs only one calculation between mea-
1336 sured n^{th} order flow Q -vector. The other advantage of the SP method is that it can be
1337 applied for not only $SC(m, n)$ which observables for flow “magnitudes” correlation, but
1338 also for the flow ”direction” correlations like event-plane correlation. [9] or non-linear
1339 response of flow harmonics [135].

1340 However, the disadvantage of SP methods is (likely) under estimation of $SC(m, n)$
1341 in low multiplicity regions. This effects were discussed with ToyMC simulation in Ap-
1342 pendix A. Because of this issue of difference between two different methods and inaccu-
1343 racy(under estimation) of SP method in low multiplicity regions, we used all the result
1344 from QC method as the default in this analysis.

1345 **Method comparison of higher order harmonics**

1346 Also $SC(m, n)$ and $NSC(m, n)$ results with higher order flow harmonics (up to
1347 5th order) were measured by the SP method, and the results are shown in Fig.4.14. For
1348 the higher order, because of statistical fluctuation for peripheral collisions, results were
1349 only taken from the 0% to 40% collision centrality regions. As a result, the two methods
1350 shows the consistent values within errors.

1351 **p_T dependence of $SC(m, n)$ with SP method**

1352 The p_T dependence of $SC(m, n)$ and $NSC(m, n)$ were checked with the SP method.
1353 The results of $SC(m, n)$ and $NSC(m, n)$ with different minimum p_T cuts are shown
1354 in Fig.4.15(up to 0.7 GeV/c minimum p_T cuts) and Fig.4.16(up to 1.5 GeV/c) min-
1355 imum p_T cuts. As seen in Fig.4.15, there is certain p_T dependence for $SC(m, n)$, but
1356 not clear p_T dependence for $NSC(m, n)$ as like QC method. However, in even higher
1357 p_T region(Fig.4.16), unlike the results with QC methods, we could see weak p_T depen-
1358 dence in $NSC(m, n)$. In the $SC(m, n)$ results, as the minimum p_T cuts goes higher, the
1359 strength of the correlation becomes stronger in both $SC(3, 2)$ and $SC(4, 2)$. However,
1360 in $NSC(m, n)$ with the SP method, when the minimum p_T cuts increase, the strength
1361 of correlation for $NSC(3, 2)$ is (negatively) stronger, but the strength of correlation of
1362 $NSC(4, 2)$ becomes weaker. As a result, in higher p_T range, the $NSC(m, n)$ values
1363 always getting smaller.

1364 For the better comparison, the ratio of $NSC(m, n)$ with various minimum p_T cuts
1365 to default is shown in Fig.4.17. Up to 0.7 GeV/c, the ratio of $NSC(m, n)$ values are
1366 consistent with a default cut within errors, but the minimum p_T exceeds 0.8GeV/c, the
1367 ratio of $NSC(3, 2)$ moving above the 1, and the ratio of $NSC(4, 2)$ goes down below
1368 the 1. The reason why these trends are only shown in the SP method, and not in the
1369 QC is not yet fully explained. However, the disadvantage of the SP method is that we
1370 lose almost half of the statistics because of a large η gap around $\eta = 0$ and also the
1371 number of combinations for the track pair is $\frac{1}{3}$ when compared to QC methods. This is
1372 one possible option to explain these p_T dependence behavior of SP method, and tested
1373 in ToyMC simulation in Appendix A.

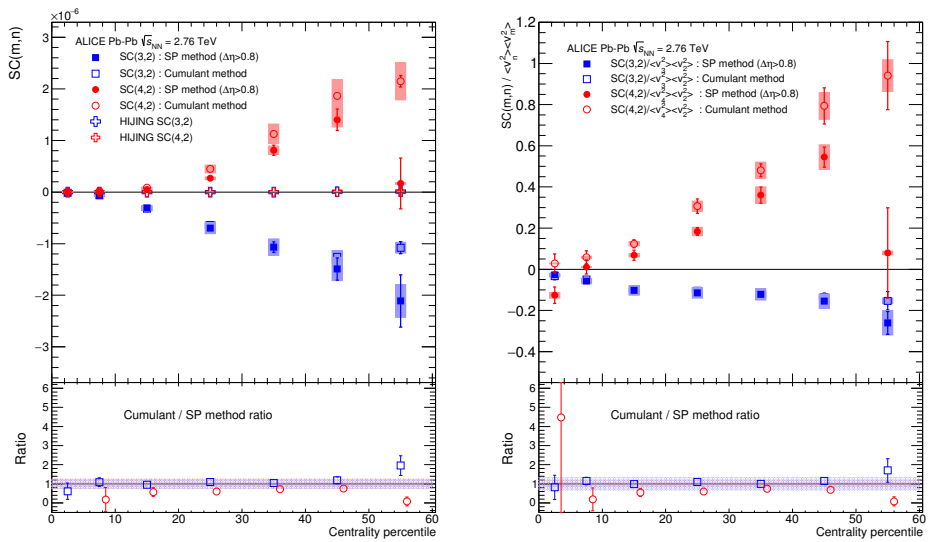


Figure 4.13: Comparison of $SC(m,n)$ (Top) and $NSC(m,n)$ (Bottom) results for $SC(3,2)$ (blue) and $SC(4,2)$ (red) with the SP and QC method up to 60% centralities. The different ratios are shown in lower pads, and systematic uncertainty is drawn as a band around 1

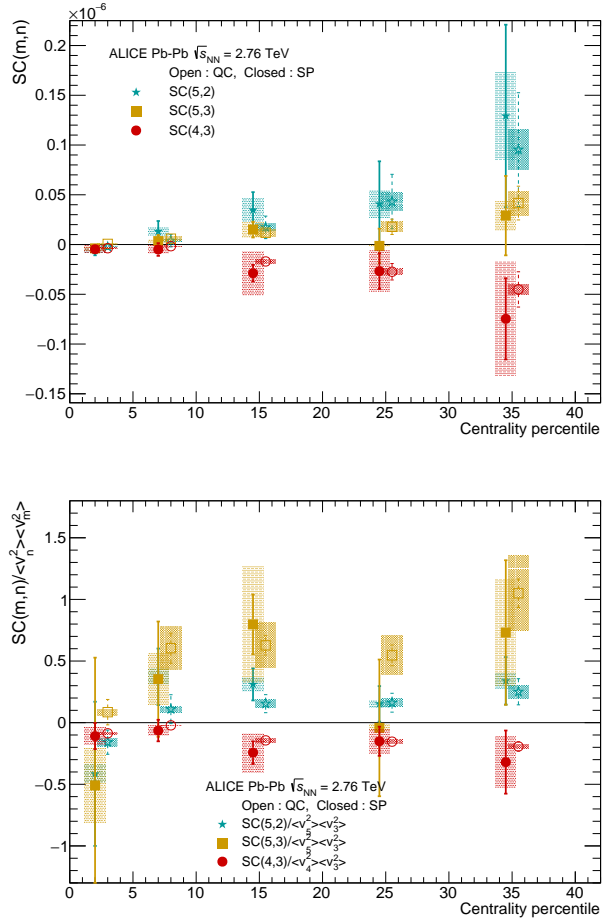


Figure 4.14: Result of higher order $SC(m, n)$ and $NSC(m, n)$ with two different method. Along x-axis offset was applied for better visibility. For the QC method $|\eta| < 0.8$ cut was applied, while SP method takes $0.4 < |\eta| < 0.8$.

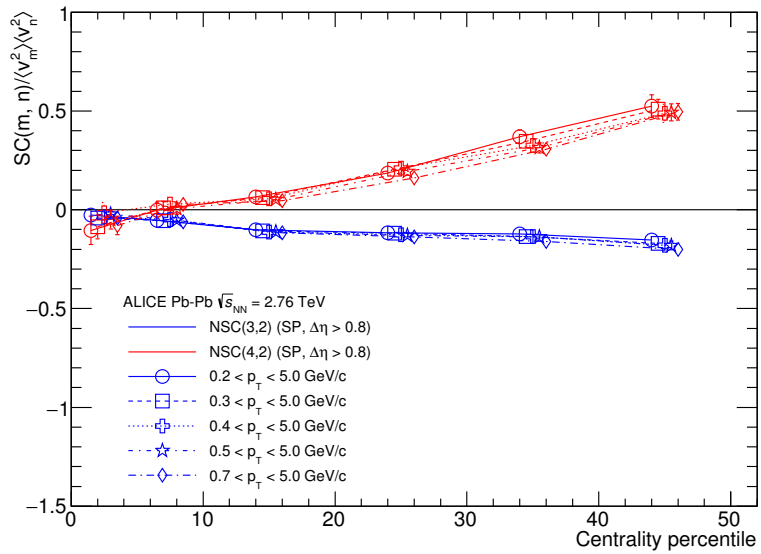
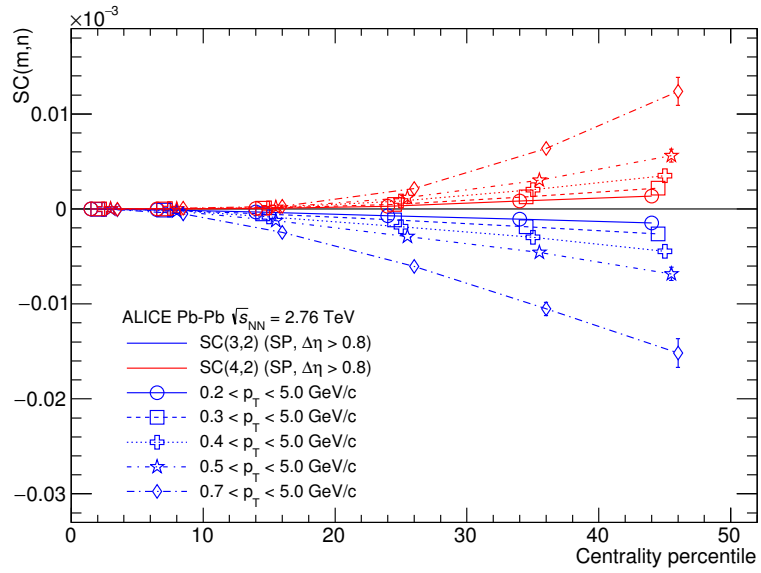


Figure 4.15: $SC(m, n)$ and $NSC(m, n)$ with SP method with default cuts ($0.2 \leq p_T \leq 5.0 \text{ GeV}/c$) and various minimum p_T cuts up to $0.7 \text{ GeV}/c$

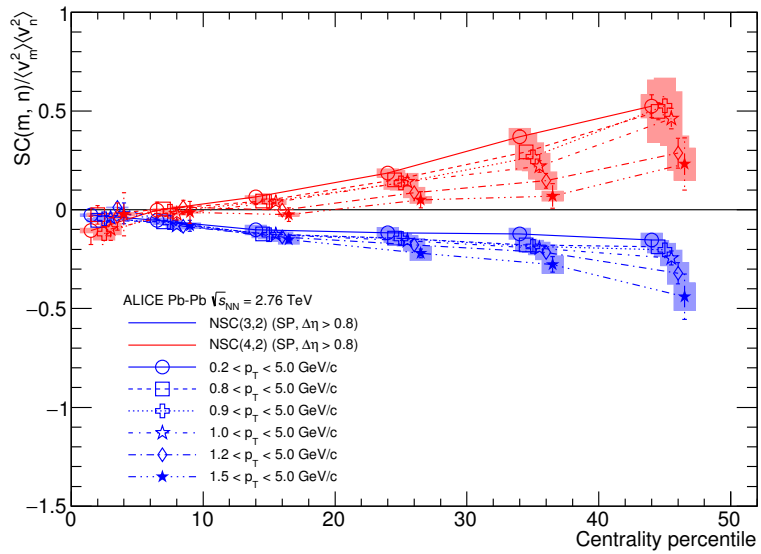
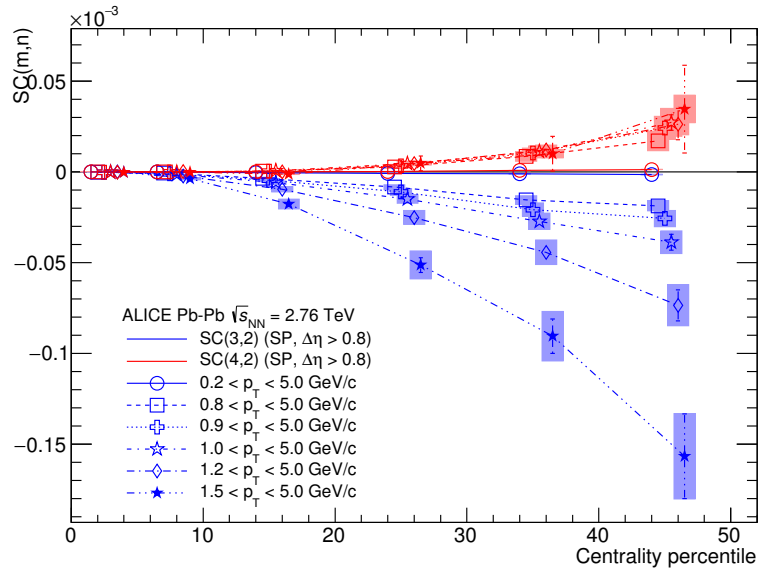


Figure 4.16: $SC(m, n)$ and $NSC(m, n)$ with SP method with default cuts ($0.2 \leq p_T \leq 5.0$ GeV/c) and various minimum p_T cuts up to 1.5 GeV/c)

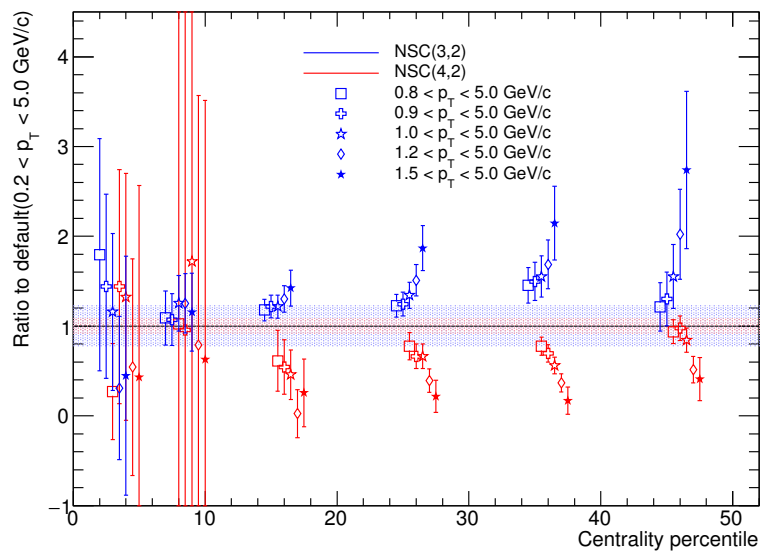
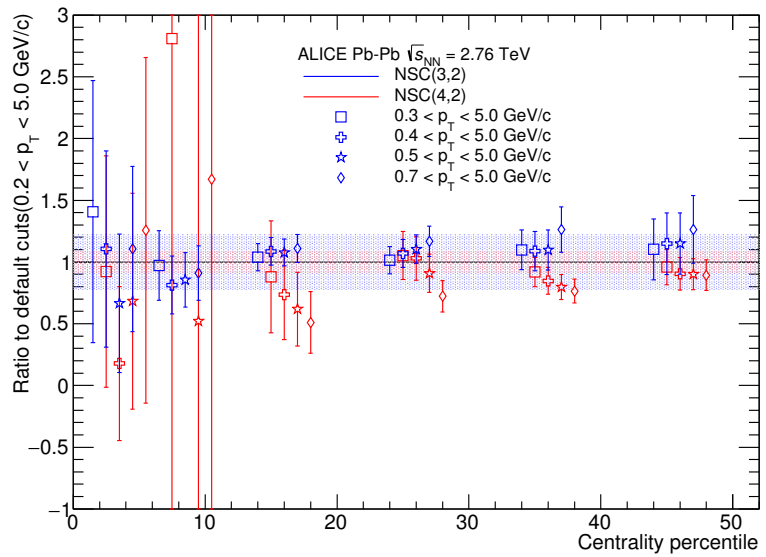


Figure 4.17: The ratio of $NSC(m, n)$ with SP method to the default cuts

₁₃₇₄ **Chapter 5**

₁₃₇₅ **Conclusion and Outlook**

₁₃₇₆ As the strong evidence of QGP existence, flow has been studied in detail during the
₁₃₇₇ past few decades. But only a few studies have been done about correlation between flow
₁₃₇₈ harmonics and leads to the following questions; How do v_n and ϵ_n fluctuate and what
₁₃₇₉ is the underlying probability density function (*p.d.f*) of their distributions? How are the
₁₃₈₀ initial geometry fluctuations reflected in differential flow measurements? What is the
₁₃₈₁ relationship between different harmonic event plane angles? What is the relationship
₁₃₈₂ between the flow coefficient of different harmonics? The answers to the above questions
₁₃₈₃ (especially for the last) *Symmetric Cumulants* ($SC(m, n)$) have been introduced as the
₁₃₈₄ key observable to measure correlation between flow harmonic “magnitudes” v_m and v_n .

₁₃₈₅ As the result of $SC(m, n)$, we have found that event-by-event fluctuations of v_2 - v_3
₁₃₈₆ and v_3 - v_4 are anti-correlated while fluctuations of v_2 - v_4 , v_2 - v_5 and v_3 - v_5 are correlated.
₁₃₈₇ The various hydrodynamic calculations and model simulations were studied together.
₁₃₈₈ The large differences between data and MC-Glauber confirmed that the correlation were
₁₃₈₉ not able to explained by only linear response of initial conditions, and there is certain
₁₃₉₀ non-linear contribution of initial fluctuations.

₁₃₉₁ None of the existing models and hydrodynamic calculations with the different pa-
₁₃₉₂ rameterizations of the temperature dependence of η/s couldn't capture the data quantita-
₁₃₉₃ tively. Furthermore, the sign of v_3 - v_2 correlation in most central collision range(0-10%)
₁₃₉₄ was found to be different between the data and hydrodynamic model calculations. In the
₁₃₉₅ most central collisions the anisotropies originate mainly from fluctuations, i.e. the ini-

1396 tial ellipsoidal geometry characteristic for mid-central collisions plays little role in this
1397 regime. Hence this observation might help to understand the details of the fluctuations
1398 in initial conditions.

1399 It is suggested that the $SC(m, n)$ is more sensitive to both initial conditions and hy-
1400 drodynamic property η/s than single flows. In addition, we have found that the different
1401 order harmonic correlations have different sensitivities to the initial conditions and the
1402 system properties. Therefore they have discriminating power on separating the role of
1403 the η/s from the initial conditions to the final state particle anisotropies.

1404 The comparisons to VISH2+1 calculation show that all the models with large η/s
1405 regardless of the initial conditions failed to capture the centrality dependence of higher
1406 order correlations, more clearly than lower order harmonic correlations. Based on the
1407 tested model parameters, the η/s should be small and AMPT initial condition is favored
1408 by the data. A quite clear separation of the correlation strength between different initial
1409 conditions is observed for these higher order harmonic correlations compared to the
1410 lower order harmonic correlations.

1411 We have found that v_3-v_2 and v_4-v_2 correlations have moderate p_T dependence in
1412 mid-central collisions. This might be an indication of possible viscous corrections for
1413 the equilibrium distribution at hadronic freeze-out. The results presented in this article
1414 can be used to further optimize model parameters and put better constraints on the initial
1415 conditions and the transport properties of nuclear matter in ultra-relativistic heavy-ion
1416 collisions.

1417 All these $SC(m, n)$ results were measured with multi particle cumulants method
1418 (QC method). Besides of QC method, we introduced the Scalar Product method (SP
1419 method) to measure $SC(m, n)$. Basically, most of the results are consistent in errors.
1420 With the current understanding of the methods, they should agree well even though they
1421 have different sensitivity to the flow fluctuations. However at some points, there are some
1422 deviations between the SP and QC methods. These differences are most pronounced in
1423 peripheral collision centrality regions. We investigate the reason of difference between
1424 two methods by testing and measuring $SC(m, n)$ by using a simple toy monte-carlo.
1425 We tested the flow fluctuations and non-flow effect, and found that at some multiplicity

range SP method were not able to recover input values. The different sensitivities to flow fluctuations and non-flow effect in QC and SP methods might be a nice piece of material by itself in further study.

Even though, there are some missing parts on this analysis, such as no clear p_T dependence of $NSC(m, n)$ and lack of explanation for different method response, it provides quantitative hints for the comprehensive understanding of hydrodynamical behavior of collision system. Also new observables $SC(m, n)$ are promising observables to provide additional constraints on the initial state phenomena and dynamical evolution and its fluctuation without event-by-event shape engineering. Since Run2 data from LHC is approaching with a new highest record of center-of-mass energy and much higher amount of events. Since the flow analysis were based on statistical calculation, more interesting analysis including correlations and fluctuations will be studied again with Run2 data.

Appendices

1440 **Appendix A**

1441 **Toy MC simulation**

1442 **A.0.1 Toy Monte Carlo simulation**

1443 In this appendix, we will use the Monte Carlo simulation to check the correlation be-
1444 tween two different flow harmonics and check the systematic response to Q -Cumulant
1445 method(QC) and Scalar Product method(SP).

Since, $SC(m, n)$ is defined as like

$$\langle v_n^2 v_m^2 \rangle - \langle v_n^2 \rangle \langle v_m^2 \rangle$$

1446 it is not easy to calculate directly $SC(m, n)$ from arbitrary v_n and v_m which fluctuate
1447 event by event. So, in this Toy Monte Carlo simulation, we consider simplest case. i.e
1448 the uniform flow distribution. The uniform flow distribution is defined as like

$$f(v_n) = const, \quad v_{min} < v_n < v_{max} \quad (\text{A.1})$$

1449 In this configuration, we can easily assume that the function of flow v_n can be nor-
1450 malized with

$$1 = \int_{-\infty}^{\infty} f(v_n) dv \quad (\text{A.2})$$

$$= \int_{v_{min}}^{v_{max}} const dv \quad (\text{A.3})$$

$$= cont(v_{max} - v_{min}) \quad (\text{A.4})$$

1451 SO,

$$const = \frac{1}{v_{max} - v_{min}} \quad (A.5)$$

1452

1453 Then the final normalized uniform flow distribution is

$$f(v_n) = \frac{1}{v_{max} - v_{min}} \quad (A.6)$$

1454

1455 And if we assume the mean value of given order flow harmonics as μ_v , then it follows

$$1 = \int_{-\infty}^{\infty} vf(v)dv \quad (A.7)$$

$$= \int_{v_{min}}^{v_{max}} v \frac{1}{v_{max} - v_{min}} dv \quad (A.8)$$

$$= \frac{1}{v_{max} - v_{min}} \frac{v_{max}^2 - v_{min}^2}{2} \quad (A.9)$$

1456 and finally we have

$$\mu_v = \frac{v_{max} - v_{min}}{2} \quad (A.10)$$

1457

1458 To calculate standard deviation(σ_v) for event fluctuations, use the definition of
1459 expectation value of a random variables.

$$\mu_x = E[x] = \int_{-\infty}^{\infty} xf(x)dx \quad (A.11)$$

1460

$$\sigma_x^2 = V[x] = E[(x - E[x])^2] = \int_{-\infty}^{\infty} (x - \mu_x)^2 f(x)dx \quad (A.12)$$

1461

1462 So, we can get straightforwardly

$$\sigma_v^2 = \frac{1}{12} (v_{max} - v_{min})^2 \quad (A.13)$$

1463 or,

$$\sigma_v = \frac{1}{2\sqrt{3}}(v_{max} - v_{min}) \quad (\text{A.14})$$

1464

1465 So, for the uniform distribution Toy models, we can express the flow v_n and its
1466 fluctuation with events(σ_v) as term as uniform flow distribution (v_{max} and v_{min})

$$\langle v \rangle = \frac{v_{max} + v_{min}}{2} \quad (\text{A.15})$$

1467

$$\langle v^2 \rangle = \frac{v_{max}^2 + v_{max}v_{min} + v_{min}^2}{3} \quad (\text{A.16})$$

1468

$$\langle v^3 \rangle = \frac{1}{4}(v_{max} + v_{min})(v_{max}^2 + v_{min}^2) \quad (\text{A.17})$$

1469

$$\langle v^4 \rangle = \frac{1}{5}(v_{max}^4 + v_{max}^3 v_{min} + v_{max}^2 v_{min}^2 + v_{max} v_{min}^3 + v_{min}^4) \quad (\text{A.18})$$

1470

1471 With above equations, we now can express the $SC(m, n)$ as term of v_{max} and v_{min}
1472 only. For example, if we set v_2 and v_3 to have uniform distribution such as

1473 • $v_2 = \text{Uniform}[0.05, 0.08]$

1474 • $v_3 = 0.1 - v_2$

1475 then the $SC(3, 2)$ will be express as like

$$SC(3, 2) = \langle v_3^2 v_2^2 \rangle - \langle v_3^2 \rangle \langle v_2^2 \rangle \quad (\text{A.19})$$

$$= \langle x^2 (0.1 - x)^2 \rangle - \langle x^2 \rangle \langle (0.1 - x)^2 \rangle \quad (\text{A.20})$$

$$= \langle x^2 (0.01 - 0.2x + x^2) \rangle - \langle x^2 \rangle \langle (0.01 - 0.2x + x^2) \rangle \quad (\text{A.21})$$

$$= \langle 0.01x^2 \rangle - \langle 0.2x^3 \rangle + \langle x^4 \rangle - \langle x^2 \rangle (0.01 - \langle 0.2x \rangle + \langle x^2 \rangle) \quad (\text{A.22})$$

$$= -(0.2) \langle x^3 \rangle + \langle x^4 \rangle + 0.2 \langle x \rangle \langle x^2 \rangle - \langle x^2 \rangle^2 \quad (\text{A.23})$$

$$\begin{aligned} &= -(0.2) \frac{1}{4} (v_{max} + v_{min})(v_{max}^2 + v_{min}^2) \\ &\quad + \frac{1}{5} (v_{max}^4 + v_{max}^3 v_{min} + v_{max}^2 v_{min}^2 + v_{max} v_{min}^3 + v_{min}^4) \\ &\quad 0.2 \frac{v_{max}^2 + v_{max} v_{min} + v_{min}^2}{3} \frac{v_{max} + v_{min}}{2} \\ &\quad - \frac{v_{max}^2 + v_{max} v_{min} + v_{min}^2}{3} \frac{v_{max}^2 + v_{max} v_{min} + v_{min}^2}{3} \quad (\text{A.24}) \end{aligned}$$

1476 As a results $SC(3, 2) \simeq -6.78 \times 10^{-7}$, Also $SC(4, 2)$ can be obtained by similar
1477 calculations.

1478 In this analysis, we tested with ToyMC simulation for $SC(m, n)$ with both uniform
1479 fluctuation case (which is simplest case), and 2-Dim Gaussian fluctuation case (which is
1480 more realistic case) For the uniform fluctuation case, we set v_n as like

1481 • $v_2 = \text{Uniform}[0.04, 0.09]$

1482 • $v_3 = 0.1 - v_2$

1483 • $v_4 = v_2 - 0.02$

1484 These settings are based on the real flow measurements to have $\langle v_2 \rangle \sim 0.065$ which
1485 is similar v_2 in mid-central collisions, and setting v_3 to have negative correlation with
1486 similar as what it is measured. Also v_4 have been setted to have positive correlation but
1487 a little bit higher than what is measured.

1488 We performed ToyMC simulations with various multiplicity and run over 1M events
1489 per each multiplicity bins. The results are shown in Fig.A.2 and A.3. As seen in results,
1490 both Q-cumulants (QC) and Scalar Product (SP) method were able to capture input value

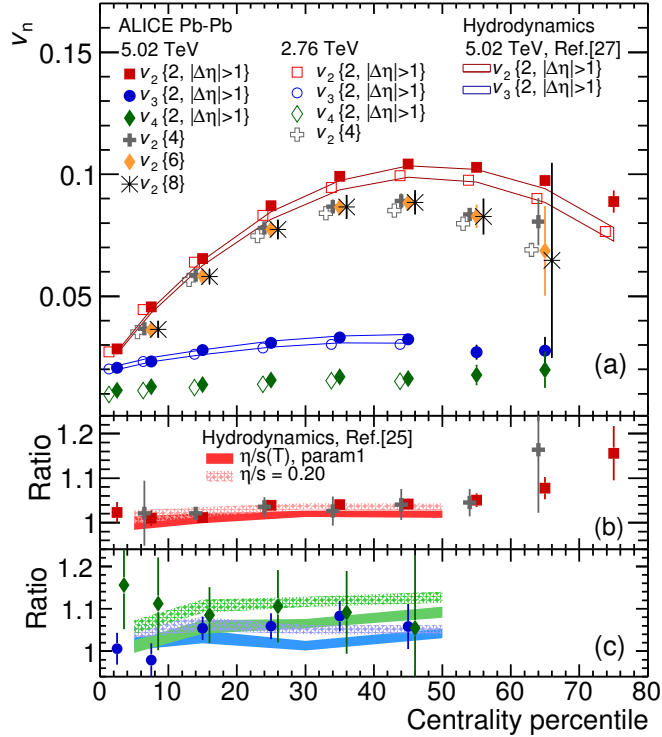


Figure A.1: Flow measurement with ALICE at $\sqrt{S_{NN}} = 2.76\text{TeV}/c$ and $5.02\text{TeV}/c$ with various measurement methods, also hydrodynamic predictions are drawn as bands

in high multiplicity regions with $\sim 1\%$ errors, but in low multiplicity region, we observe discrepancy between two methods and these effects are most pronounced in lowest multiplicity (corresponding to values for peripheral collisions over 60% centrality). Neither QC nor SP methods were fully free from these effects. However, because of η gap, SP method has disadvantages for the number of combinations(or multiplicity). As the result, QC methods recover better the input value than SP method, and SP method results are always smaller than QC for all multiplicity bins.

Also we tested with 2-dim Gaussian like flow fluctuations to try a realistic flow fluctuation taken from a measured distribution.

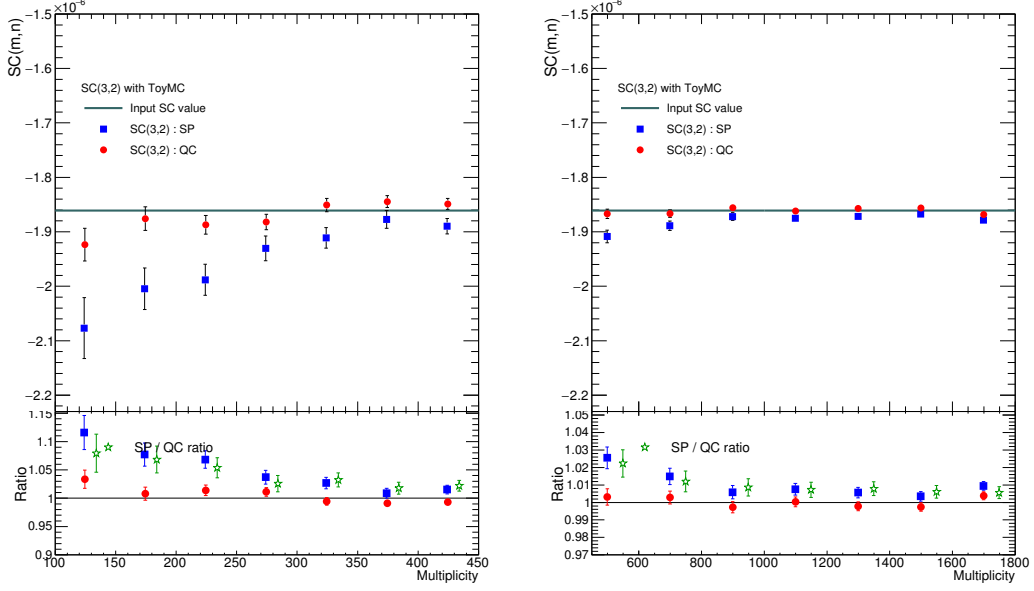


Figure A.2: Results of ToyMC simulation for SC(3,2) with random uniform distribution of v_n with various multiplicity. The left figure is the result from 50 to 450 multiplicity, and right figure is the result from 500 to 1800 multiplicity. Both Q-cumulatns(QC) and Scalar Product(SP) mehtods are tested and drawn with red and blue color marker. Also ratio to input values are drawn in bottom pad, and the ratio of SP / QC methods are drawn with green marker

$$p(v_n) = \frac{v_n}{\sigma^2} e^{-\frac{v_n^2}{2\sigma^2}}, \quad (\text{A.25})$$

1500 This is the radial projection of a 2 dimensional Gaussian distribution in \bar{v}_n . The σ
 1501 parameter is given by $\sigma = \sqrt{2/\pi} \langle v_n \rangle$
 1502 then the settings are as like followings

- 1503 • v_2 = Bessel Gaussian (mean 0.065)
 1504 • $v_3 = 0.04 - (v_2/8)$
 1505 • $v_4 = v_2/6$

1506 We set v_n to have similar values in real flow values and to have $\sim SC(m, n)$ in
 1507 mid centralities in ALICE data. The results are shown in Fig.A.5. As same as uniform

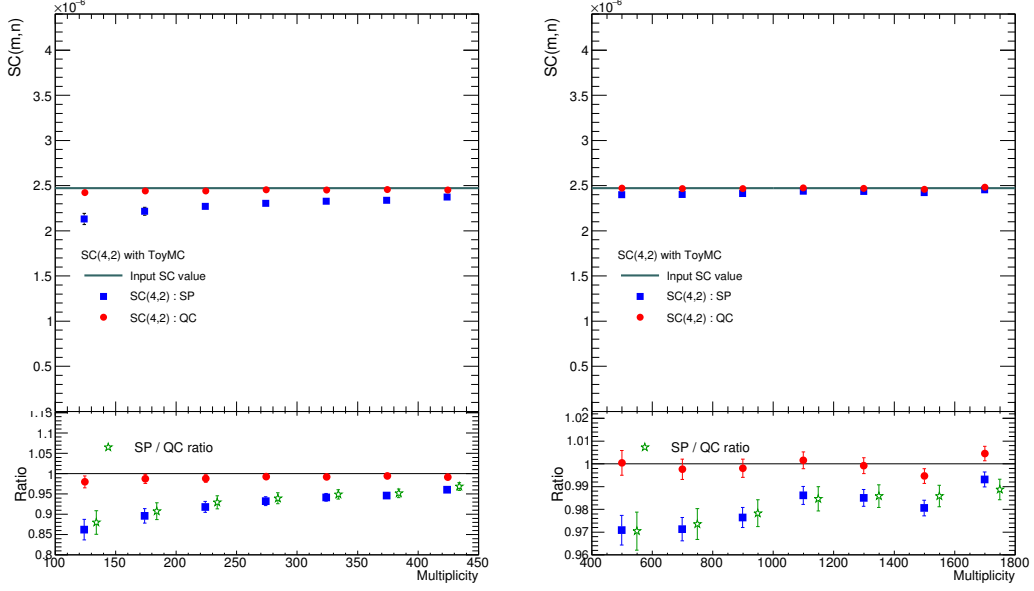


Figure A.3: Results of ToyMC simulation for $SC(4,2)$ with random uniform distribution of v_n with various multiplicity. The left figure is the result from 50 to 450 multiplicity, and right figure is the result from 500 to 1800 multiplicity. Both Q-cumulatns(QC) and Scalar Product(SP) mehtods are tested and drawn with red and blue color marker. Also ratio to input values are drawn in bottom pad, and the ratio of SP / QC methods are drawn with green marker

1508 flow distribution case both method recover input values well and consistent in 1% levels.
 1509 However when we see the details, we can check that the results from SP methods are
 1510 always lower than QC methods as like previous results. As the results, the ratio of SP
 1511 over QC results are above 1 in $SC(3, 2)$ case because it' is negative correlation. And
 1512 ratio of SP over QC are below than 1 in $SC(4, 2)$ case.

1513 A.0.2 Test non-flow effects by impose jets from PYTHIA into ToyMC

1514 $SC(m, n)$ results with HIJING are zero for all centralities for both methods, and
 1515 also even with the high p_T bins. These suggested that $SC(m, n)$ is not the results from
 1516 non-flow effects, and it is not sensitive to non-flows. In additional to HIJING results,
 1517 we now have studied it explicitly with PYTHIA jet particles on $SC(m, n)$. This implies

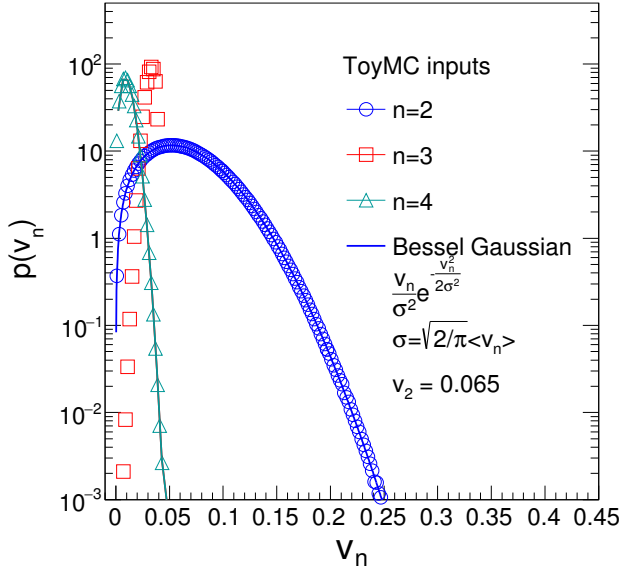


Figure A.4: Event by Event Flow harmonics distributions from Bessel Gaussian function based on [?]

1518 the largest effect from the particles which stem from jets in PYTHIA in mid central col-
 1519 lisions. To check these study, we setup ToyMC as previous section. And use PYTHIA8
 1520 to impose jet into ToyMC. To see the maximized effects on $SC(m, n)$ we use PYTHIA
 1521 setting as like followings

- 1522 • $\sqrt{S_{NN}} = 2.76 \text{ TeV}$
- 1523 • Phase Space $p_T > 5 \text{ GeV}/c$
- 1524 • Other settings use default of PYTHIA8

1525 and implement jet particles for every events. The p_T spectra and it's ratio to number of
 1526 particles in corresponding centralities are drawn in Figure. A.6. Straitforwadly the jet
 1527 effects are most pronounced in peripheral collisions and p_T regions more than $1 \text{ GeV}/c$
 1528 The results of $SC(m, n)$ with ToyMC with jets from PYTHIA is shown in Fig.A.7.
 1529 When we do not implement the PYTHIA Jet, as we expected, the results of SC(m,n)

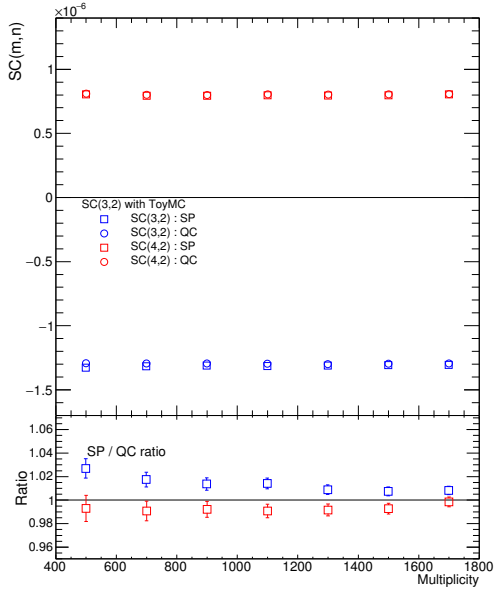


Figure A.5: Results of ToyMC simulation for $SC(m,n)$ with Bessel Gaussian like distribution, Both SP and QC results were performed and the ratio of two different methods are show in bottom pad

well capture the input values with around few % of differences. Also as we saw in previous section, $SC(m, n)$ with QC results have better accuracy than SP method. When we embed PYTHIA jet into ToyMC the both SP and QC results are suffer from the jet and, the strength of correlation from both methods are getting smaller. The response to particles from jet are quite similar for both QC and SP methods. There are few % of difference in central collisions and around 10% effect in 50% ~ 60% centrality bin and these observations hold both for $SC(3, 2)$ and $SC(4, 2)$. When we consider that these PYTHIA settings are almost maximized non-flow effects, and the behavior of both SP and QC response are same, we can conclude that the $SC(m,n)$ is insensitive to Non-flow effects.

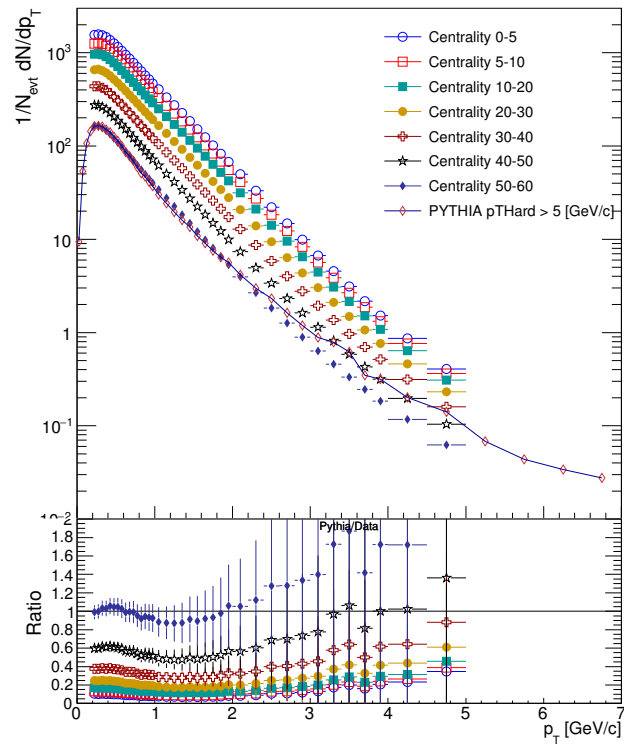


Figure A.6:

1540

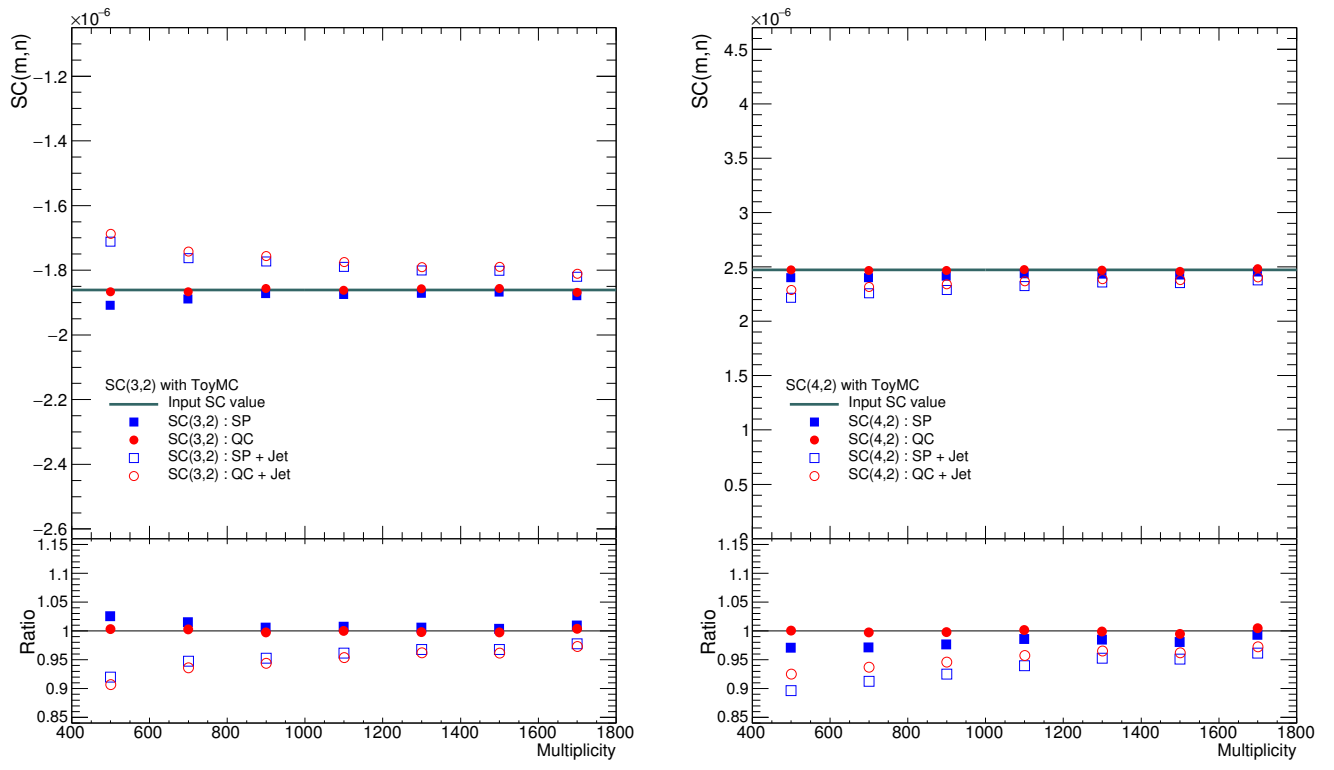


Figure A.7: The ToyMC results of $SC(3,2)$ (left) and $SC(4,2)$ (right) from 400 to 1800 multiplicity. The input values are drawn as green line. Closed markers are the results with SP and QC results without jet implementation(as same as previous results) and open markers are the results after PYTHIA jet embedding. The ratio to the input values are drawn in bottom pad

₁₅₄₁ **Appendix B**

₁₅₄₂ **Choosing weight for event average**

₁₅₄₃ The double angular brackets in flow analysis means usually means that one for aver-
₁₅₄₄ age over all particles, and the other for the average over all events.

$$\langle\langle \dots \rangle\rangle = \langle\langle \dots \rangle_{particles} \rangle_{events}$$

₁₅₄₅ And for the average over events, the finding proper event weights are important to
₁₅₄₆ get the results without bias.

₁₅₄₇ One approach to get event averaged results, is set the all event weights as 1 (equal
₁₅₄₈ weights). For example, measure the flow coefficient(v_n) in given centrality, we measure
₁₅₄₉ v_n for each events, and calculate mean v_n as average of measured v_n with uniform
₁₅₅₀ weights(or materially no weights). But this approach is not correct in case of multi-
₁₅₅₁ particle correlations.

₁₅₅₂ In this analysis of $SC(m, n)$, the measurement performed in two procedure, first
₁₅₅₃ over all distinct particle quadruplets in an event, and then in the second step the single-
₁₅₅₄ event averages were weighted with "number of combinations" for correct event weight.

₁₅₅₅ To prove this, let's think a set of N events, where the multiplicity of each event is M_i
₁₅₅₆ where the i denote for i th event.

₁₅₅₇ Then the equation for 2-particle correlation Eq.3.3 can be written as like

$$\langle\langle 2 \rangle\rangle \equiv \frac{\sum_{i=1}^N \sum_{a,b=1}^{M_i} e^{in(\phi_{i,a} - \phi_{i,b})}}{\sum_{i=1}^N \sum_{a,b=1}^{M_i}} \quad (\text{B.1})$$

1558 with the constraints $a \neq b$. The equation B.1 implies that, we calculated every possi-
 1559 ble pairs of particle in an events and by using constraints, we eliminated all contributions
 1560 from self-correlations. If we take two distinct pairs of particles, one formed in event A
 1561 and another formed in event B, then the above definition ensures that these two distinct
 1562 pairs of particles will be taken into account at equal footing (i.e. a unit weight has being
 1563 assigned to each distinct pair of particles in any event in Eq.B.1). The denominator in
 1564 definition simply constant the total number of all such distinct pairs in all events. In
 1565 general form, for the definition of the i th event

$$\langle 2 \rangle_i \equiv \frac{\sum_{a,b=1}^{M_i} e^{in(\phi_{i,a} - \phi_{i,b})}}{\sum_{a,b=1}^{M_i}} \quad (\text{B.2})$$

1566

1567 And the total number the distinct pairs in the i th events will be evaluated as follows

$$\sum_{a,b=1}^{M_i} = \left(\sum_{a=1}^{M_i} \right) \left(\sum_{b=1}^{M_i} \right) - \sum_{a=b=1}^{M_i} = M_i^2 - M_i = M_i(M_i - 1) \quad (\text{B.3})$$

1568

1569 Extend to all event sets,

$$\langle\langle 2 \rangle\rangle = \frac{\sum_{i=1}^N \sum_{a,b=1}^{M_i} e^{in(\phi_{i,a} - \phi_{i,b})}}{\sum_{i=1}^N M_i(M_i - 1)} \quad (\text{B.4})$$

1570 and

$$\langle 2 \rangle_i \equiv \frac{\sum_{a,b=1}^{M_i} e^{in(\phi_{i,a} - \phi_{i,b})}}{M_i(M_i - 1)} \quad (\text{B.5})$$

1571 Then, we immediately get the following results by insert above equation to the orig-
 1572 inal Eq. B.1

$$\langle\langle 2 \rangle\rangle = \frac{\sum_{i=1}^N M_i(M_i - 1) \times \frac{\sum_{a,b=1}^{M_i} e^{in(\phi_{i,a} - \phi_{i,b})}}{M_i(M_i - 1)}}{\sum_{i=1}^N M_i(M_i - 1)} \quad (\text{B.6})$$

1573 and finally we get,

$$\langle\langle 2 \rangle\rangle = \frac{\sum_{i=1}^N M_i(M_i - 1) \times \langle 2 \rangle_i}{\sum_{i=1}^N M_i(M_i - 1)} \quad (\text{B.7})$$

1574 As seen in Eq. B.7, the event weight number of combinations has to be used to
1575 weight single event average $\langle 2 \rangle$ to obtain exactly the all event average $\langle\langle 2 \rangle\rangle$. The prof of
1576 4-particle correlation can be done in similar way.

₁₅₇₇ **Appendix C**

₁₅₇₈ **Jet energy loss as function of
₁₅₇₉ path-length**

₁₅₈₀ **C.1 Basic motivation**

₁₅₈₁ The nuclear modification factor, which is called R_{AA} , is one of the strong evidence
₁₅₈₂ of created medium in heavy ion collisions compare to $p+p$ collisions [136]. In Quantum
₁₅₈₃ Chromodynamics(QCD), the suppression of high p_T hadrons was predicted as the result
₁₅₈₄ of the energy loss of hard-scatters quarks and gluons in the hot and dense medium.

₁₅₈₅ **C.2 Analysis**

₁₅₈₆ **C.2.1 Inclusive R_{AA}**

₁₅₈₇ To compare heavy ion collisions to $p-p$ collision, the nuclear modification factor
₁₅₈₈ R_{AA} is defined.

$$R_{AA}(p_T) = \frac{(1/N_{AA}^{evt})dN^{AA}/dp_T}{\langle N_{coll} \rangle (1/N_{pp}^{evt})dN^{pp}/dp_T} \quad (\text{C.1})$$

₁₅₈₉

₁₅₉₀ where dN^{AA}/dp_T and dN^{pp}/dp_T are the yields in heavy ion collisions and $p-p$ col-
₁₅₉₁ lisions, respectively. $\langle N_{coll} \rangle$ is the average number of binary nucleon-nucleon collisions
₁₅₉₂ in one heavy ion collision event.

₁₅₉₃ Without medium effect, the nuclear modification factor R_{AA} should be 1. However,

1594 in heavy ion collision the nuclear modification factor is usually smaller than 1 [8, 52, 53].
 1595 These suppression for the high p_T hadrons can be explained by “jet quenching”, and this
 1596 is the one of probe for the existence of QGP medium. Compare with RHIC, LHC show
 1597 a stronger modification [8]. This indicate an enhanced energy loss and hence a denser
 1598 medium was produced at the LHC.

1599 C.2.2 Elliptic flow

1600 Anisotropic flow is the well known feature in both theoretical and experiment in
 1601 heavy ion collision. It provides the hints to understand collision evolution and thermal-
 1602 ization process. (See section.1.4 for the details)

$$\frac{dN}{d\Delta\phi} = \frac{x_0}{2\pi} + \frac{1}{2\pi} \sum_{n=1} (2v_n \cos n(\phi - \psi_n)) \quad (\text{C.2})$$

1603

1604 The function of $\frac{dN}{d\Delta\phi}$ shows the particle distribution in transverse direction. This
 1605 anisotropy particle production is known as flow effect. Especially, elliptical flow, which
 1606 is second order flow v_2 is well explained by almond shape initial geometry. But the
 1607 shape of the collision geometry is not a perfect almond shape because the collision nu-
 1608 cleon is not uniform sphere. Therefore, the created medium is not homogenous and has
 1609 complex shape. These are the reason of flow fluctuation and cause of higher order flow.
 1610 This higher order flow which comes from fluctuation and is not strongly affected by the
 1611 centrality of the collision. Because the distribution of the participating nucleons in col-
 1612 lision is totally random, so fluctuation is depends on event by event geometry and these
 1613 effect will be minimized in average over events.

1614 C.2.3 R_{AA} as function of $\Delta\phi$

As the nuclear modification factor represent the ratio of yield of particle produced in heavy ion and p - p collision, one can make R_{AA} as a function of p_T and $\Delta\phi$, where

$$\Delta\phi = \phi - \psi_n$$

1615 by using definition of flow. Since, the yield of p - p collision does not have reaction
 1616 plane, we can estimate the ratio of particle produced in ϕ angle is uniform over the event

₁₆₁₇ average. Therefore, the definition of R_{AA} as function of p_T and $\Delta\phi$ can be written as
₁₆₁₈ [137, 138]

$$R_{AA}(p_T, \Delta\phi) = \frac{(1/N_{AA}^{evt})d^2N^{AA}/dp_T d\Delta\phi}{\langle N_{coll} \rangle (1/N_{pp}^{evt})dN^{pp}/dp_T} \quad (\text{C.3})$$

$$= R_{AA}(p_T) \frac{dN^{AA}}{d\Delta\phi} \quad (\text{C.4})$$

$$= R_{AA}(p_T)(1 + \sum_{n=1} (2v_n \cos n(\Delta\phi))) \quad (\text{C.5})$$

₁₆₁₉

₁₆₂₀ If we neglect high order flow which comes from fluctuations, above equation can be
₁₆₂₁ simplified like

$$R_{AA}(p_T, \Delta\phi) \sim R_{AA}(p_T)(1 + 2v_2 \cos 2\Delta\phi) \quad (\text{C.6})$$

₁₆₂₂

₁₆₂₃ C.2.4 Path-length calculation with Glauber model

₁₆₂₄ If we assume all particles are produced from the center of collision region, then it
₁₆₂₅ is possible to represent path-length as function of centrality and $\Delta\phi$ which is transverse
₁₆₂₆ angle with respect to the reaction plane. To analyze the path-length dependence of R_{AA} ,
₁₆₂₇ we estimate the path lengths of patrons in the medium as the distance from the center
₁₆₂₈ to the edge of the elliptical overlap zone of the heavy ion collision(See Fig.C.1). To
₁₆₂₉ calculate this length, TGlauber Monte Carlo simulation has been used to evaluate for all
₁₆₃₀ variations as function of impact parameter(centrality). of medium to the edge.

₁₆₃₁ However, in real situation, hard scattering happens in any collision point, also the
₁₆₃₂ direction where the parton travels is random. One would calculate a weight factor for
₁₆₃₃ the parton to travels into the divided region we set. In this case, proper path length is the
₁₆₃₄ average value of length from the collision points to the edge of collision region for given
₁₆₃₅ angle, such as

$$L(\Delta\phi) = \frac{\sum_{n=1}^N L_n(\Delta\phi)}{N} \quad (\text{C.7})$$

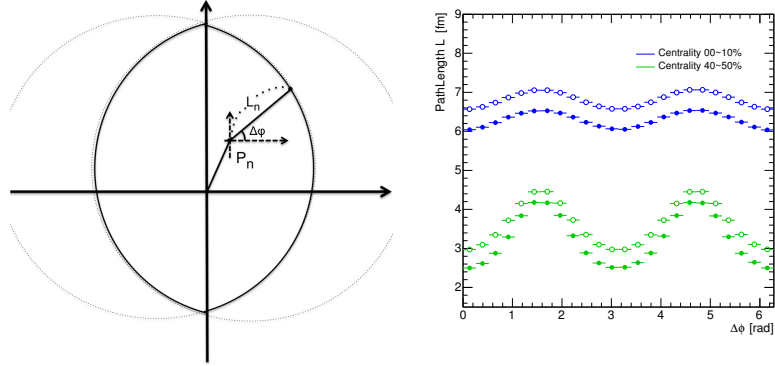


Figure C.1: Basic concept of definition of path-length for given angle $\Delta\phi$ (top), and results for centrality 00-10% and 40-50%(bottom). Open symbols are path-length which is calculated from Eq.C.7. Closed symbols are length from center to edge of region.

1636 where N is number of binary collisions, and $L_n(\Delta\phi)$ is length from n_{th} collision point(P_n
 1637 in Fig.C.1) to edge of collision shape for given angle $\Delta\phi$. This length is always longer
 1638 then length from center to edge of collision region.

1639 C.3 Result

1640 C.3.1 $R_{AA}(p_T, \Delta\phi)$

1641 For LHC experiment, the Nuclear modification factor, R_{AA} , of the Pb-Pb values
 1642 has been published by ALICE collaboration[139]. In Central collisions the field is most
 1643 suppressed with $R_{AA} \sim 0.13$ at $p_T = 6 \sim 7 \text{ GeV}/c$. Above $p_T > 7 \text{ GeV}/c$, there is
 1644 a significant rise in the nuclear modification factor for $p_T > 30 \text{ GeV}/c$. In peripheral
 1645 collisions, the suppression is weaker with $R_{AA} \sim 0.7$ and not much dependence of
 1646 p_T . Also the flow values v_n has been measured by CMS collaboration[140] up to $p_T =$
 1647 $20 \text{ GeV}/c$ for each centrality for same collision energy for Pb-Pb. They measured elliptic
 1648 flow(in terms of Fourier components of the azimuthal distribution, the $n=2$) with using
 1649 unidentified charged particles in $|\eta| < 2.4$. The anisotropic flow values are maximized
 1650 around intermediately $p_T \sim 4 \text{ GeV}/c$. To facilitate a quantitative comparison of there
 1651 result, the CMS measurements are fitted with a combination of a fifth-order polynomial

function (for $p_T < 4.2\text{GeV}/c$) and a Landau distribution (for $p_T > 4.2\text{GeV}/c$). The Results are shown in Fig.C.2, there is almost a factor of 2 or more suppression out-of-plane(where $\Delta\phi = \pi/2$) than in-plane($\Delta\phi = 0$) near $p_T = 3\text{GeV}/c$ in Centrality 20% to 30%. This suppression goes down when p_T moves higher. For RHIC experiment, the R_{AA} values as function of $\Delta\phi$ of neutral pion with respect to centrality in Au+Au collisions at $\sqrt{S_{NN}} = 200\text{GeV}$ has been Published by PHENIX collaboration. [141]

1658 C.3.2 Convert $\Delta\phi$ to path-length

1659 By using TGlauber simulation[142], for each Pb+Pb with collision energy 2.76TeV
1660 and Au+Au with collision energy 200GeV, the path length estimation has been done.
1661 To get average values of length between collision point to outside of shape, divide by 6
1662 bins(0~15, 15~30, 30~45, 45~60, 60~75, 75~90 degree) and find outermost wounded
1663 nucleon for each bins. Then histograms are filled with length from collision point to
1664 outermost nucleon and its transverse angle. The averaged values as path length for given
1665 angles are shown in Fig.C.3

1666 Based on Glauber simulations, there is no apparent path-length change in central
1667 collision. In peripheral regions, the path length has been changed more then 10% and,
1668 Path-length of out-of-plane is even longer then path-length of in-plane in more central
1669 collisions. For example, the path-length of out-of-plane in 30%~40% is approximately
1670 equal to the path-length of in-plane in 20%~30% centrality classes. The ALICE simula-
1671 tion result has always slightly longer path-length then PHENIX because of size of heavy
1672 ion species

1673 C.3.3 Path-length dependence of R_{AA}

1674 As a result, the R_{AA} values as function of $\Delta\phi$ are converted to as function of path
1675 length for each centralities. For given centrality, variation of $\Delta\phi$ gives a variation of the
1676 path length transversed for fixed initial conditions. Fig.C.4 shows the nuclear modifi-
1677 cation factor R_{AA} as a function of path-length for each p_T bins for LHC experiment.
1678 The results indicate that the suppression depends on the path-length for high p_T region
1679 particles. For the $p_T > 5\text{GeV}/cbins$, the slopes in the individual centralities are aligned

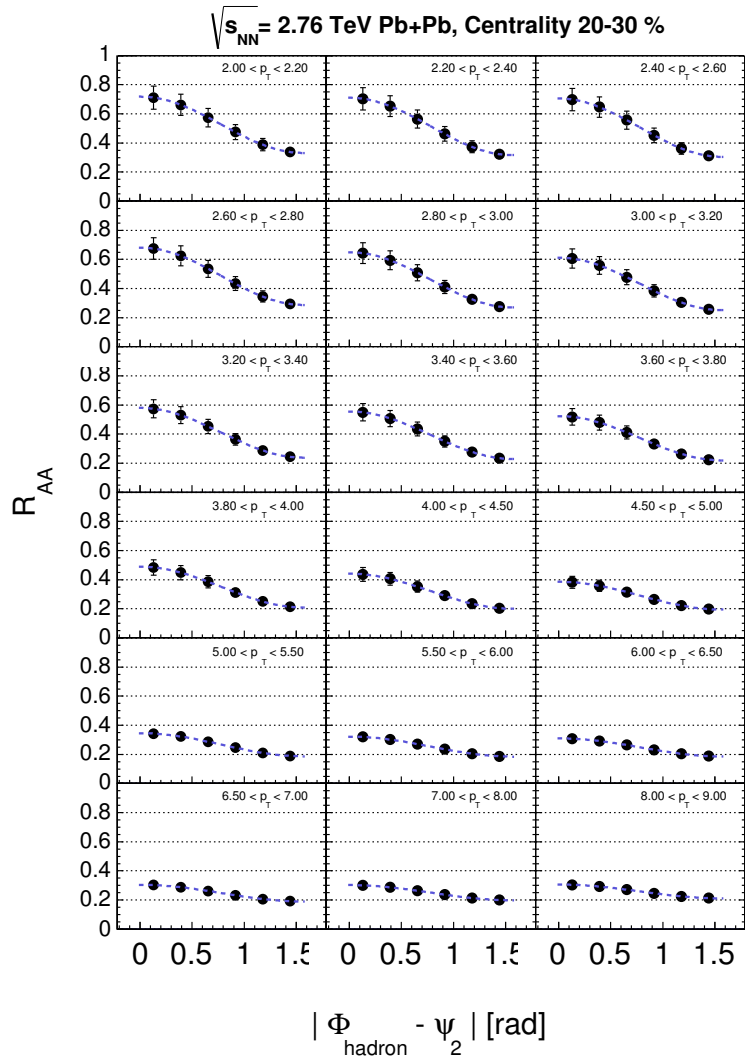


Figure C.2: R_{AA} versus $\Delta\phi$ for LHC experiment for given p_T bins. Statistical errors and systematical errors are evaluated quadratic.

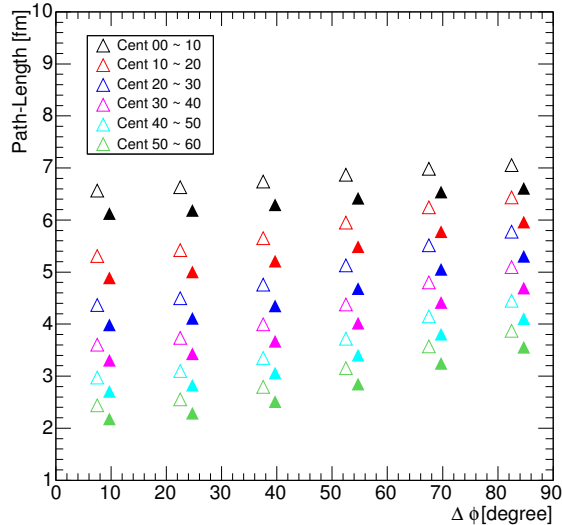


Figure C.3: Geometrical simulation result of path length calculation vs angle with respect to reaction plane by using TGlauber simulation for ALICE(open symbols) and PHENIX(closed symbols), plotted for the six centralities as shown in legend. The angle respect to reaction plane, $\Delta\phi$ is for the center of the bins(7.5, 22.5, 37.5, 52.5, 67.5 and 82.5) and centrality dependent offset is introduced for visual clarity

1680 together. And R_{AA} seems universal function with path length L for all centrality classed
 1681 for $p_T > 5GeV/c$ ranges within errors. To compare with PHENIX result, the same p_T
 1682 bin has been chosen and shows in Fig.C.5. Both result are fitted by following function

$$\frac{a}{a + L^n} \quad (C.8)$$

1683 where, a is arbitrary constant and L is path length. With this function we expect $R_{AA} = 1$
 1684 at path-length L = 0, and $R_{AA} = 0$ at path length $L = \infty$. For all centralities with more
 1685 then $p_T > 5GeV/c$, the function works well with $n \sim 2$ for both result.

1686 C.4 Summary

1687 One of the prediction of parton energy loss calculation is the average energy loss can

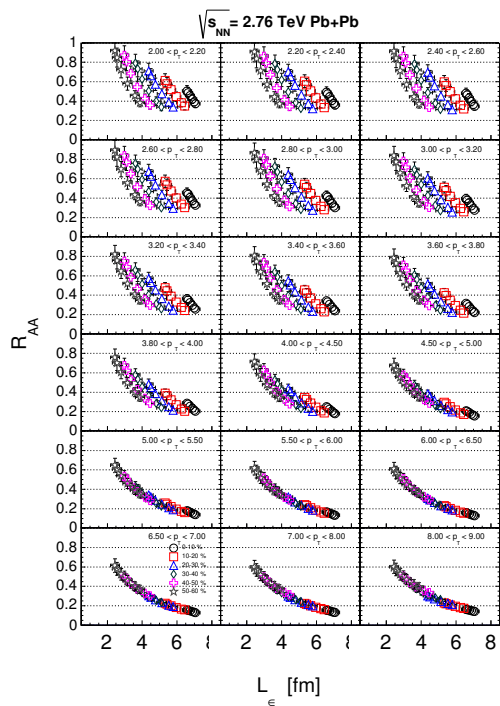


Figure C.4: R_{AA} versus Path-length correspond to $\Delta\phi$ for LHC experiment for given p_T bins. Statistical errors and systematical errors are evaluated quadratic.

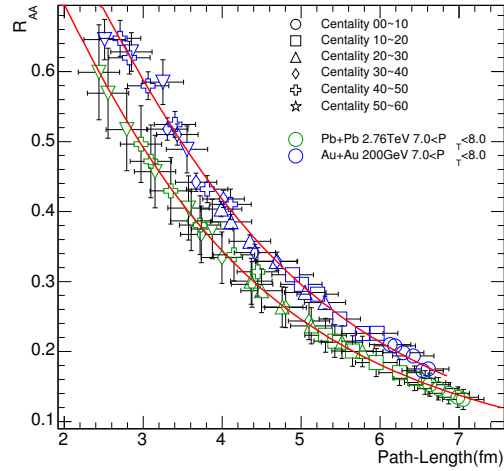


Figure C.5: Comparison of R_{AA} as function of path length for ALICE and PHENIX with $7\sim 8$ GeV/c p_T bin

1688 be represent as a function of the mean free path in medium. And energy loss in medium
 1689 can be indirectly evaluated from nuclear modification factor, R_{AA} . With combination
 1690 of using inclusive R_{AA} and flow, we can estimate the dependence of suppression on
 1691 geometry which related to mean free path length. we presented result of path-length
 1692 dependence of R_{AA} by using flow harmonics and calculation of path length from glauber
 1693 simulation. As the results, in high p_T ranges ($p_T > 5.0 \text{ GeV}/c$), the R_{AA} seems universal
 1694 function with path length. Moreover the decrease slope of R_{AA} as function of path-
 1695 length were well fitted by 2nd order inverse function.

References

- [1] “Closing in on the border between primordial plasma and ordinary matter.”
- [2] R. Snellings, “Elliptic Flow: A Brief Review,” *New J. Phys.*, vol. 13, p. 055008, 2011.
- [3] P. F. Kolb and U. W. Heinz, “Hydrodynamic description of ultrarelativistic heavy ion collisions,” 2003.
- [4] S. A. Voloshin, A. M. Poskanzer, and R. Snellings, “Collective phenomena in non-central nuclear collisions,” 2008.
- [5] M. L. Miller, K. Reygers, S. J. Sanders, and P. Steinberg, “Glauber modeling in high energy nuclear collisions,” *Ann. Rev. Nucl. Part. Sci.*, vol. 57, pp. 205–243, 2007.
- [6] A. Bzdak, “Heavy ion collisions in the used nucleon model,” *Phys. Lett.*, vol. B647, pp. 358–360, 2007.
- [7] K. Aamodt *et al.*, “Elliptic flow of charged particles in Pb-Pb collisions at 2.76 TeV,” *Phys. Rev. Lett.*, vol. 105, p. 252302, 2010.
- [8] G. Roland, K. Šafařík, and P. Steinberg, “Heavy-ion collisions at the {LHC},” *Progress in Particle and Nuclear Physics*, vol. 77, pp. 70 – 127, 2014.
- [9] G. Aad *et al.*, “Measurement of event-plane correlations in $\sqrt{s_{NN}} = 2.76$ TeV lead-lead collisions with the ATLAS detector,” *Phys. Rev.*, vol. C90, no. 2, p. 024905, 2014.

- 1716 [10] S. Chatrchyan *et al.*, “Measurement of higher-order harmonic azimuthal
1717 anisotropy in PbPb collisions at $\sqrt{s_{NN}} = 2.76$ TeV,” *Phys. Rev.*, vol. C89, no. 4,
1718 p. 044906, 2014.
- 1719 [11] “Cern document server.”
- 1720 [12] “Aliroot documentation.”
- 1721 [13] H. Niemi, K. J. Eskola, and R. Paatelainen, “Event-by-event fluctuations in a
1722 perturbative QCD + saturation + hydrodynamics model: Determining QCD mat-
1723 ter shear viscosity in ultrarelativistic heavy-ion collisions,” *Phys. Rev.*, vol. C93,
1724 no. 2, p. 024907, 2016.
- 1725 [14] G. Giacalone, L. Yan, J. Noronha-Hostler, and J.-Y. Ollitrault, “Symmetric cu-
1726 mulants and event-plane correlations in Pb + Pb collisions,” *Phys. Rev.*, vol. C94,
1727 no. 1, p. 014906, 2016.
- 1728 [15] H. D. Politzer, “Reliable perturbative results for strong interactions?,” *Phys. Rev.*
1729 *Lett.*, vol. 30, pp. 1346–1349, Jun 1973.
- 1730 [16] D. J. Gross and F. Wilczek, “Ultraviolet behavior of non-abelian gauge theories,”
1731 *Phys. Rev. Lett.*, vol. 30, pp. 1343–1346, Jun 1973.
- 1732 [17] K. G. Wilson, “Confinement of quarks,” *Phys. Rev. D*, vol. 10, pp. 2445–2459,
1733 Oct 1974.
- 1734 [18] J. Adams *et al.*, “Experimental and theoretical challenges in the search for the
1735 quark gluon plasma: The STAR Collaboration’s critical assessment of the evi-
1736 dence from RHIC collisions,” *Nucl. Phys.*, vol. A757, pp. 102–183, 2005.
- 1737 [19] J. C. Collins and M. J. Perry, “Superdense matter: Neutrons or asymptotically
1738 free quarks?,” *Phys. Rev. Lett.*, vol. 34, pp. 1353–1356, May 1975.
- 1739 [20] N. Cabibbo and G. Parisi, “Exponential hadronic spectrum and quark liberation,”
1740 *Physics Letters B*, vol. 59, no. 1, pp. 67 – 69, 1975.
- 1741 [21] F. Karsch *PoSCPOD*, vol. 07, no. 026, (2007).

- 1742 [22] E. Lofgren, “Accelerator division annual reports, 1 july 1972 12/31/1974,”
1743 *Lawrence Berkeley National Laboratory*, 2008.
- 1744 [23] A. Kovalenko, A. Baldin, A. Malakhov, *et al.*, “Status of the nuclotron,” in *Pro-*
1745 *ceedings of EPAC*, vol. 94, pp. 161–164, 1994.
- 1746 [24] M. Gyulassy and L. McLerran, “New forms of qcd matter discovered at rhic,”
1747 *Nuclear Physics A*, vol. 750, no. 1, pp. 30–63, 2005.
- 1748 [25] D. Barton *et al.*, *Heavy ion program at BNL: AGS, RHIC*. Brookhaven National
1749 Lab., 1987.
- 1750 [26] K. Grebieszkow, “Hot strong matter,” *arXiv preprint arXiv:1407.3690*, 2014.
- 1751 [27] I. Arsene, I. Bearden, D. Beavis, C. Besliu, B. Budick, H. Bøggild, C. Chasman,
1752 C. Christensen, P. Christiansen, J. Cibor, *et al.*, “Quark–gluon plasma and color
1753 glass condensate at rhic? the perspective from the brahms experiment,” *Nuclear*
1754 *Physics A*, vol. 757, no. 1, pp. 1–27, 2005.
- 1755 [28] B. B. Back *et al.*, “The PHOBOS perspective on discoveries at RHIC,” *Nucl.*
1756 *Phys.*, vol. A757, pp. 28–101, 2005.
- 1757 [29] J. D. Bjorken, “Highly relativistic nucleus-nucleus collisions: The central rapidity
1758 region,” *Phys. Rev. D*, vol. 27, pp. 140–151, Jan 1983.
- 1759 [30] R. Rapp, B. Kämpfer, A. Andronic, D. Blaschke, C. Fuchs, M. Harada, T. Hilger,
1760 M. Kitazawa, T. Kunihiro, P. Petreczky, F. Riek, C. Sasaki, R. Thomas, L. To-
1761 los, P. Zhuang, H. van Hees, R. Vogt, and S. Zschocke, *In-Medium Excitations*,
1762 pp. 335–529. Berlin, Heidelberg: Springer Berlin Heidelberg, 2011.
- 1763 [31] C. Shen, U. Heinz, P. Huovinen, and H. Song, “Radial and elliptic flow in Pb+Pb
1764 collisions at the Large Hadron Collider from viscous hydrodynamic,” *Phys. Rev.*,
1765 vol. C84, p. 044903, 2011.
- 1766 [32] A. Bazavov *et al.*, “Equation of state in (2+1)-flavor QCD,” *Phys. Rev.*, vol. D90,
1767 p. 094503, 2014.

- 1768 [33] S. Voloshin and Y. Zhang, “Flow study in relativistic nuclear collisions by fourier
 1769 expansion of azimuthal particle distributions,” *Zeitschrift für Physik C Particles*
 1770 and *Fields*, vol. 70, no. 4, pp. 665–671, 1996.
- 1771 [34] K. H. Ackermann *et al.*, “Elliptic flow in Au + Au collisions at $(S_{NN})^{**}(1/2) =$
 1772 130 GeV,” *Phys. Rev. Lett.*, vol. 86, pp. 402–407, 2001.
- 1773 [35] J. Adam *et al.*, “Anisotropic flow of charged particles in Pb-Pb collisions at
 1774 $\sqrt{s_{NN}} = 5.02 \text{ TeV}$,” *Phys. Rev. Lett.*, vol. 116, no. 13, p. 132302, 2016.
- 1775 [36] P. Romatschke and U. Romatschke, “Viscosity Information from Relativistic Nu-
 1776 clear Collisions: How Perfect is the Fluid Observed at RHIC?,” *Phys. Rev. Lett.*,
 1777 vol. 99, p. 172301, 2007.
- 1778 [37] B. Schenke, S. Jeon, and C. Gale, “Elliptic and triangular flows in 3 + 1D viscous
 1779 hydrodynamics with fluctuating initial conditions,” *J. Phys.*, vol. G38, p. 124169,
 1780 2011.
- 1781 [38] P. Bozek and I. Wyskiel-Piekarska, “Particle spectra in Pb-Pb collisions at
 1782 $\sqrt{S_{NN}} = 2.76 \text{ TeV}$,” *Phys. Rev.*, vol. C85, p. 064915, 2012.
- 1783 [39] C. Gale, S. Jeon, B. Schenke, P. Tribedy, and R. Venugopalan, “Event-by-event
 1784 anisotropic flow in heavy-ion collisions from combined Yang-Mills and viscous
 1785 fluid dynamics,” *Phys. Rev. Lett.*, vol. 110, no. 1, p. 012302, 2013.
- 1786 [40] T. Hirano, P. Huovinen, and Y. Nara, “Elliptic flow in Pb+Pb collisions at
 1787 $\sqrt{s_{NN}} = 2.76 \text{ TeV}$: hybrid model assessment of the first data,” *Phys. Rev.*,
 1788 vol. C84, p. 011901, 2011.
- 1789 [41] P. Kovtun, D. T. Son, and A. O. Starinets, “Viscosity in strongly interacting quan-
 1790 tum field theories from black hole physics,” *Phys. Rev. Lett.*, vol. 94, p. 111601,
 1791 2005.
- 1792 [42] R. A. Lacey, N. N. Ajitanand, J. M. Alexander, P. Chung, W. G. Holzmann, M. Is-
 1793 sah, A. Taranenko, P. Danielewicz, and H. Stoecker, “Has the QCD Critical Point

- 1794 been Signaled by Observations at RHIC?,” *Phys. Rev. Lett.*, vol. 98, p. 092301,
1795 2007.
- 1796 [43] P. Danielewicz and M. Gyulassy, “Dissipative phenomena in quark-gluon plas-
1797 mas,” *Phys. Rev. D*, vol. 31, pp. 53–62, Jan 1985.
- 1798 [44] A. M. Poskanzer and S. A. Voloshin, “Methods for analyzing anisotropic flow in
1799 relativistic nuclear collisions,” *Phys. Rev. C*, vol. 58, pp. 1671–1678, Sep 1998.
- 1800 [45] M. Luzum and H. Petersen, “Initial State Fluctuations and Final State Correlations
1801 in Relativistic Heavy-Ion Collisions,” *J. Phys.*, vol. G41, p. 063102, 2014.
- 1802 [46] B. Alver *et al.*, “Importance of correlations and fluctuations on the initial source
1803 eccentricity in high-energy nucleus-nucleus collisions,” *Phys. Rev.*, vol. C77,
1804 p. 014906, 2008.
- 1805 [47] S. Wang, Y. Z. Jiang, Y. M. Liu, D. Keane, D. Beavis, S. Y. Chu, S. Y. Fung,
1806 M. Vient, C. Hartnack, and H. Stoecker, “Measurement of collective flow in heavy
1807 ion collisions using particle pair correlations,” *Phys. Rev.*, vol. C44, pp. 1091–
1808 1095, 1991.
- 1809 [48] M. B. Tsang, R. T. de Souza, Y.-d. Kim, D. R. Bowman, N. Carlin, C. K. Gelbke,
1810 W. G. Gong, W. G. Lynch, L. Phair, and F. Zhu, “Reaction plane determination for
1811 Ar-36 + Au-197 collisions at E/A=35 MeV,” *Phys. Rev.*, vol. C44, pp. 2065–2081,
1812 1991.
- 1813 [49] D. d’Enterria, “Jet quenching,” *Landolt-Bornstein*, vol. 23, p. 471, 2010.
- 1814 [50] X.-N. Wang and M. Gyulassy, “Gluon shadowing and jet quenching in $A + A$
1815 collisions at $\sqrt{s} = 200 \text{ GeV}$,” *Phys. Rev. Lett.*, vol. 68, pp. 1480–1483, Mar 1992.
- 1816 [51] M. Aggarwal *et al.*, “Transverse mass distributions of neutral pions from pb-
1817 induced reactions at 158 gev,” *The European Physical Journal C - Particles and
1818 Fields*, vol. 23, no. 2, pp. 225–236, 2002.

- 1819 [52] A. e. a. Adare, “Suppression pattern of neutral pions at high transverse momentum
 1820 in Au + Au collisions at $\sqrt{s_{NN}} = 200$ GeV and constraints on medium transport
 1821 coefficients,” *Phys. Rev. Lett.*, vol. 101, p. 232301, Dec 2008.
- 1822 [53] J. a. e. Adams, “Transverse-momentum and collision-energy dependence of high-
 1823 p_T hadron suppression in Au + Au collisions at ultrarelativistic energies,” *Phys.*
 1824 *Rev. Lett.*, vol. 91, p. 172302, Oct 2003.
- 1825 [54] P. Christiansen, “Event-Shape Engineering and Jet Quenching,” *J. Phys. Conf.*
 1826 *Ser.*, vol. 736, no. 1, p. 012023, 2016.
- 1827 [55] M. Miller and R. Snellings, “Eccentricity fluctuations and its possible effect on
 1828 elliptic flow measurements,” 2003.
- 1829 [56] B. Alver *et al.*, “System size, energy, pseudorapidity, and centrality dependence
 1830 of elliptic flow,” *Phys. Rev. Lett.*, vol. 98, p. 242302, 2007.
- 1831 [57] B. Alver and G. Roland, “Collision geometry fluctuations and triangular flow in
 1832 heavy-ion collisions,” *Phys. Rev.*, vol. C81, p. 054905, 2010. [Erratum: *Phys.*
 1833 *Rev.*C82,039903(2010)].
- 1834 [58] K. Aamodt *et al.*, “Higher harmonic anisotropic flow measurements of charged
 1835 particles in Pb-Pb collisions at $\sqrt{s_{NN}}=2.76$ TeV,” *Phys. Rev. Lett.*, vol. 107,
 1836 p. 032301, 2011.
- 1837 [59] M. Luzum and J.-Y. Ollitrault, “Extracting the shear viscosity of the quark-gluon
 1838 plasma from flow in ultra-central heavy-ion collisions,” *Nucl. Phys.*, vol. A904-
 1839 905, pp. 377c–380c, 2013.
- 1840 [60] T. Renk and H. Niemi, “Constraints from v_2 fluctuations for the initial-state ge-
 1841 ometry of heavy-ion collisions,” *Phys. Rev.*, vol. C89, no. 6, p. 064907, 2014.
- 1842 [61] L. Yan, J.-Y. Ollitrault, and A. M. Poskanzer, “Azimuthal Anisotropy Distribu-
 1843 tions in High-Energy Collisions,” *Phys. Lett.*, vol. B742, pp. 290–295, 2015.

- 1844 [62] C. Shen, S. A. Bass, T. Hirano, P. Huovinen, Z. Qiu, H. Song, and U. Heinz, “The
1845 QGP shear viscosity: Elusive goal or just around the corner?,” *J. Phys.*, vol. G38,
1846 p. 124045, 2011.
- 1847 [63] P. Bozek, “Flow and interferometry in 3+1 dimensional viscous hydrodynamics,”
1848 *Phys. Rev.*, vol. C85, p. 034901, 2012.
- 1849 [64] J.-B. Rose, J.-F. Paquet, G. S. Denicol, M. Luzum, B. Schenke, S. Jeon, and
1850 C. Gale, “Extracting the bulk viscosity of the quark?gluon plasma,” *Nucl. Phys.*,
1851 vol. A931, pp. 926–930, 2014.
- 1852 [65] S. Ryu, J. F. Paquet, C. Shen, G. S. Denicol, B. Schenke, S. Jeon, and C. Gale,
1853 “Importance of the Bulk Viscosity of QCD in Ultrarelativistic Heavy-Ion Colli-
1854 sions,” *Phys. Rev. Lett.*, vol. 115, no. 13, p. 132301, 2015.
- 1855 [66] D. Teaney and L. Yan, “Non linearities in the harmonic spectrum of heavy ion col-
1856 lisions with ideal and viscous hydrodynamics,” *Phys. Rev.*, vol. C86, p. 044908,
1857 2012.
- 1858 [67] L. V. Bravina, B. H. Brusheim Johansson, G. K. Eyyubova, V. L. Korotkikh, I. P.
1859 Loktin, L. V. Malinina, S. V. Petrushanko, A. M. Snigirev, and E. E. Zabrodin,
1860 “Hexagonal flow v6 as a superposition of elliptic v2 and triangular v3 flows,”
1861 *Phys. Rev.*, vol. C89, no. 2, p. 024909, 2014.
- 1862 [68] M. Luzum and J.-Y. Ollitrault, “Constraining the viscous freeze-out distribution
1863 function with data obtained at the BNL Relativistic Heavy Ion Collider (RHIC),”
1864 *Phys. Rev.*, vol. C82, p. 014906, 2010.
- 1865 [69] H. Niemi, G. S. Denicol, H. Holopainen, and P. Huovinen, “Event-by-event distri-
1866 butions of azimuthal asymmetries in ultrarelativistic heavy-ion collisions,” *Phys.*
1867 *Rev. C*, vol. 87, p. 054901, May 2013.
- 1868 [70] A. Bilandzic, C. H. Christensen, K. Gulbrandsen, A. Hansen, and Y. Zhou,
1869 “Generic framework for anisotropic flow analyses with multiparticle azimuthal
1870 correlations,” *Phys. Rev. C*, vol. 89, p. 064904, Jun 2014.

- 1871 [71] J. Adam *et al.*, “Correlated event-by-event fluctuations of flow harmonics in Pb-
1872 Pb collisions at $\sqrt{s_{\text{NN}}} = 2.76$ TeV,” *Phys. Rev. Lett.*, vol. 117, p. 182301, 2016.
- 1873 [72] *The CERN Large Hadron Collider: Accelerator and Experiments, LHC Machine*.
1874 JINST, 2008.
- 1875 [73] “Alice public web page.”
- 1876 [74] “Atlas public web pages.”
- 1877 [75] “Cms public web page.”
- 1878 [76] P. Cortese, C. W. Fabjan, L. Riccati, K. Safarík, and H. de Groot, *ALICE
1879 physics performance: Technical Design Report*. Technical Design Report AL-
1880 ICE, Geneva: CERN, 2005. revised version submitted on 2006-05-29 15:15:40.
- 1881 [77] F. Meddi, “The {ALICE} silicon pixel detector (spd),” *Nuclear Instruments and
1882 Methods in Physics Research Section A: Accelerators, Spectrometers, Detectors
1883 and Associated Equipment*, vol. 465, no. 1, pp. 40 – 45, 2001. {SPD2000}.
- 1884 [78] B. Alessandro *et al.*, “Charge collection in the Silicon Drift Detectors of the AL-
1885 ICE experiment,” *JINST*, vol. 5, p. P02008, 2010.
- 1886 [79] G. Contin, “The ALICE Silicon Strip Detector performance during the first LHC
1887 data taking,” *Conf. Proc.*, vol. C100901, pp. 257–260, 2010.
- 1888 [80] G. Contin, *The Silicon Strip Detector (SSD) for the ALICE experiment at LHC:
1889 construction, characterization and charged particles multiplicity studies*. PhD
1890 thesis, Trieste U., 2009.
- 1891 [81] “Upgrade of the ALICE Time Projection Chamber,” Tech. Rep. CERN-LHCC-
1892 2013-020. ALICE-TDR-016, Oct 2013.
- 1893 [82] A. Collaboration, “Performance of the alice vzero system,” *arXiv preprint
1894 arXiv:1306.3130*, 2013.

- 1895 [83] P. Cortese, *ALICE transition-radiation detector: Technical Design Report*. Tech-
1896 nical Design Report ALICE, Geneva: CERN, 2001.
- 1897 [84] A. Alici, A. Collaboration, *et al.*, “The mrpc-based alice time-of-flight detector:
1898 status and performance,” *Nuclear Instruments and Methods in Physics Research
1899 Section A: Accelerators, Spectrometers, Detectors and Associated Equipment*,
1900 vol. 706, pp. 29–32, 2013.
- 1901 [85] L. Molnar, “The ALICE HMPID detector ready for collisions at the LHC,” *Nucl.
1902 Instrum. Meth.*, vol. A595, pp. 27–30, 2008.
- 1903 [86] H. Torii and the ALICE-PHOS Collaborations, “The alice phos calorimeter,”
1904 *Journal of Physics: Conference Series*, vol. 160, no. 1, p. 012045, 2009.
- 1905 [87] R. B. for the ALICE EMCal Collaboration *et al.*, “Alice emcal physics perfor-
1906 mance report,” *arXiv preprint arXiv:1008.0413*, 2010.
- 1907 [88] P. Cortese, V. Chambert, R. Simon, J. Contreras, P. Van de Vyvre, A. Di Bar-
1908 tolomeo, V. Petrov, A. De Haas, F. Navach, A. Kolojvari, *et al.*, “Alice forward
1909 detectors: Fmd, to and vo,” tech. rep., ALICE-TDR-011, 2004.
- 1910 [89] C. Oppedisano, R. Arnaldi, E. Chiavassa, C. Cicalò, P. Cortese, A. De Falco,
1911 G. Dellacasa, N. De Marco, A. Ferretti, M. Floris, *et al.*, “Physics performance of
1912 the alice zero degree calorimeter,” *Nuclear Physics B-Proceedings Supplements*,
1913 vol. 197, no. 1, pp. 206–210, 2009.
- 1914 [90] D. Adamová, J. Chudoba, T. Kouba, P. M. Lorenzo, P. Saiz, J. Švec, and J. Hampl,
1915 “Status of the grid computing for the alice experiment in the czech republic,”
1916 *Journal of Physics: Conference Series*, vol. 219, no. 7, p. 072023, 2010.
- 1917 [91] K. Aamodt *et al.*, “The ALICE experiment at the CERN LHC,” *JINST*, vol. 3,
1918 p. S08002, 2008.
- 1919 [92] P. Cortese *et al.*, “ALICE: Physics performance report, volume I,” *J. Phys.*,
1920 vol. G30, pp. 1517–1763, 2004.

- 1921 [93] P. Cortese *et al.*, “ALICE: Physics performance report, volume II,” *J. Phys.*,
 1922 vol. G32, pp. 1295–2040, 2006.
- 1923 [94] K. Aamodt *et al.*, “Centrality dependence of the charged-particle multiplicity den-
 1924 sity at mid-rapidity in Pb-Pb collisions at $\sqrt{s_{NN}} = 2.76$ TeV,” *Phys. Rev. Lett.*,
 1925 vol. 106, p. 032301, 2011.
- 1926 [95] X.-N. Wang and M. Gyulassy, “HIJING: A Monte Carlo model for multiple jet
 1927 production in p p, p A and A A collisions,” *Phys. Rev.*, vol. D44, pp. 3501–3516,
 1928 1991.
- 1929 [96] “GEANT Detector Description and Simulation Tool,” 1994.
- 1930 [97] H. Niemi, G. S. Denicol, H. Holopainen, and P. Huovinen, “Event-by-event distri-
 1931 butions of azimuthal asymmetries in ultrarelativistic heavy-ion collisions,” *Phys.*
 1932 *Rev.*, vol. C87, no. 5, p. 054901, 2013.
- 1933 [98] A. Bilandzic, C. H. Christensen, K. Gulbrandsen, A. Hansen, and Y. Zhou,
 1934 “Generic framework for anisotropic flow analyses with multiparticle azimuthal
 1935 correlations,” *Phys. Rev.*, vol. C89, no. 6, p. 064904, 2014.
- 1936 [99] A. Adare *et al.*, “Measurements of Higher-Order Flow Harmonics in Au+Au Col-
 1937 lisions at $\sqrt{s_{NN}} = 200$ GeV,” *Phys. Rev. Lett.*, vol. 107, p. 252301, 2011.
- 1938 [100] G. Aad *et al.*, “Measurement with the ATLAS detector of multi-particle azimuthal
 1939 correlations in p+Pb collisions at $\sqrt{s_{NN}} = 5.02$ TeV,” *Phys. Lett.*, vol. B725,
 1940 pp. 60–78, 2013.
- 1941 [101] B. B. Abelev *et al.*, “Multiparticle azimuthal correlations in p -Pb and Pb-Pb colli-
 1942 sions at the CERN Large Hadron Collider,” *Phys. Rev.*, vol. C90, no. 5, p. 054901,
 1943 2014.
- 1944 [102] V. Khachatryan *et al.*, “Evidence for Collective Multiparticle Correlations in p-Pb
 1945 Collisions,” *Phys. Rev. Lett.*, vol. 115, no. 1, p. 012301, 2015.

- 1946 [103] L. Adamczyk *et al.*, “Long-range pseudorapidity dihadron correlations in d +Au
1947 collisions at $\sqrt{s_{NN}} = 200$ GeV,” *Phys. Lett.*, vol. B747, pp. 265–271, 2015.
- 1948 [104] A. Adare *et al.*, “Measurements of elliptic and triangular flow in high-multiplicity
1949 $^3\text{He}+\text{Au}$ collisions at $\sqrt{s_{NN}} = 200$ GeV,” *Phys. Rev. Lett.*, vol. 115, no. 14,
1950 p. 142301, 2015.
- 1951 [105] C. Loizides, “Experimental overview on small collision systems at the LHC,”
1952 in *Proceedings, 25th International Conference on Ultra-Relativistic Nucleus-Nucleus Collisions (Quark Matter 2015): Kobe, Japan, September 27-October 3, 2015*, 2016.
- 1955 [106] R. S. . Bhalerao, J.-Y. Ollitrault, and S. Pal, “Characterizing flow fluctuations with
1956 moments,” *Physics Letters B*, vol. 742, pp. 94–98, Mar. 2015.
- 1957 [107] M. Gyulassy and X.-N. Wang, “HIJING 1.0: A Monte Carlo program for parton
1958 and particle production in high-energy hadronic and nuclear collisions,” *Comput. Phys. Commun.*, vol. 83, p. 307, 1994.
- 1960 [108] X.-N. Wang and M. Gyulassy, “hijing: A monte carlo model for multiple jet pro-
1961 duction in pp, pA, and AA collisions,” *Phys. Rev. D*, vol. 44, pp. 3501–3516, Dec
1962 1991.
- 1963 [109] N. Borghini, P. M. Dinh, and J.-Y. Ollitrault, “A New method for measur-
1964 ing azimuthal distributions in nucleus-nucleus collisions,” *Phys. Rev.*, vol. C63,
1965 p. 054906, 2001.
- 1966 [110] R. Paatelainen, K. J. Eskola, H. Holopainen, and K. Tuominen, “Multiplicities and
1967 p_T spectra in ultrarelativistic heavy ion collisions from a next-to-leading order
1968 improved perturbative QCD + saturation + hydrodynamics model,” *Phys. Rev.*,
1969 vol. C87, no. 4, p. 044904, 2013.
- 1970 [111] R. Paatelainen, K. J. Eskola, H. Niemi, and K. Tuominen, “Fluid dynamics with
1971 saturated minijet initial conditions in ultrarelativistic heavy-ion collisions,” *Phys.
1972 Lett.*, vol. B731, pp. 126–130, 2014.

- 1973 [112] K. J. Eskola, H. Niemi, and R. Paatelainen, “Pinning down QCD-matter shear vis-
1974 cosity in ultrarelativistic heavy-ion collisions via EbyE fluctuations using pQCD
1975 + saturation + hydrodynamics,” in *Proceedings, 7th International Conference*
1976 *on Hard and Electromagnetic Probes of High-Energy Nuclear Collisions (Hard*
1977 *Probes 2015): Montréal, Québec, Canada, June 29-July 3, 2015*, 2016.
- 1978 [113] B. Zhang, C. M. Ko, B.-A. Li, and Z.-w. Lin, “A multiphase transport model for
1979 nuclear collisions at RHIC,” *Phys. Rev.*, vol. C61, p. 067901, 2000.
- 1980 [114] Z.-w. Lin, S. Pal, C. M. Ko, B.-A. Li, and B. Zhang, “Charged particle rapidity
1981 distributions at relativistic energies,” *Phys. Rev.*, vol. C64, p. 011902, 2001.
- 1982 [115] Z.-W. Lin, C. M. Ko, B.-A. Li, B. Zhang, and S. Pal, “A Multi-phase transport
1983 model for relativistic heavy ion collisions,” *Phys. Rev.*, vol. C72, p. 064901, 2005.
- 1984 [116] B. Andersson, G. Gustafson, and B. Nilsson-Almqvist, “A Model for Low p(t)
1985 Hadronic Reactions, with Generalizations to Hadron - Nucleus and Nucleus-
1986 Nucleus Collisions,” *Nucl. Phys.*, vol. B281, pp. 289–309, 1987.
- 1987 [117] B. Nilsson-Almqvist and E. Stenlund, “Interactions Between Hadrons and Nuclei:
1988 The Lund Monte Carlo, Fritiof Version 1.6,” *Comput. Phys. Commun.*, vol. 43,
1989 p. 387, 1987.
- 1990 [118] B. Zhang, “ZPC 1.0.1: A Parton cascade for ultrarelativistic heavy ion collisions,”
1991 *Comput. Phys. Commun.*, vol. 109, pp. 193–206, 1998.
- 1992 [119] Z.-W. Lin, C. M. Ko, B.-A. Li, B. Zhang, and S. Pal, “Multiphase transport model
1993 for relativistic heavy ion collisions,” *Physical Review C*, vol. 72, pp. 064901–29,
1994 Dec. 2005.
- 1995 [120] B. Li, A. T. Sustich, B. Zhang, and C. M. Ko, “Studies of superdense hadronic
1996 matter in a relativistic transport model,” *Int. J. Mod. Phys.*, vol. E10, pp. 267–352,
1997 2001.
- 1998 [121] Z.-w. Lin and C. M. Ko, “Partonic effects on the elliptic flow at RHIC,” *Phys.*
1999 *Rev.*, vol. C65, p. 034904, 2002.

- 2000 [122] Z.-W. Lin, “Evolution of transverse flow and effective temperatures in the parton
 2001 phase from a multi-phase transport model,” *Phys. Rev.*, vol. C90, no. 1, p. 014904,
 2002 2014.
- 2003 [123] J. Adam *et al.*, “Higher harmonic flow coefficients of identified hadrons in Pb-Pb
 2004 collisions at $\sqrt{s_{NN}} = 2.76$ TeV,” *JHEP*, vol. 09, p. 164, 2016.
- 2005 [124] X. Zhu, Y. Zhou, H. Xu, and H. Song, “Correlations of flow harmonics in 2.76A
 2006 TeV Pb–Pb collisions,” 2016.
- 2007 [125] H.-j. Xu, Z. Li, and H. Song, “High-order flow harmonics of identified hadrons in
 2008 2.76A TeV Pb + Pb collisions,” *Phys. Rev.*, vol. C93, no. 6, p. 064905, 2016.
- 2009 [126] R. S. Bhalerao, A. Jaiswal, and S. Pal, “Collective flow in event-by-event par-
 2010 tonic transport plus hydrodynamics hybrid approach,” *Phys. Rev.*, vol. C92, no. 1,
 2011 p. 014903, 2015.
- 2012 [127] L. Pang, Q. Wang, and X.-N. Wang, “Effects of initial flow velocity fluctuation in
 2013 event-by-event (3+1)D hydrodynamics,” *Phys. Rev.*, vol. C86, p. 024911, 2012.
- 2014 [128] Z. Qiu, C. Shen, and U. Heinz, “Hydrodynamic elliptic and triangular flow in
 2015 Pb-Pb collisions at $\sqrt{s} = 2.76\text{ATeV}$,” *Phys. Lett.*, vol. B707, pp. 151–155, 2012.
- 2016 [129] C. Shen, U. Heinz, P. Huovinen, and H. Song, “Systematic parameter study
 2017 of hadron spectra and elliptic flow from viscous hydrodynamic simulations of
 2018 Au+Au collisions at $\sqrt{s_{NN}} = 200$ GeV,” *Phys. Rev.*, vol. C82, p. 054904, 2010.
- 2019 [130] P. F. Kolb, J. Sollfrank, and U. W. Heinz, “Anisotropic transverse flow and the
 2020 quark hadron phase transition,” *Phys. Rev.*, vol. C62, p. 054909, 2000.
- 2021 [131] D. Kharzeev and M. Nardi, “Hadron production in nuclear collisions at RHIC and
 2022 high density QCD,” *Phys. Lett.*, vol. B507, pp. 121–128, 2001.
- 2023 [132] H. J. Drescher and Y. Nara, “Effects of fluctuations on the initial eccentricity
 2024 from the Color Glass Condensate in heavy ion collisions,” *Phys. Rev.*, vol. C75,
 2025 p. 034905, 2007.

- 2026 [133] T. Hirano and Y. Nara, “Eccentricity fluctuation effects on elliptic flow in rela-
2027 tivistic heavy ion collisions,” *Phys. Rev.*, vol. C79, p. 064904, 2009.
- 2028 [134] F. G. Gardim, F. Grassi, M. Luzum, and J.-Y. Ollitrault, “Mapping the hydro-
2029 dynamic response to the initial geometry in heavy-ion collisions,” *Phys. Rev. C*,
2030 vol. 85, p. 024908, Feb 2012.
- 2031 [135] L. Yan and J.-Y. Ollitrault, “ v_4, v_5, v_6, v_7 : nonlinear hydrodynamic response
2032 versus LHC data,” *arXiv.org*, pp. 82–87, Feb. 2015.
- 2033 [136] K. Adcox *et al.*, “Suppression of hadrons with large transverse momentum in cen-
2034 tral Au+Au collisions at $\sqrt{s_{NN}} = 130\text{-GeV}$,” *Phys. Rev. Lett.*, vol. 88, p. 022301,
2035 2002.
- 2036 [137] J. Liao and V. Koch, “Exposing the non-collectivity in elliptic flow,” *Phys. Rev.*
2037 *Lett.*, vol. 103, p. 042302, 2009.
- 2038 [138] S. Adler *et al.*, “A Detailed Study of High-p(T) Neutral Pion Suppression and Az-
2039 imuthal Anisotropy in Au+Au Collisions at $s(\text{NN})^{**}(1/2) = 200\text{-GeV}$,” *Phys.Rev.*,
2040 vol. C76, p. 034904, 2007.
- 2041 [139] B. Abelev *et al.*, “Centrality Dependence of Charged Particle Production at Large
2042 Transverse Momentum in Pb–Pb Collisions at $\sqrt{s_{NN}} = 2.76\text{ TeV}$,” *Phys.Lett.*,
2043 vol. B720, pp. 52–62, 2013.
- 2044 [140] S. Chatrchyan *et al.*, “Measurement of the elliptic anisotropy of charged parti-
2045 cles produced in PbPb collisions at nucleon-nucleon center-of-mass energy = 2.76
2046 TeV,” *Phys.Rev.*, vol. C87, p. 014902, 2013.
- 2047 [141] A. Adare *et al.*, “Neutral pion production with respect to centrality and reac-
2048 tion plane in Au+Au collisions at $\sqrt{s_{NN}}=200\text{ GeV}$,” *Phys.Rev.*, vol. C87, no. 3,
2049 p. 034911, 2013.
- 2050 [142] B. Alver, M. Baker, C. Loizides, and P. Steinberg, “The PHOBOS Glauber Monte
2051 Carlo,” 2008.